

ENGINEERING A RAPID POINT-OF-CARE DIAGNOSTIC PLATFORM UTILIZING TETHERED ENZYME
TECHNOLOGY FOR TIME-SENSITIVE PATHOLOGIES

A Dissertation

Presented to the Faculty of the Graduate School

of Cornell University

in Partial Fulfillment of the Requirements for the Degree of

Doctor of Philosophy

by

James Paul Lata

August 2015

© 2015 James Paul Lata

ENGINEERING A RAPID POINT-OF-CARE DIAGNOSTIC PLATFORM UTILIZING TETHERED ENZYME TECHNOLOGY FOR TIME-SENSITIVE PATHOLOGIES

James Paul Lata, Ph.D.

Cornell University 2015

The primary advances in creating a point-of-care testing (PoCT) diagnostic platform involve miniaturizing assays based on recognition of biomarker antigens with antibodies. This approach has inherent issues with time-sensitive pathologies because of the inherently slow speed of antibody-antigen interactions. Such an obstacle can be overcome through use of faster enzymatic reactions. In this work, we focused on creating an enzymatic based PoCT diagnostic platform suitable for time-sensitive pathologies, in particular addressing stroke. We hypothesize that by immobilizing enzymes to nanoparticles (NP) the enzymes will be stabilized and confined to a smaller volume, therefore increasing the efficiency of sequential enzymatic reactions needed to detect biomarkers at physiological and pathological levels in human serum and transduce that detection into a luminescent signal. Development of this platform involved several key steps, including immobilizing functional enzymes on inorganic surfaces and developing microfluidic systems with microliter-volume reactions. Because the use of immobilized enzymes in hybrid organic-inorganic devices is in a nascent stage of development, it is also essential to work out fundamental principles of how the inorganic scaffolds might affect the activities of the tethered enzymes.

Through biomimicry of the sperm flagellum, enzymes were designed to include a His-tag to bind with Ni-NTA groups on an inorganic surface in a precise orientation. This approach yielded higher specific activity than did attachment of the same enzymes through adsorption or chemically-specific binding (e.g. amine-carboxyl) techniques. While the orientation had dramatic impacts on the enzyme function, the surface size/curvature to which it is bound also influenced the enzyme function. Prior literature on this relationship was largely anecdotal. To identify generalizable truths regarding the

effects of the surface size and curvature on enzyme function, we used three enzymes, each representing a different class of enzyme, at maximal enzyme loading and in monolayers on gold NPs ranging in size from 5 to 50 nm in diameter. We found that larger NPs had increased enzyme multilayer formations and decreased k_{cat} and specific activity by 2.8 to 8.3 fold, depending on the enzyme. Contrary to other reports and suggesting an advantage for oriented immobilization, we did not see effects of size on the same enzymes when tethered in monolayers.

Tethering to NPs has immediate application in medical diagnosis of time-sensitive pathologies due to enzymes' rapid catalysis versus slow antibody interactions. Neuron specific enolase (NSE) is a biomarker for stroke, which we detected through the sequential reaction of tethered luciferase (Luc) and pyruvate kinase (PK), yielding a luminescent signal proportional to the concentration of enolase in our samples. In both rat stroke models and human patient samples, we found this diagnostic platform gave accurate results in 10 minutes compared to typical 4 hour ELISA tests, yet maintained a high correlation with the results from ELISA. In addition to NSE, we also utilized a tethered enzymatic reaction to detect phosphoglycerate mutase (PGM) at concentrations as low as 0.6 ng/ml. PGM is being investigated as a biomarker for stroke and myocardial infarction.

Lastly, we moved this technology into a PoCT platform by localizing them in microfluidic chip devices and stabilizing reactions at microliter volumes. This was accomplished with pluronic F108 as the cryogenic protectant during lyophilization of 10 μ l reactions. We produced the microchannel devices using SU-8 lithography and included a positive, negative and test channel. We demonstrated that these microfluidic cards with enzymes tethered to NPs in the reaction wells could detect enolase at physiological and pathological levels. Building on these advancements, we can now pursue a plethora of biomarkers to detect time-sensitive pathologies.

BIOGRAPHICAL SKETCH

James P. Lata was born July 5, 1986, in Tannersville, Pennsylvania. He received a Bachelor of Science in Bioengineering with a concentration in Material Science Engineering and a minor in Nanotechnology from The Pennsylvania State University (Penn State). He also received a Bachelor of Art in Physics with two minors in Mathematics and Chemistry from East Stroudsburg University (ESU). During his time at Penn State, James researched recombinant kinesin biomolecular motors under the tutelage of Dr. William Hancock. His projects focused on using novel engineering techniques with quantum dots to determine translational differences between a variety of kinesin constructs. James was recognized with several scholarships, including the Paul B. Shiring, Sr. Memorial Scholarship, Class of 1922 Memorial Scholarship, ESU Exceptional Academic Achievement Scholarship, Paul Kicska Outstanding Academic Achievement Scholarship, as well as notable awards from Sigma Xi. After graduation, James began his Ph.D. in the Department of Biomedical Engineering at Cornell University under the guidance of Dr. Alexander Travis. His research has been supported by the Travis lab through an NIH Pioneer Award.

ACKNOWLEDGMENTS

I am extremely grateful to my advisor, Dr. Alexander Travis, for his wisdom and patience. During my graduate career, I came to Dr. Travis with many far future ideas to which he needed to break down to the current feasibility of such projects. His guidance was one of respect and trust in my ability to act independently on all my ventures, even though a few ideas were not able to come to complete fruition. While independence was important, he also taught me to reach out and talk to experts in fields instead of trying to “reinvent the wheel”. It was through my discussions with Dr. Travis as a colleague and mentor that I became a successful scientist. I would also like to thank my committee members, Dr. David Erickson and Dr. Moonsoo Jin, for their insights during my thesis work. In addition, I had the privilege of collaborating with Dr. Nozomi Nishimura, Dr. Chris Schaffer, and Dr. Yash Agrawal, who have aided in bringing the diagnostic platform from bench-top to animal and preclinical application.

All of the experimentation was made possible through the support of an NIH Pioneer Award, CTSC Seed Funding, and a SUNY Health Now Planning Grant. The NIH Pioneer Award brought me into the lab and allowed me to work for all five years focusing on functionally tethering enzymes. The CTSC Seed Funding opened up collaborations with Weill Cornell Medical and NYC Presbyterian Hospital in order to obtain stroke patient samples for the initial phases of preclinical trials. Lastly, the SUNY Health Now Planning Grant involved multiple collaborators including Upstate Medical and Buffalo Medical to obtain patient samples for the first generation platform. Cornell University offered many unique facilities which trained me in nanobiotechnology including, the Nanobiotechnology Center (NBTC), Cornell NanoScale Science and Technology Facility, Cornell Center for Materials Research, and the Biotechnology Resource Center, with special thanks to Beth Rhoades who helped mentor me with my projects in the NBTC.

To my Travis Lab colleagues, I owe a great deal of gratitude for welcoming me into the lab and joining in on thought provoking discussions. Everyone in our lab was integral to my success as a graduate student by supporting me in so many ways: Dr. Roy Cohen, Dr. Chinatsu Mukai, Dr. Lizeng Gao, Jacque Nelson-Harrington and Jennifer Nagashima. It was a pleasure working with the nicest people, and the best work environment, one could wish for.

Finally, my family have always been motivating and supporting me through my graduate journey of highs and lows. Through their love and confidence in my abilities I want to thank: my parents, Marie and George; my sister, Holly; and my grandmother, Tida. Lastly, I would like to thank my friends at home and in Ithaca who have helped get me through my graduate years with needed merrymaking.

TABLE OF CONTENTS

| | |
|--|-----------|
| BIOGRAPHICAL SKETCH | v |
| ACKNOWLEDGEMENTS | vi |
| 1. CHAPTER 1: INTRODUCTION | 1 |
| 1.1 Tethered enzyme technology | 1 |
| 1.2 Pathology specific biomarkers | 4 |
| 1.3 Biomarker detection | 6 |
| 1.4 Point-of-care testing (PoCT) platform | 7 |
| 2. CHAPTER 2: EFFECTS OF NANOPARTICLE SIZE ON MULTILAYER FORMATION AND KINETICS OF TETHERED ENZYMES | 13 |
| 2.1 Introduction | 13 |
| 2.2 Materials and methods | 16 |
| 2.2.1 Gold nanoparticle surface modifications | 16 |
| 2.2.2 Functionalizing gold nanoparticles with tethered enzymes | 17 |
| 2.2.3 Calculations for enzyme layers | 17 |
| 2.2.4 Enzyme activity assays | 23 |
| 2.3 Results and discussion | 24 |
| 2.3.1 Oriented enzyme immobilization to varying sizes of gold nanoparticles | 24 |
| 2.3.2 Kinetic trends for an enzyme monolayer | 26 |
| 2.3.3 Effects multilayers have on enzyme kinetics | 33 |
| 2.4 Conclusions | 43 |
| 3. CHAPTER 3: USE OF TETHERED ENZYMES FOR RAPID BIOMARKER DETECTION – A PLATFORM TECHNOLOGY ENABLING POINT OF CARE DIAGNOSIS OF BRAIN PATHOLOGIES | 45 |
| 3.1 Introduction | 45 |
| 3.2 Materials and methods | 47 |
| 3.2.1 Experimental design | 47 |
| 3.2.2 Construction of His-Si4 fusion proteins | 48 |
| 3.2.3 Protein expression and purification | 48 |
| 3.2.4 Enzymatic activity assays | 49 |
| 3.2.5 Detection of NSE in rat stroke model | 49 |
| 3.2.5.1 Surgery and occlusion | 52 |
| 3.2.5.2 Fluoro-Jade C staining | 53 |
| 3.2.5.3 Measurement of rat brain infarct volume and torn tissue area | 53 |
| 3.2.5.4 Measurements of NSE activity and quantification by ELISA | 54 |
| 3.2.6 Detection of NSE in blood samples from human subjects | 54 |
| 3.2.6.1 Plasma sample collection | 54 |
| 3.2.6.2 Detection of NSE in plasma samples from human subjects | 55 |
| 3.3 Results and discussion | 55 |
| 3.3.1 Enzyme immobilization to silica nanoparticles imparts advantages to | 55 |

| | |
|--|------------|
| coupled enzymatic efficiency | |
| 3.3.2 Detection of biomarker NSE using sequential immobilized enzymes | 61 |
| 3.3.3 Detection of NSE in rat stroke models using tethered enzyme system compared to ELISA detection | 61 |
| 3.3.4 Detection of NSE in human plasma samples from patients using tethered enzymes compares to ELISA detection | 67 |
| 3.4 Conclusions | 67 |
| 4. CHAPTER 4: ORIENTED IMMOBILIZATION OF ENOLASE WITH AN APPLICATION IN PHOSPHOGLYCERATE MUTASE DETECTION | 71 |
| 4.1 Introduction | 71 |
| 4.2 Materials and methods | 75 |
| 4.2.1 Protein engineering | 75 |
| 4.2.2 Silica magnetic nanoparticle (SiMNP) synthesis | 76 |
| 4.2.3 Oriented enzyme immobilization | 77 |
| 4.2.4 Enzyme activity assays | 78 |
| 4.2.5 Statistical Analysis | 79 |
| 4.3 Results | 80 |
| 4.3.1 Protein engineering and optimization of enolase | 80 |
| 4.3.2 Enolase immobilization to SiMNPs | 80 |
| 4.3.3 Pyruvate kinase and enolase co-immobilization and sequential reactions | 80 |
| 4.3.4 Phosphoglycerate mutase diagnostic detection utilizing pyruvate kinase and enolase sequential reaction | 84 |
| 4.4 Discussion | 84 |
| 4.5 Conclusions | 87 |
| 5. CHAPTER 5: MICROFLUIDIC PLATFORM FOR TETHERED ENZYME DIAGNOSIS OF STROKE SPECIFIC BIOMARKER, ENOLASE | 89 |
| 5.1 Introduction | 89 |
| 5.2 Materials and methods | 92 |
| 5.2.1 Enzyme nanoparticle conjugation | 92 |
| 5.2.2 Enzyme activity assay | 94 |
| 5.2.3 Microfluidic chip designs | 94 |
| 5.2.4 Loading and Cleaning the Chip | 96 |
| 5.2.5 Statistics | 98 |
| 5.3 Results and discussion | 98 |
| 5.3.1 Miniaturization and lyophilization of enzymatic reaction | 98 |
| 5.3.2 Optimizations of the microfluidic chip design and implementation | 101 |
| 5.3.3 Detection of enolase in water and commercial human serum with microfluidic chip | 101 |
| 5.4 Conclusions | 108 |
| 6. CONCLUSIONS AND FUTURE DIRECTIONS | 109 |
| 7. REFERENCES | 113 |

CHAPTER 1

INTRODUCTION

1.1 Tethered Enzyme Technology

A fundamental challenge in producing hybrid organic/inorganic devices lies in interfacing biological components with inorganic materials while maintaining a high degree of functionality. Functionally tethering enzymes has several advantages, such as concentrating enzymes, spatially localizing reactions, and improving enzyme stability for increased shelf life^{1,2}. Applications for immobilized enzymes are seemingly limitless, including biocatalysis³, biofuel cells⁴, bioprocessing¹, biosensing^{5,6}, and drug delivery⁷. Enzymes are proteins which have a complex and fragile tertiary and quaternary structure to perform biocatalysis. The difficulties in immobilizing enzymes while maintaining function are three fold: 1. The enzyme needs to retain the ability to undergo necessary conformational changes; 2. The catalytic and cofactor binding domains need to be readily accessible; 3. The enzyme must maintain proper folding and not undergo denaturation^{8,9}. Commonly employed immobilization strategies include random protein adsorption directly to a surface and chemically-specific crosslinking to surface molecules¹⁰. Random protein adsorption is highly dependent on intermolecular forces between the enzyme and the surface (Fig. 1.1 a). This technique is a very crude and easy way to attach enzymes; however, the activity of these enzymes are greatly diminished¹¹. Enzymes which are randomly adsorbed can partially or completely denature once contact is made with a solid support. Secondly, the surface can block the catalytic and cofactor binding domains of the enzyme. Also, the enzyme can have steric hindrance with the surface which will impair conformational changes¹². Lastly, over time enzymes can leach off the solid support. To resolve some of these problems, a chemically-specific crosslinking technique was developed which allowed specific areas of the enzyme to permanently bind with molecules on the solid surface.

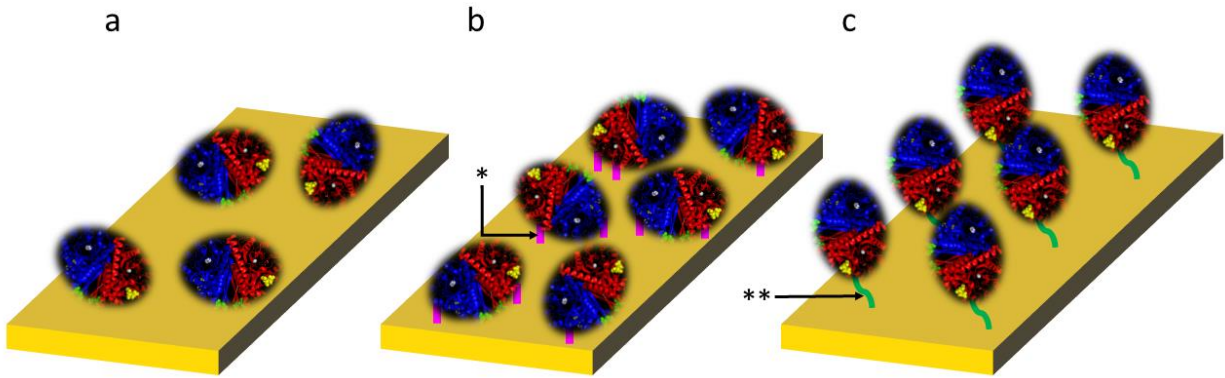


Figure 1.1: Techniques to immobilize enzymes to inorganic surfaces. Through (a) non-specific adsorption an enzyme is attracted via charges present on the surface, this forces the enzyme to come into direct contact with the surface, impairing conformational changes and blocking catalytic domains. An improved immobilization technique (b) chemically binds an enzyme through specific groups on the enzyme's surface with modified groups on the support (*). This technique can still block catalytic domains and bind to multiple locations on an enzyme, therefore hindering conformational changes. Therefore, (c) specific, oriented immobilization was implemented to tether an enzyme to a single location to the surface (**). The tether helps prevent the enzyme from coming into direct contact with the surface, allowing conformational changes and leaving catalytic domains accessible.

One common example is to chemically modify a surface with carboxyl groups which will covalently bind with the amine groups found on an enzyme through 1-ethyl-3-(3-dimethylaminopropyl) carbodiimide hydrochloride (EDC) chemistry (Fig. 1.1 b) . This binding strategy yields much more stable enzymes than random adsorption, however it also possess several disadvantages. The chemistries can be very harsh and thus the environmental impacts on the enzymes can cause loss of activity. Enzymes can be bound to the surface via more than one amine group on an individual enzyme, which will hinder conformational changes, block catalytic domains, and reduce the degrees of rotational freedom compared to non-tethered counterparts. To overcome the weaknesses of these two approaches, we investigated chemically specific, oriented immobilization of enzymes.

Adopting a biomimetic strategy, inspired by sperm, enzymes can be tethered to solid surfaces in an oriented fashion and through a single anchoring point on an enzyme. Through evolution, mammalian sperm have developed a localized energy production scheme in the principal piece of the flagellum using tethered glycolytic enzymes¹³⁻¹⁵. The sperm tail has a streamlined shape which limits cytosolic space, therefore enzymes could not freely reside in a fluid phase, but instead are tethered in a solid state to a cytoskeletal element known as the fibrous sheath^{16, 17}. The fibrous sheath is a ribbed structure which runs the length of the principal piece and was previously thought to be mainly used for structural support. Several of the glycolytic enzymes are tethered through a germ cell specific (gcs) domain positioned at the enzyme's N-terminus. Through protein engineering and rational design, we have removed the gcs sequence and replaced it with an affinity tag, such as a hexahistidine tag (His-tag) or silica-binding tag (Si-tag), for binding of the enzyme with a specific molecule or material (e.g. Ni-NTA), on an inorganic surface^{18, 19}. This tethering strategy allows the enzyme to be specifically tethered through the N-terminus without impeding conformational changes, inducing tertiary structure denaturation, or blocking binding sites (Fig. 1.1 c). This strategy also allows for enzyme multimer formations since it includes a linker which reduces the chance for the enzyme to come into direct contact with the surface.

We have shown that this specific, oriented immobilization via genetically-encoded binding domains conferred advantages in specific activity versus either random adsorption or chemically-specific binding^{18, 19}. We have also expanded this technique to many different somatic enzymes without a gcs sequence, placing the tag at either the N- or C-terminus with similar advantageous results.

This dissertation focuses on the specific, oriented immobilization of enzymes to a variety of different nanoparticles (NP). NPs are an ideal scaffold for enzyme binding considering they can be used in a plethora of biotechnology applications²⁰⁻²³. They possess high surface to volume ratios and dispersibility, and can be easily integrated into various devices with spatial control. The curvature of the NPs is an attractive feature since it gives tethered enzymes increased range of motion compared to planar surfaces, and likely increases the accessibility of cofactor and substrate binding sites on the enzymes so they can be approached by molecules in solution from a wider arc of approach. Throughout this dissertation our tethered enzyme technology will be used to look into fundamental questions, such as how nanoparticle size effects enzyme efficiency, as well as advances in hybrid organic/inorganic devices for biomarker detection and disease diagnosis.

1.2 Pathology Specific Biomarkers

Certain pathologies are time-sensitive, requiring prompt diagnosis for treatment to be effective and/or prevent irreversible damage or death. Ischemic stroke is an example of a time-sensitive pathology with only a 3-4 hour window post event for diagnosis and treatment. It is one of the leading causes of mortality and long-term disability in the United States. Over 750,000 people a year are affected by stroke, killing 136,000 and leaving many others permanently disabled²⁴. Current diagnosis methodology for stroke is time consuming and expensive, and facilities with specialists at its diagnosis are rare. The current medical paradigm is to first transport the patient to a neurological facility, which are found in only 33% of counties in the US²⁴. Next, the patient undergoes a labyrinth of tests performed

by a neurologist to rule out stroke mimics, such as transient ischemic attacks, migraines, epilepsy, electrolyte abnormalities, and mass lesions²⁵. Once the patient has been confirmed to have a stroke, the type of stroke, either ischemic or hemorrhagic, is identified by advanced imaging tests, computed tomography (CT) and/or magnetic resonance imaging (MRI). The type of stroke is extremely important as the treatment for ischemic stroke, tissue plasminogen activator (TPA), is contraindicated in the case of hemorrhagic stroke²⁶. Even with expensive imaging, micro-strokes that occur in small vessels can be overlooked and misdiagnosed. This current paradigm is unsatisfactory considering stroke only has a 3-4 hour window at which TPA can be effectively administered. After this time point irreversible neurological damage starts to take effect. Due to the clinical need, much attention has focused on alternative methods to diagnose stroke and other time-sensitive pathologies with a quick and easy test following hospital admission or at the scene of the event.

Significant research effort is being dedicated to the identification and detection of pathology-specific biomarkers²⁷. After a pathological event, molecules are released into the blood stream, cerebral spinal fluid and/or urine which are unique to the event. These markers typically come from intracellular components after cell damage/death, or exposure to changes in the cellular environment such as hypoxic conditions. A large number of molecules have been studied for their potential to provide clinically relevant diagnostic and prognostic information regarding stroke²⁸. Although results from a panel of biomarkers would be required to give a definitive diagnosis, neuron-specific enolase (NSE) is one of the most studied biomarkers for its appearance in the blood following many different neurological brain pathologies, including stroke^{29, 30}. NSE has also proven to distinguish between stroke mimics. Due to the potential significance of NSE in diagnosing stroke, it is a worthy first step biomarker for diagnostic detection. In addition to NSE, there are a few other important stroke biomarkers³¹ which we are attempting to detect, such as S100 β , GFAP (glial fibrillary acidic protein) and PGM (phosphoglycerate mutase)^{32, 33}.

1.3 Biomarker Detection

There exists a pressing need for biomarker detection for time-sensitive and difficult to diagnose pathologies. Biomarkers that have been identified need to be transitioned to clinical validation testing for further evaluation³⁴. Traditionally, blood biomarker detection is based on results from enzyme-linked immunosorbent assay (ELISA), polymerase chain reaction (PCR), and/or mass spectrometry³⁵. While these technologies are accurate at detecting specific stable biomarkers which do not degrade over time, they also require sample preparation, sophisticated instrumentation, trained operators, and a good deal of time and money. In the hospital setting, automated ELISA is by far the most common of the techniques. A standard ELISA requires lengthy incubations for antibody-antigen interactions to occur, and multiple washing steps. Together, the full protocol takes approximately four hours³⁶. With time-sensitive pathologies, such as stroke, which need to be diagnosed within 3-4 hours of onset, this detection strategy is unacceptable. To improve on this technology there have been many reports using lateral flow assays with antibody capture; however, these have low sensitivity and have not yet overcome the necessary time constraints³⁵. Other methods of detection warrant investigation.

In Chapters 3 and 4 of this dissertation, we describe investigations of a new way to detect biomarkers and give a prompt and quantifiable result. We utilize oriented immobilization of coupled enzymatic reactions on NPs with a bioluminescent readout for the detection of NSE and PGM in human serum. Enzyme biocatalysis is orders of magnitude faster than antibody based interactions³⁷, resulting in a fast detection without long incubation steps. The bioluminescent readout allows for simple instrumentation, consisting of a photodiode detector, without a need for any bulky excitation source. Operation for this detection strategy is simple, without requiring wash steps, reagent additions, device calibration, or difficult instrumental handling. This assay works in a 96-well plate format compatible with existing plate readers capable of luminometry. Plasma is added to an enzymatic mixture pre-loaded and lyophilized in the wells, and then placed into the plate reader. After ten minutes, results are given and a

simple analysis quantifies the concentration of biomarker in the given sample. These reactions are designed per biomarker, much like with an ELISA, but the biomarker must ultimately be amenable to being detected by an enzymatic cascade. This is not as difficult as it might seem, as many biomarkers are either themselves enzymes, such as NSE and PGM, or the biomarker increases or decreases an enzyme's activity, such as S100 β . The use of coupled enzyme reactions to detect analytes has been around for decades^{38, 39}, and indeed is the basis for the most common PoCT—the glucometer. However, almost all recent attention has focused on antibody-capture based approaches. Avoidance of enzyme-based technologies is due to several factors, including the need to produce and purify the enzymes needed, maintain their function when tethered, and be able to store them long term.

1.4 Point-of-Care Testing (PoCT) Platform

The end goal for diagnostics is to create a device which can be used by the patient or caregiver at the scene of an incident. This device would be as simple to use as a glucometer for diabetic patients, but give quantitative results for the diagnosis of multiple pathologies, and possibly be able to transfer these results wirelessly to a physician or diagnostic specialist for further analysis. This concept of “telemedicine” is of particular interest for time-sensitive pathologies as it would reduce many of the most time-consuming steps currently involved in stroke diagnosis such as transportation to a stroke clinic (often bypassing closer medical facilities), neurological assessment, MRI/CT scans, as well as long and complicated blood work analysis. The ideal device would be able to detect femtomolar amounts of multiple biomarkers taken from low microliter volumes of blood and send encrypted results to an electronic health record within minutes. Such a device should be portable, disposable and cost under a dollar⁴⁰. This device is still “far future,” however having a PoCT device for the diagnosis of one pathology is more conceivable and could have a tremendous impact on medical practice.

Microfluidic systems have been extensively researched regarding diagnostic applications.

Microfluidic devices can be classified by the way fluid is transported through the device, which can be either active or passive transport. In active transport there exists some external change needed to move the fluid. Some examples of valves and pumps which have been designed for active transport include: 1) pneumatic PDMS^{41, 42}, in which a deformable material is pressed to close perpendicularly crossing channels; 2) screws, pneumatic tubing, or solenoids⁴³, which reliably close or open channels in deformable materials with applied force, voltage or pressure; 3) magnetic inductors⁴⁴, magnets which can reversibly pull a metal plated channel to allow flow; 4) reciprocating movement membrane valves⁴⁵, in which a piezoelectric pump can compress or decompress fluid to flow into, and be directed by, membrane valves; 5) electro-osmotic flow⁴⁶, in which an applied electrical current charge is displaced in the fluid and creates a pressure gradient; 6) centrifugal force^{47, 48}, in which the entire device is rotated at specific speeds to push the fluid from the inner side of the device to the outer side; or 7) electrowetting⁴⁹, in which pulses of electrical potential change the surface from hydrophobic to hydrophilic; this is mainly used for water bubble manipulations.

On the other hand, passive transport utilizes innate properties and the design of the device to move fluid through the device without external assistance. Examples of passive valves and pumps include: 1) capillary driven flow⁵⁰, in which valves created in the channel design stop flow using the meniscus of the fluid and can allow it to continue when a connecting flow breaks the surface tension; 2) hydrophobic barriers⁵¹, in which regions in the device are made hydrophobic and when amphipathic components bind with the hydrophobic region, changing it to be hydrophilic, the fluid can move through the region; 3) pH controlled flow⁵², in which hydrogels expand or contract depending on pH conditions and can stop or continue flow; 4) porous capillary membranes^{53, 54}, in which a porous membrane wicks fluid throughout the device; 5) capillary pumps⁵⁵, in which micropillars in a hydrophilic device allow for autonomous flow which can be controlled by the positioning of the micropillars; or 6) vacuum-driven

flow⁵⁶, in which an external vacuum induces flow by dissolving the air trapped in a channel made from a gas permeable material.

Another defining aspect of a PoCT diagnostic platform is the nature of receptors used to detect pathology-specific biomarkers. All of the methods thus far have used capture techniques which increase the density of biomarkers for signal transduction, these include: 1) oligonucleotides with attached antibodies⁵⁷, oligonucleotide with antibodies to capture biomarkers are incubated and concentrated in a section in the device with a complementary oligonucleotide; phages⁵⁸, 2) bacteriophages are used to produce a variety of proteins on their surface which interact with specific biomarkers; 3) self-assembled monolayers⁵⁹, in which chemical modifications on a surface can capture receptors which in turn bind with biomarkers; or 4) supported lipid bilayers⁶⁰, in which antibodies are bound to ion channels in a lipid bilayer and when the biomarker binds to the antibody the ion channel opens changing the conductance of the membrane.

Lastly, how the signal is transduced will have dramatic implications for the detector unit and sensitivity of the diagnostic approach. Signal transduction for a microfluidic PoCT device can be separated into labeled or label-free transduction. In labeled transduction, particles or molecules are used to bind with the biomarkers and are detected/quantified through various methods including: 1) colorimetry⁶¹, aptamer or antibody conjugated gold nanoparticles are visible once bound to an antigen; 2) fluorescence⁶², fluorescent markers are bound through antibodies to biomarkers and detected with a CCD camera; 3) reflective⁶³, much like fluorescence but using silver nanoparticles and detecting reflected light; 4) optomagnetic⁶⁴, magnetic fields manipulate magnetic nanoparticles attached to antibodies bound to biomarkers and the light reflected off the surface is detected; or 5) electrochemical⁶⁵, in which the charge on an electrode is changed with reducing or oxidizing reagents activated by the biomarkers.

Label-free transduction can directly detect the markers without the need for labeling, some examples include: 1) surface plasmon resonance⁶⁶, in which biomarkers attached to a metal film change

the surface plasmon resonance in the metal; 2) resonant optical waveguides⁶⁷, in which changes in optical resonance are detected after biomarker binding; 3) nanowire field effect transistors⁶⁸, in which biomarkers bound to a gap in these transistors can change the conductance between the source and drain; and 4) cantilevers⁶⁹, which can be used as either resonators, measuring the mass of the bound biomarker, or through deflection of the cantilever from surface stress by binding of the biomarkers. While a great deal of progress has been made in the diagnostic implementation of microfluidic systems, these devices still have not broken into the market, due to a combination of lack of clinical data, sensitivity and/or reproducibility. All of these previous devices used antibody capture for signal transduction. Utilizing enzymatic reactions with a bioluminescent readout in a microfluidic device has not been attempted, and we believe is where improved sensitivity and reproducibility can be obtained in order to advance microfluidic PoCT devices to market.

In Chapter 5 of this dissertation, we attempt to minimize required sample sizes and enhance portability of our tethered enzyme detection strategy by integrating it into a multichannel microfluidic platform. If ultimately successful, this would allow our technology to be used as a platform for various PoCT devices by paramedics, athletic trainers, medical assistants, or military personnel in diverse field settings. Utilizing tethered enzymes in a microfluidic-based PoCT device has multiple advantages over antibody-based approaches. These advantages include: 1. Speed - enzymatic reactions occur thousands of times faster than antibody-antigen interactions; 2. Luminescence-based readout - enables stand-alone, highly portable devices that do not require bulky excitation elements, such as with fluorescence or absorbance; 3. Sensitivity - enzymatic reactions facilitate signal amplification at the steps of both detection and readout; 4. Reduced cost of fabrication – NPs and microchannel chips are made from inexpensive materials and can easily be mass produced; 5. Small sample size - the rapid enzymatic detection with the microchannel design only requires nanoliter amounts of plasma per channel; 6. Accurate quantification – utilizing positive and negative controls built in with the test channel allows for

calibration and noise/background reduction; 7. Multiplex capability - coupled biochemical reactions can detect multiple biomarkers through a spatially-defined luminescence readout; and 8. Robust and portable - the chip/reader system as a whole could be small and portable because it would not require an excitation light source. Our fabrication strategy for these microfluidic chips uses SU-8 lithography methods to make a 3 channel-device capable of measuring one biomarker at a time. This is the first generation of our device, and thus still uses a plate reader to detect the signal, however it is relatively straightforward to conceive a portable custom reader for these chips (Fig. 1.2).

In conclusion, our PoCT platform has the potential to transform medical practice by providing accurate and quantitative biomarker assessments before the patient arrives to the hospital. While in transit or at the scene, a paramedic can draw blood and run it through our device which will give a quantitative answer to stroke, and possibly the type/size of stroke. In the case of an ischemic stroke the patient can immediately receive TPA; in the case of a small stroke, and possibly hemorrhagic strokes, the patient can immediately go for MRI, bypassing the need for the initial neurology assessment and saving precious time.

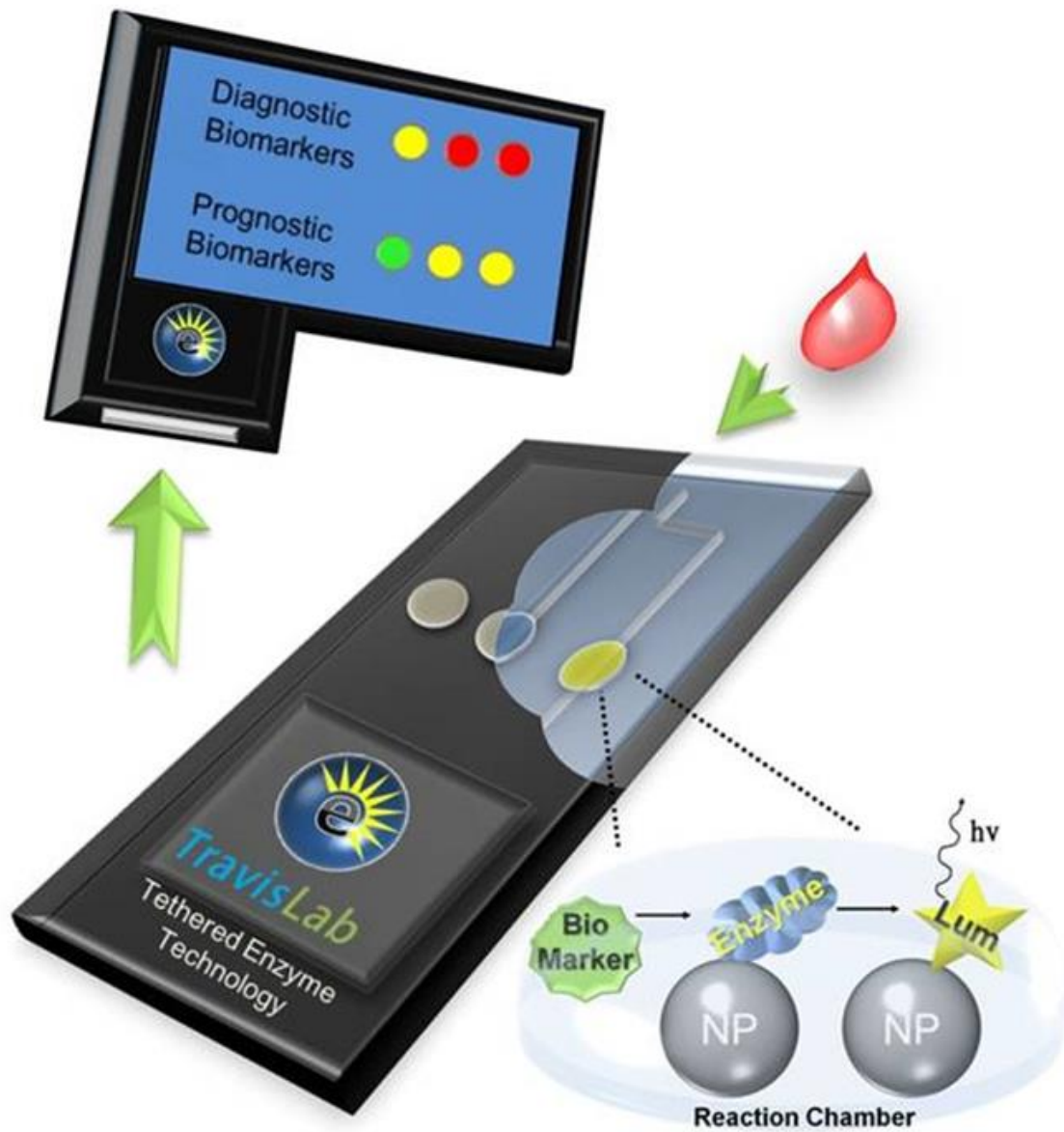


Figure 1.2: Schematic for a future PoCT device utilizing tethered enzymes in a microfluidic chip.

With a drop of blood this hypothetical device would be able to test for biomarkers present through sequential tethered enzyme reactions within a microfluidic chip. The chip could be inserted into a handheld detector unit which would display diagnostic and possibly prognostic information depending on the biomarker concentrations.

CHAPTER 2

EFFECTS OF NANOPARTICLE SIZE ON MULTILAYER FORMATION AND KINETICS OF TETHERED ENZYMES[‡]

2.1 Introduction

NPs have many positive attributes for use in biotechnological applications, including dispersibility, high surface area, and the ability to be integrated into various devices with spatial control. Applications for NPs with attached enzymes include biocatalysis³, biosensing⁵, biofuel cells⁴, disease diagnosis⁶, and drug delivery⁷. Because enzyme attachment can block substrate binding sites or interfere with necessary conformational changes⁸, much attention has focused on surface attachment chemistry⁷⁰. However, other variables can also exert profound influences on tethered enzyme function, but surprisingly have been rarely studied.

Surface composition, geometry, roughness, porosity and sub-nanometer morphology can all impact surface modifications and/or enzyme binding^{22, 71}. In addition, surface charge can have dramatic effects on the enzymes bound^{11, 72}. Characteristics of the medium in which the conjugates are suspended such as pH, temperature, viscosity, and salt concentrations can also impact enzyme function^{73, 74}. Many enzymes form functional multimers and can bind with one another to create multilayers, dependent on protein surface charge, size, tertiary and quaternary structure, and packing density. Multilayer formation and tethered enzyme activity can also be affected by NP size and surface area, thereby affecting the performance of functionalized NPs across diverse applications. Despite this fundamental importance, there has been relatively little study of the effect of NP size on the function of different types of immobilized enzymes.

The few notable studies investigating the effects of NP size on activity have typically utilized single enzymes at less than 50% surface coverage. The many technical differences among these studies

[‡] Modified from Lata JP et. al. Manuscript submitted for publication.

resulted in varying findings regarding K_M , k_{cat} and specific activity (Table 2.1)^{11, 21, 74, 75}. These studies were all limited to single enzymes and used attachment strategies, such as non-specific binding and specific, non-oriented binding, which were sub-optimal for retaining enzymatic activity. Coupled with use of different NPs of different size ranges, as well as use of varying measurements to quantify activity, these differences limit one's ability to draw generalizable conclusions about the impact of NP size on function. To date, no reports have provided fundamental understanding of the impacts of NP size on the activity of multiple enzyme classes standardizing surface attachment chemistry, NP composition, and kinetic analysis, with consideration of multilayer formation under conditions of maximal enzyme loading. This aspect is critical for practical application of these technologies, as maximum function per NP reduces the overall amount of NPs needed.

Previously we showed that biomimetic oriented immobilization yielded higher specific activities versus non-oriented adsorption or carboxyl-amine binding^{18, 19}. Here, we standardized NP attachment strategy (oriented immobilization via hexahistidine tags) and composition (Ni-NTA coated gold NPs), to test the impact of NP size (\varnothing 5, 10, 20 and 50 nm) on multilayer formation, activity and kinetic parameters (k_{cat} , K_M , k_{cat}/K_M) of enzymes representing three different classes: glucose-6-phosphate isomerase (GPI), an isomerase; glyceraldehyde-3-phosphate dehydrogenase S (GAPDHS), an oxidoreductase; and pyruvate kinase (PK), a transferase.

To standardize surface attachment chemistry to the NP, we chose oriented immobilization using genetically-encoded hexahistidine tags (His-tag). Unlike random adsorption, or chemically-specific but non-oriented approaches such as carboxyl-amine binding (the two most common approaches), genetically-positioned binding tags facilitate immobilization in a specific orientation. This reduces the impact of subtle (sub-nm) morphological surface variation and the parts of the protein that come into direct contact with the surface, a common problem with non-specific adsorption of enzymes¹¹. Unlike

Table 2.1: Prior Studies Involving Effects of NP Size on Bound Enzyme Activity

| First Author | Enzyme | Binding | NP Composition | NP Size (nm) | k_{cat} (s^{-1}) | K_M (μM) | k_{cat}/K_M ($s^{-1}\mu M^{-1}$) | Specific Activity (U/g protein) | Relative Activity (%) at 100 nm ² Surface Area |
|-------------------------------------|------------------------|------------|--------------------------------|--------------|------------------------|-------------------|--------------------------------------|---------------------------------|---|
| Jia et al., 2003 ¹³ | α -chymotrypsin | Amine | Polystyrene | 110 | 20 | 31.7 | 0.63 | NA | NA |
| | | | | 270 | 18.6 | 40.9 | 0.46 | NA | NA |
| | | | | 490 | 19.4 | 66.4 | 0.29 | NA | NA |
| | | | | 1000 | 15.4 | 63.7 | 0.24 | NA | NA |
| Wu et al., 2011 ¹⁴ | candida rugosa lipase | Adsorption | Gold | 13.1 | 18 | 9.5 | 1.89 | NA | NA |
| | | | | 25.2 | 18.3 | 14.1 | 1.3 | NA | NA |
| | | | | 37.5 | 19.6 | 15.7 | 1.25 | NA | NA |
| | | | | 50.8 | 19.1 | 17.1 | 1.12 | NA | NA |
| | | | | 69.6 | 17.9 | 18.1 | 0.99 | NA | NA |
| Park et al., 2011 ¹⁵ | glucose oxidase | Amine | Fe ₃ O ₄ | 5 | NA | NA | NA | 5800 | NA |
| | | | | 26 | NA | NA | NA | 5100 | NA |
| | | | | 51 | NA | NA | NA | 3800 | NA |
| Vertegel et al., 2004 ¹¹ | chicken egg lysozyme | Adsorption | Silica | 4 | NA | NA | NA | NA | 65 |
| | | | | 20 | NA | NA | NA | NA | 42 |
| | | | | 100 | NA | NA | NA | NA | 38 |

the more common binding approaches, genetically encoded tags can be positioned to allow access to the substrate binding domain and any needed conformational changes^{20, 76}. In our previous studies^{18, 19}, we showed that this strategy led to higher specific activities than the same enzymes when randomly adsorbed or attached via carboxyl-amine binding.

2.2 Materials and Methods

All materials and reagents were purchased from Sigma-Aldrich (MO, USA) or ThermoFisher Scientific (MA, USA) unless otherwise stated.

2.2.1: Gold Nanoparticle Surface Modifications. AuNPs were purchased from Sigma-Aldrich and the preparation of AuNPs used a tannic acid/citrate reduction protocol, thus the surface had mostly tannic acid with some citrate. All modifications of AuNPs were carried out in 0.1 mM PBS solution. AuNPs were incubated with 11-mercaptoundecanoic acid (0.1 mg/ml dissolved in 95% ethanol) for 24 hours at room temperature. Then, 10 μ l of NaCl (2M) were added every 30 min, for a total of three additions, and incubated for 3 hours on a rocker at room temperature. Modified AuNPs were then washed three times by centrifugation (16,000 g for 20 min at 4°C) and re-suspension in 0.1 mM PBS. The carboxyl groups were activated with 1-ethyl-3-(3-dimethylaminopropyl) carbodiimide (EDC 0.5 mg/ml) and N-hydroxysuccinimide (NHS 0.2 mg/ml) solution incubated at room temperature for 1 hour. This mixture was then centrifuged and the AuNPs washed three times with 0.1 mM PBS. Next, *N,N*-bis(carboxymethyl)-L-lysine hydrate (NTA 0.5 mg/ml) was added to the AuNPs and incubated for 3 hours at room temperature. This derivative of NTA includes an additional amine group which can react with the carboxyl groups on the surface. Then NiCl₂ (0.5 mg/ml) was added to the mixture to chelate the NTA. After 1 hour, the NTA-AuNPs were washed three times by centrifugation and re-suspension into

0.1 mM PBS. The AuNPs were characterized before and after NTA modification using SEM (MIRA3 LM FESEM, Tescan) with backscatter electron detection at an acceleration voltage of 10 kV for 50, 20, 10 nm AuNPs and 30 kV for 5 nm AuNPs (Fig. 2.1). A Zetasizer ZS (Malvern) was used to measure zeta potential distributions before and after NTA modification (Fig. 2.2).

2.2.2: Functionalizing AuNPs with Tethered Enzymes. Recombinant GPI and GAPDHS were generated and their identity, relative purity, and activities verified using our previous methods^{18,19}. Recombinant PK was generated from mouse testis RNA using the same methodology. Each recombinant enzyme was diluted to a working concentration of 0.1 mg/ml. Tethering was performed by incubating at 4°C for 1 hour using 30 µl of enzyme with 150 µl of NTA-AuNP ($\sim 4 \times 10^{12}$ nm²/µl), for each of the four sizes, or 20 µl of enzyme with 20 µl of NTA-AuNP (OD = 1), for monolayer and multilayer experiments respectively. The NTA-AuNPs with bound enzymes were then washed three times with 0.1 mM PBS with final re-suspension in 120 µl (monolayer), or 40 µl (multilayer), of 0.1 mM PBS. Amount of protein bound was calculated by subtraction of the unbound from the total (Supplementary Figs. 2.3 & 2.4). GPI tethered to NTA-AuNPs, using the multilayer approach, was evaluated using TEM (Tecnai 12 Bio-Twin TEM, FEI) at 120kV (Fig. 2.5 d-g) with a phosphotungstic acid negative stain; the enzyme layers were measured using ImageJ (NIH). In calculating multilayers for each NP size, the enzyme thickness was normalized to the 5 nm NP's enzyme thickness, which was assumed to be a monolayer and which was corroborated by geometric calculations below. This took into consideration drying effects in sample preparation for TEM.

2.2.3: Calculations for Enzyme Layers. Enzyme size was estimated using similar crystal structures of each functional multimer taken from the RCSB Protein Data Bank (GPI from mouse: 1U0E, GAPDH from rabbit: 1J0X, PK from rabbit: 1F3W). We utilized spherical approximations for each multimer (GPI: 43.92 nm², GAPDHS: 56.76 nm², PK: 104.00 nm²). The contact points of adjacent multimers were assumed to

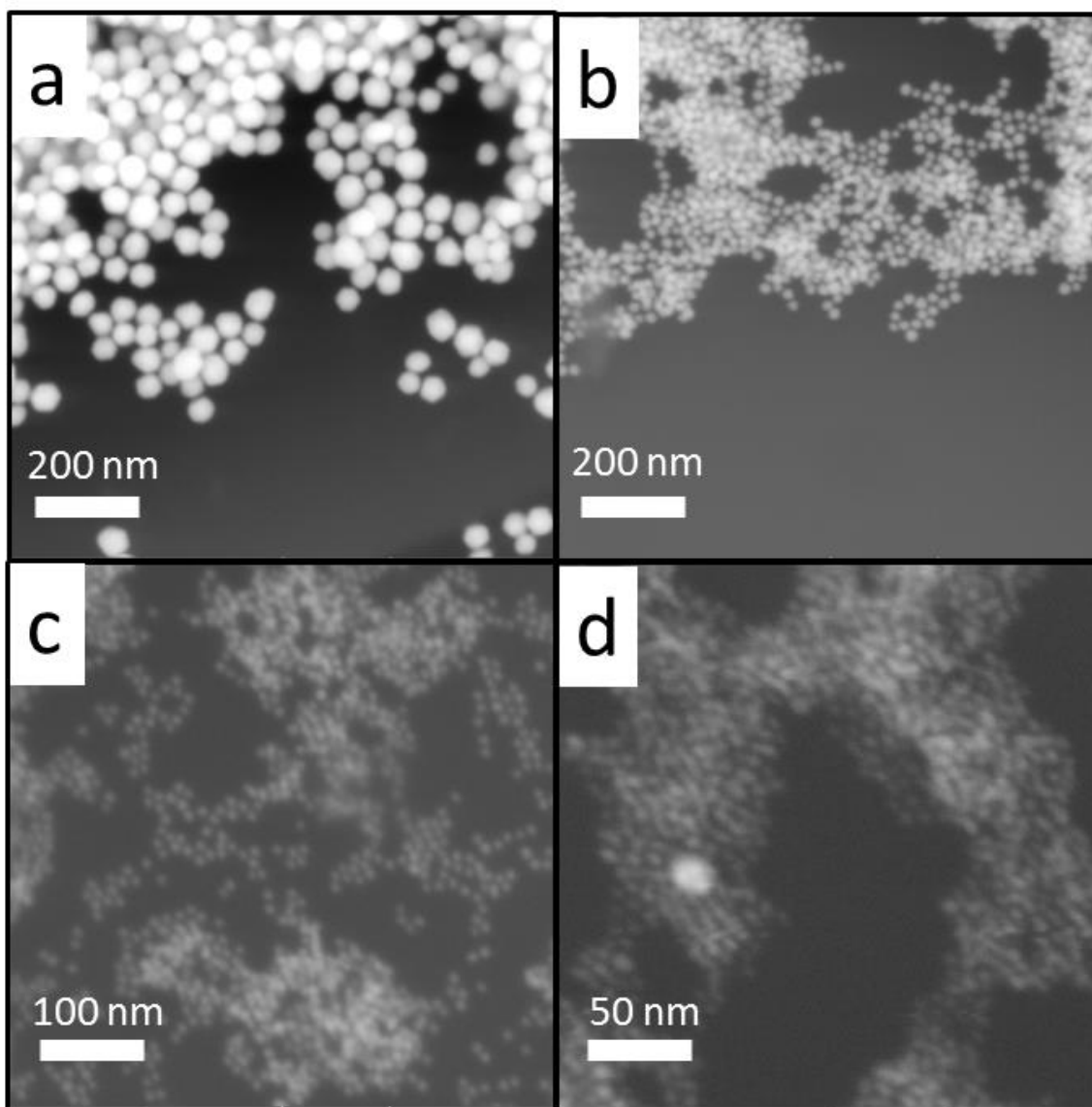


Figure 2.1: Size verification of NTA-AuNPs. NTA modified AuNPs [50 nm (a), 20 nm (b), 10 nm (c) and 5 nm (d)] were dried and SEM used to verify size distribution.

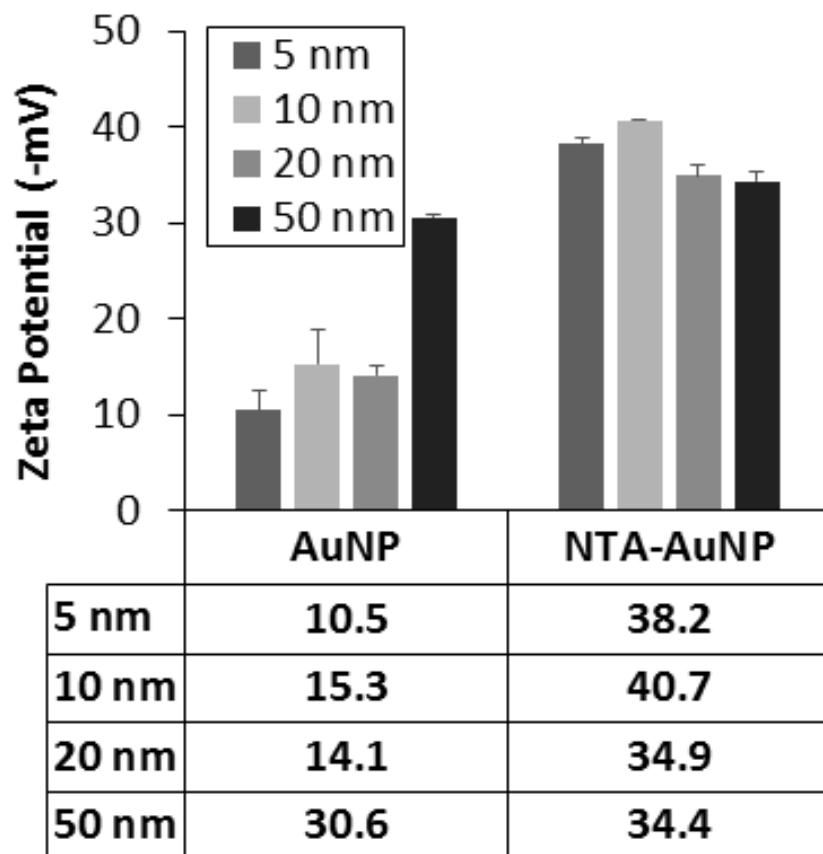


Figure 2.2: Zeta potential was used to determine aggregation of non-modified and modified AuNPs.

AuNPs were analyzed using Malvern Software before and after Ni-NTA modification. These data suggest that the larger AuNPs were more stable in suspension than their smaller counterparts. After Ni-NTA modification, all sizes of AuNPs were stabilized at lower zeta potentials, reflecting lower likelihood of aggregation. Error bars show standard deviation. Comparison of AuNP results with those from NTA-AuNP were performed using a Student's *t* test with unequal variance (Excel), and are significant at $p < 0.05$.

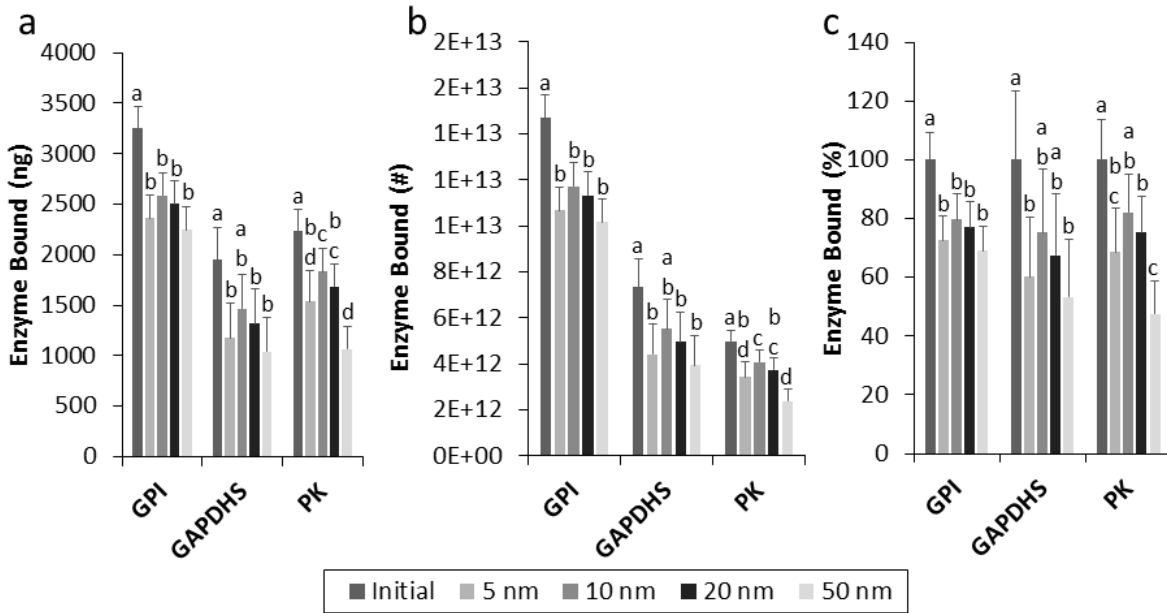


Figure 2.3: Amount of enzyme bound to AuNPs using monolayer approach calculated with BCA Protein

Assay. Enzymes were allowed to bind with the different size AuNPs. Enzyme-NP conjugates were washed three times with the amount of unbound protein in each wash measured. Via subtraction from the initial amount added, we were able to calculate (a) the mass amount of enzymes bound to AuNPs as well as (b) the number of enzymes bound and (c) the percentage bound. Error bars show standard deviation. Comparisons among sizes for a given enzyme were performed using a Student's *t* test with unequal variance (Excel); dissimilar letters denotes significance at $p < 0.05$.

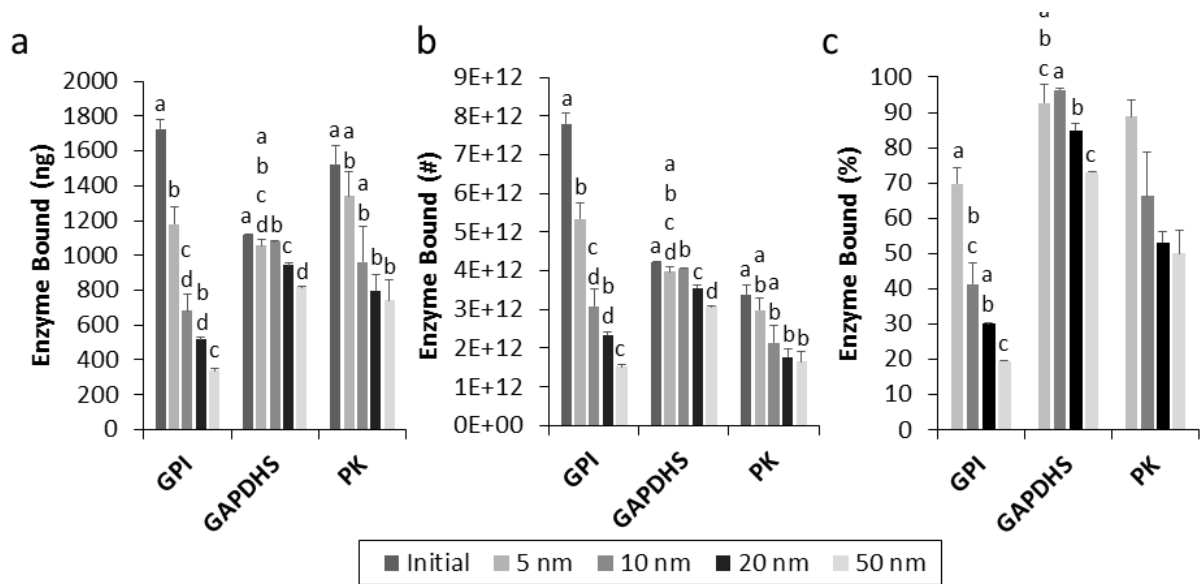


Figure 2.4: Amount of multilayer enzyme bound to AuNPs calculated with BCA Protein Assay. Enzymes were allowed to bind with the different size AuNPs. Enzyme-NP conjugates were washed three times with the amount of unbound protein in each wash measured. Via subtraction from the initial amount added, we were able to calculate (a) the mass amount of enzymes bound to AuNPs as well as (b) the number of enzymes bound and (c) the percentage bound. Error bars show SEM. Comparisons among sizes for a given enzyme were performed using a Student's *t* test with unequal variance (Excel); dissimilar letters denotes significance at $p < 0.05$, no letters indicate no significance.

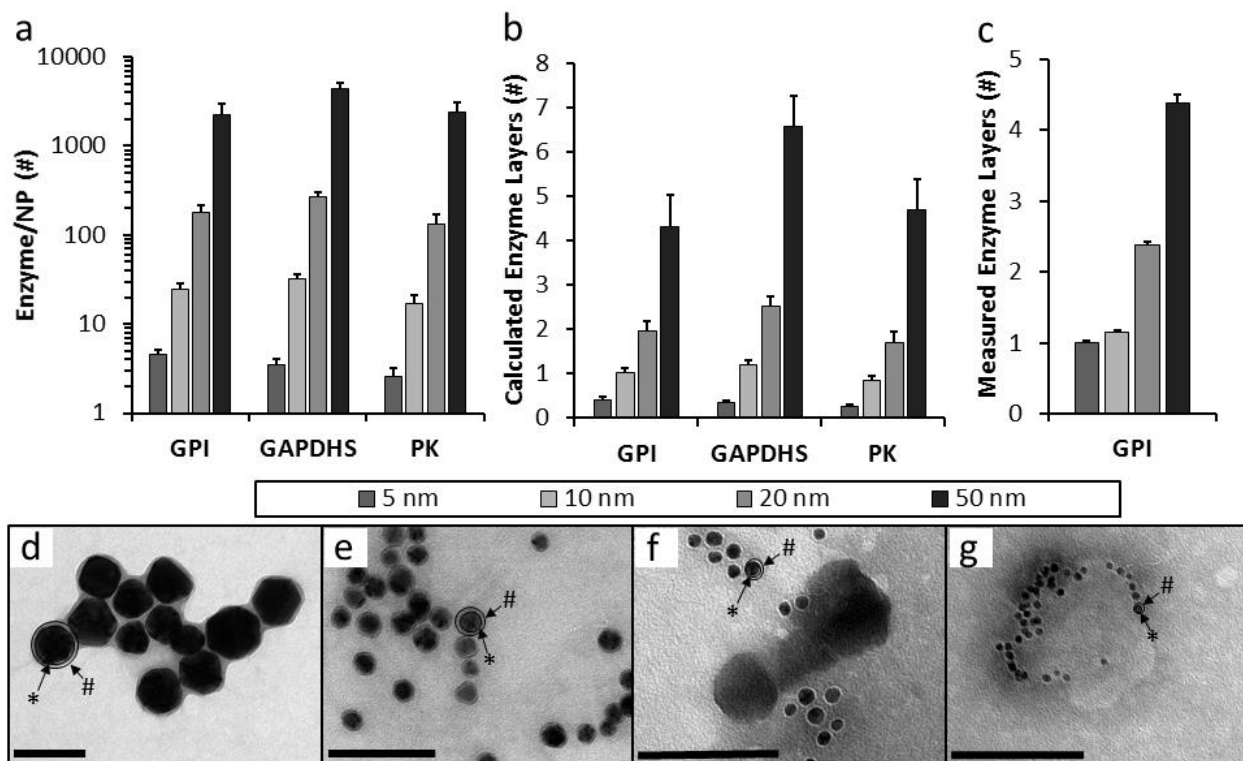


Figure 2.5: Binding and multilayer results for enzymes on NTA-AuNPs. (a) The amount of protein bound was calculated from measurements of total protein minus unbound protein and is plotted as the number of enzymes per NP for the three enzymes (GPI, GAPDHs, PK) on four sizes of AuNPs (ϕ 5, 10, 20 and 50 nm). (b) Based on the diameter of each enzyme as a functional multimer (assuming a spherical shape), and the AuNP surface area, we calculated the number of enzyme layers per NP. (c) For GPI, we then verified our calculated number of layers by measuring the thickness of the protein shells around each NTA-AuNP using TEM. In the images of GPI tethered to the different sized NTA-AuNPs [50 nm (d), 20 nm (e), 10 nm (f) and 5 nm (g)], the protein shell appears gray (#, outer circle, outlined in black for one NP in each panel) around each black NTA-AuNP (*, inner circle). The shell was noticeably larger in the case of the 50 nm AuNPs compared to the smaller AuNPs. Scale bars are 100 nm. Error bars reflect standard errors of the mean (SEM). Comparisons among sizes for a given enzyme were performed using a Student's *t* test with unequal variance (Excel), and all are significant at $p < 0.05$.

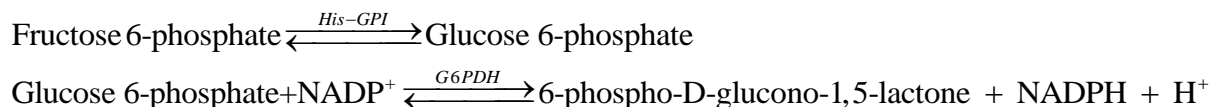
be spaced at the diameter of a multimer. To calculate the surface area of the first layer at the contact points, we used the radius of the NP plus the radius of the multimer (e.g. using a 5 nm NP and GPI, the radius for the surface area is 6.2 nm). This result was then multiplied by the number of NPs used to yield the total surface area of the first layer on all NPs. We divided the cross-sectional area of each multimer by the total surface area to yield the number of multimers that fit on the first layer. For each subsequent layer, the radius for surface area increases by the diameter of one multimer. To determine the number of layers for each enzyme and each size, we repeated this process until each model contained enough enzyme to match the measured amounts of protein bound to each NTA-AuNP. To validate this modeling, the relative number of layers per size NP was confirmed empirically using TEM as described above.

Because larger NPs had more multilayers, they would be numerically disadvantaged in terms of specific activity, k_{cat} and enzyme efficiency if their inner layers of multimers had restricted access to substrate. To investigate the impact on kinetic values of these enzymes in the underlying layers, we performed calculations using the assumption that only the “outer layer” of multimers were active. We defined “outer layer” to include all enzymes in the layer farthest away from the NP and the percentage of the second to last multimer layer which would not be covered by enzymes lying immediately atop them. For example, if only 60% of the top layer were occupied by multimers, then approximately 40% of the layer underneath would still have access to substrate.

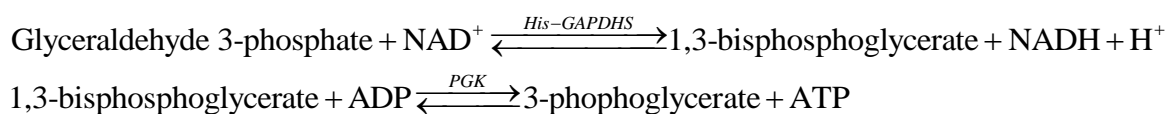
2.2.4: Enzyme Activity Assays. Reactions were carried out in clear 96-well plates and absorbance (340 nm) was detected with a spectrophotometer (Infinite 200 PRO Plate Reader, Tecan). His-tagged enzyme constructs were used in the first step of each respective reaction and exogenous enzymes, substrates and co-factors were added for quantification of activity. Kinetic assays used the following substrate concentrations: GPI, fructose 6-phosphate [0, 0.33, 0.67, 1.33, 2.67, 5.33, 10.67 mM]; GAPDHS,

glyceraldehyde 3-phosphate [0, 0.3, 0.6, 1.25, 2.5, 5, 10 mM]; PK, phosphoenolpyruvate [0, 0.17, 0.33, 0.83, 1.67, 3, 6]. k_{cat} was calculated by dividing V_{max} by the concentration of enzyme bound ($V_{max}/[E]$). K_M was the substrate concentration at half V_{max} .

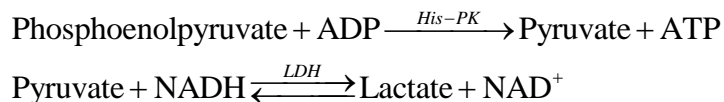
GPI was detected using the following reactions:



GAPDHS was detected using the following reactions:



PK was detected using the following reactions:



2.3 Results and Discussion

2.3.1: Oriented Enzyme Immobilization to Varying Sizes of Gold Nanoparticles.

We chose three mammalian glycolytic enzymes, each representing a different enzyme class, and genetically engineered them to include an N-terminal His-tag (Fig. 2.6). GPI isomerizes glucose-6-phosphate into fructose-6-phosphate. GAPDHS converts glyceraldehyde 3-phosphate to D-glycerate 1,3-bisphosphate through a coupled phosphorylation/oxidation reaction with NAD^+ . PK catalyzes the conversion of phosphoenolpyruvate to pyruvate through phosphorylation of ADP into ATP. All three enzymes were reverse transcribed from mouse testis RNA. A germ cell-specific, proline-rich domain of GAPDHS¹⁴ was replaced with the His-tag. Enzymes were expressed, purified and first tested for activity when free in solution prior to immobilization on AuNPs (data not shown).

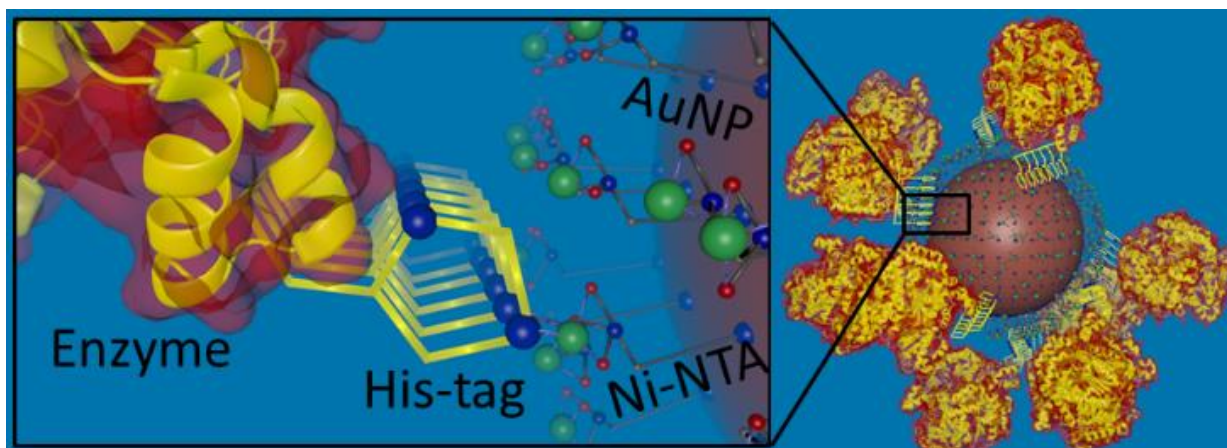


Figure 2.6: Site-specific, oriented immobilization for the binding of enzymes to AuNPs. This schematic representation shows a genetically engineered enzyme with an N-terminal his-tag bound to Ni-NTA groups on a AuNP surface. The genetically-encoded binding tag is positioned to replace a putative germ cell-specific binding domain (where applicable) with the goal being to minimize impact on substrate binding, needed conformational changes, and steric hindrance.

AuNPs have many attractive properties which make them ideal as a binding support including high dispersability, biocompatibility, and high stability at small scales. We modified AuNPs (\varnothing 5, 10, 20 and 50 nm; Sigma) with Ni-NTA (NTA-AuNP), and verified size using SEM (Fig. 2.1). We measured the zeta potentials of each size before and after modification, finding lower AuNP aggregation⁷⁷⁻⁷⁹ after modification (Zetasizer Nano ZS, Malvern; Fig. 2.2). We first evaluated a monolayer of enzyme tethered to each size of NTA-AuNP with less than 100% AuNP coverage. Absorbance values were used to calculate NTA-AuNP concentrations which were used in standardizing the NTA-AuNPs to equal surface area (Fig. 2.7). A sufficient amount of enzyme to create a monolayer was incubated with NTA-AuNPs of each size and then washed repeatedly. Amounts of enzyme bound and the percent of AuNPs covered (Fig. 2.8) were measured/calculated by performing BCA assays on each wash and subtracting the total unbound from the initial protein amount (Fig. 2.3).

2.3.2: Kinetics Trends for an Enzyme Monolayer.

After assessing binding, each conjugate preparation was utilized in side-by-side activity and kinetic assays. Kinetic measurements were obtained using coupled reactions linked to the reduction of NAD^+ to NADH (GAPDHS) or NADP^+ to NADPH (GPI), or the oxidation of NADH to NAD^+ (PK). Reactions were carried out in 96-well plates and absorbance read at 340 nm. Measurements for each enzyme at each AuNP size were carried out in triplicate. The second enzymatic step for each reaction was tested with NTA-AuNPs in suspension to rule out any change in signal due to the presence of NPs, as well as verifying that these enzymes were not limiting the reaction rate (Fig. 2.9). The three kinetic variables we evaluated were k_{cat} , K_M , and k_{cat}/K_M (Fig. 2.10). We also evaluated activity per NP (Fig. 2.11), finding that larger NPs, covered with more enzymes, had higher activities.

The turnover number (k_{cat}) is the maximum number of substrate molecules converted to product per enzyme molecule per second. As expected, each enzyme had varying inherent turnover numbers for

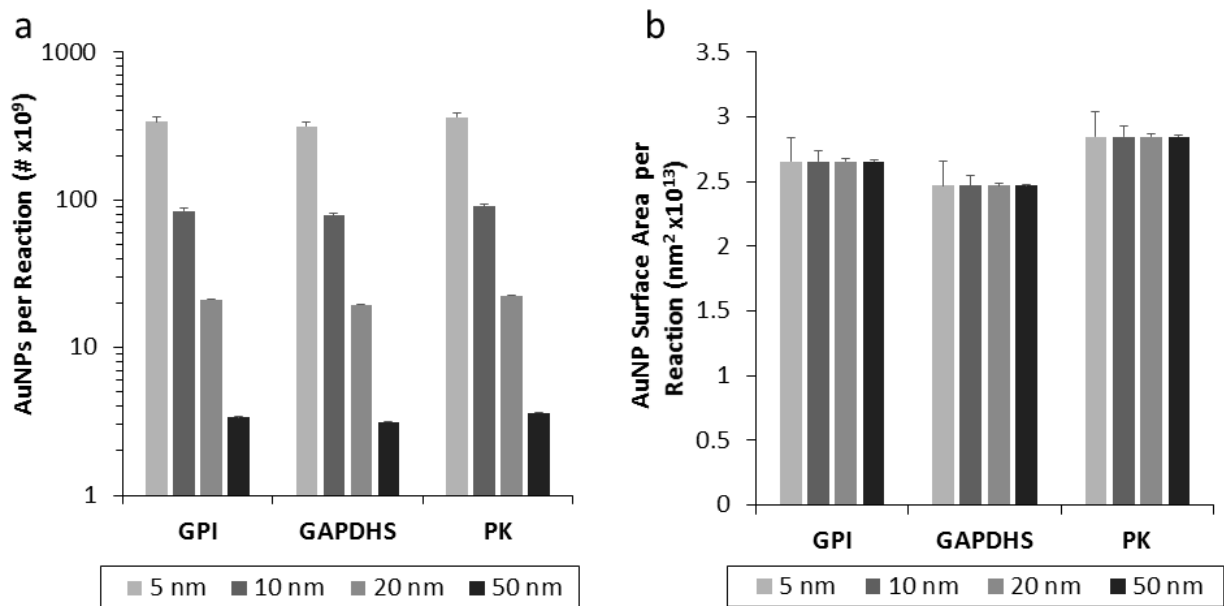


Figure 2.7: Amount of AuNP and surface area used in monolayer enzyme binding. (a) Absorbance values were used to determine AuNP concentration, which was then used to yield the number of AuNPs for enzyme binding. (b) This number was then used to calculate the total surface area for each size of AuNP. Error bars show standard deviation. All comparisons were performed using a Student's *t* test with unequal variance (Excel), and are significantly different at $p < 0.05$ between each AuNP size in **a**, and no significance in **b**.

Calculations:

The number of gold nanoparticles (NP) used per reaction (Rxn) [NP/Rxn] was taken from the calculated NP stock concentrations [NP/ml]. The amount of surface area (SA) per Rxn [SA/Rxn] was calculated by multiplying the SA of a single NP by the NP/Rxn.

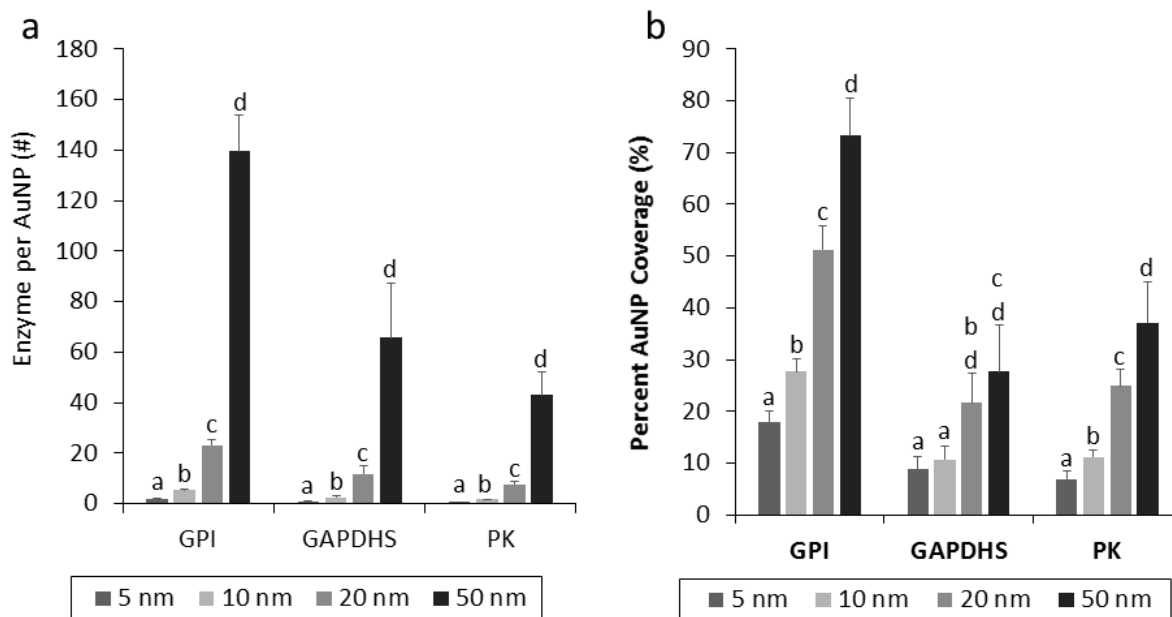


Figure 2.8: Enzyme coverage for each AuNP in monolayer approach. Surface area calculations were used for each size of AuNP together with the amount of bound enzyme to yield (a) how many enzymes were bound to each AuNP and (b) what percentage of the AuNP was covered by enzyme. Comparisons among sizes for a given enzyme were performed using a Student's *t* test with unequal variance (Excel); dissimilar letters denotes significance at $p < 0.05$.

Calculations:

The number of enzyme molecules per ng (#/ng) is simply calculated from the enzyme's molecular weight. The calculated amount of enzyme bound (ng) from BCA was then multiplied by the #/ng yielding the total number of enzyme molecules bound. The total number of enzyme molecules bound are then divided by the total number of NPs used in binding (NP/Rxn multiplied by the reaction volume) yielding the number of enzyme molecules per NP (E/NP). Next we utilized the spherical approximations for each multimer discussed in the calculations for enzyme layers, which gives the radius (E_r) and cross-sectional area (E_A) of each multimer. First we calculated the number of enzymes needed to make a monolayer on

each NP. The SA of a single layer (Layer_{SA}) of enzyme is $4\pi(NP_r + E_r)^2$. The number of enzymes which fit on that layer is Layer_{SA}/E_A . Finally the percent coverage is $(E/NP)/(\text{Layer}_{SA}/E_A)(100)$.

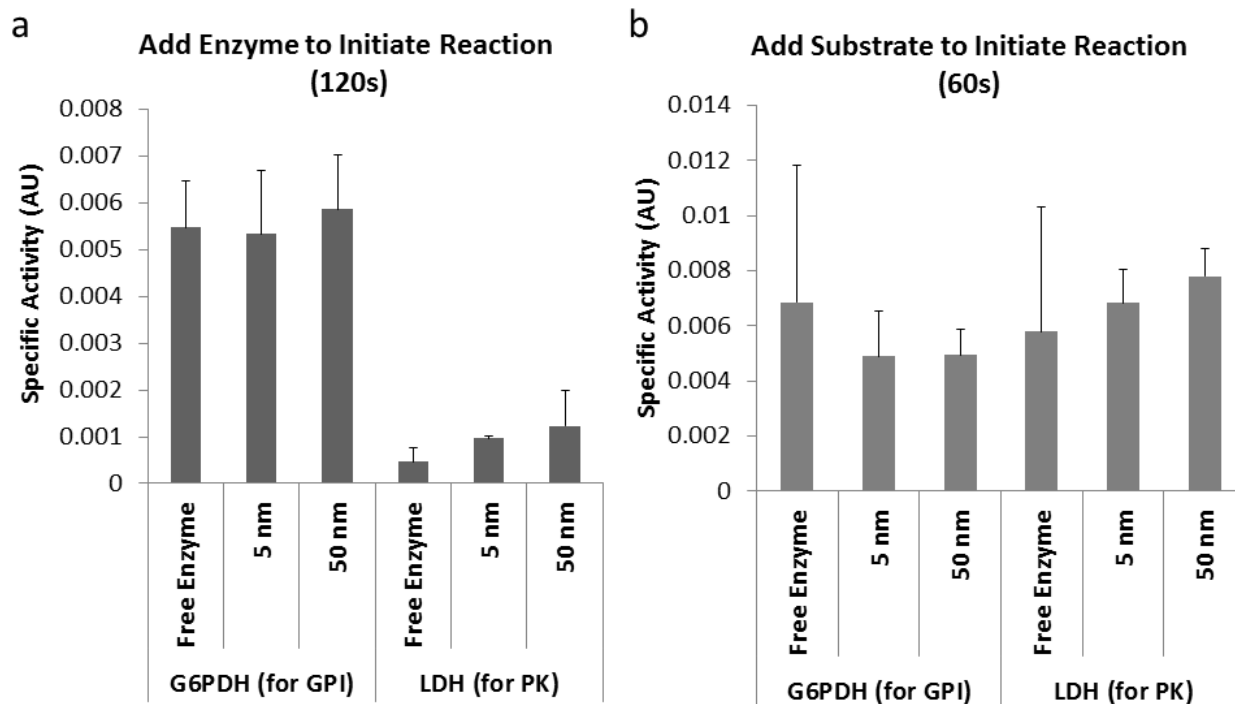


Figure 2.9: Specific activities and substrate utilization of exogenous enzymes in coupled reactions with and without AuNPs. To demonstrate that the activities measured via coupled reactions for GPI and PK reflected that of the tethered enzymes and not of exogenous enzymes in the coupled reactions, the specific activities of G6PDH for the GPI assay and LDH for the PK assay were measured with (5 and 50 nm) and without AuNPs. **(a)** The reaction was initiated by adding the enzyme or **(b)** by adding the substrate. The reaction was completed within the time shown, demonstrating how quickly these enzymes converted all their substrate to product. In comparison, the two-step reactions with tethered GPI and PK took more than 120 min to use an equivalent amount of substrate, demonstrating that the secondary enzymes were not limiting the reaction rates. Presence of AuNPs did not cause any significant changes in reaction rates. Error bars show SEM.

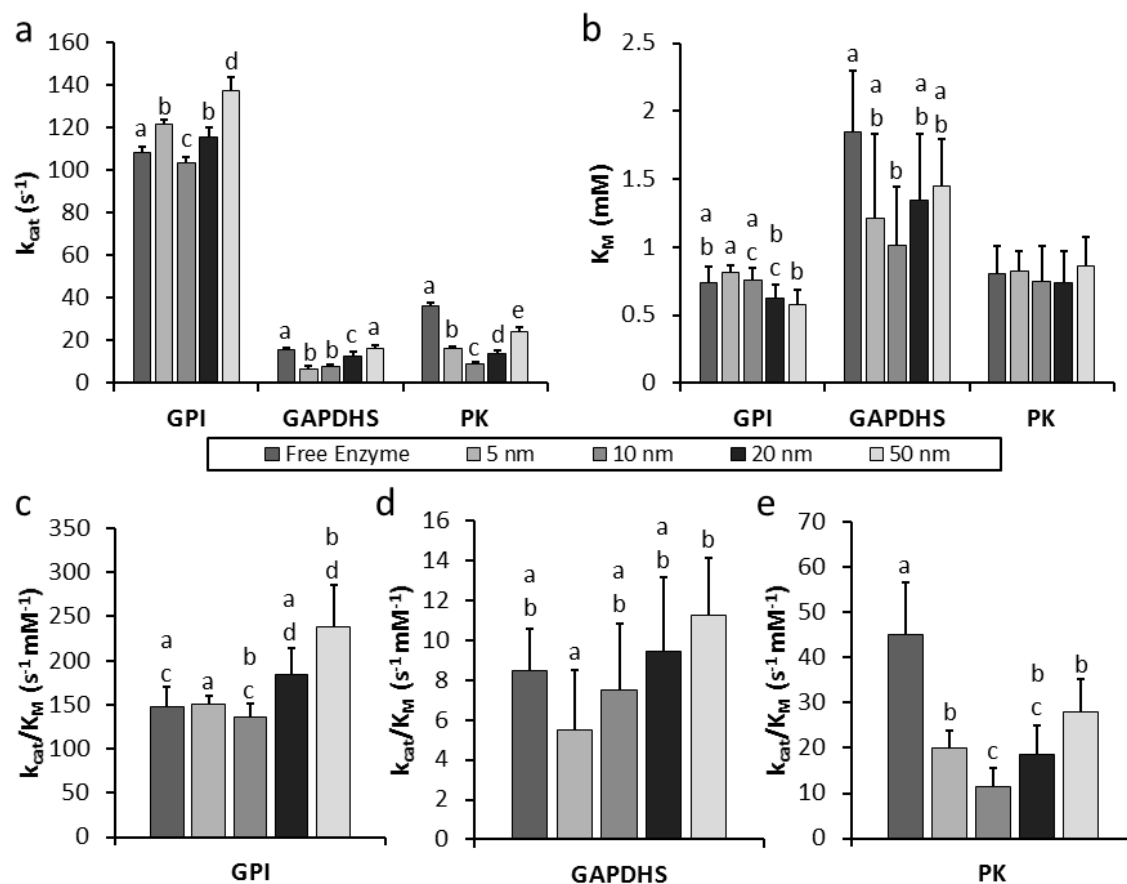


Figure 2.10: Kinetics of the tethered enzymes in a monolayer. Activity was measured for each enzyme on various sizes of AuNP with varying amount of substrate. Values for k_{cat} and K_M were calculated using Michaelis-Menten kinetics. **(a)** The turnover number (k_{cat}) displayed no significant trend, irrespective of enzyme type. **(b)** K_M also showed no significant difference for any enzyme as the size of AuNP changed. **(c-e)** Both kinetic variables were then utilized to plot enzyme efficiency (k_{cat}/K_M) yielding no clear trend for change in efficiency as AuNP size increased. Error bars show standard deviation. All comparisons among sizes for a given enzyme were performed using a Student's t test with unequal variance (Excel); dissimilar letters denotes significance at $p < 0.05$, no letters indicate no significance.

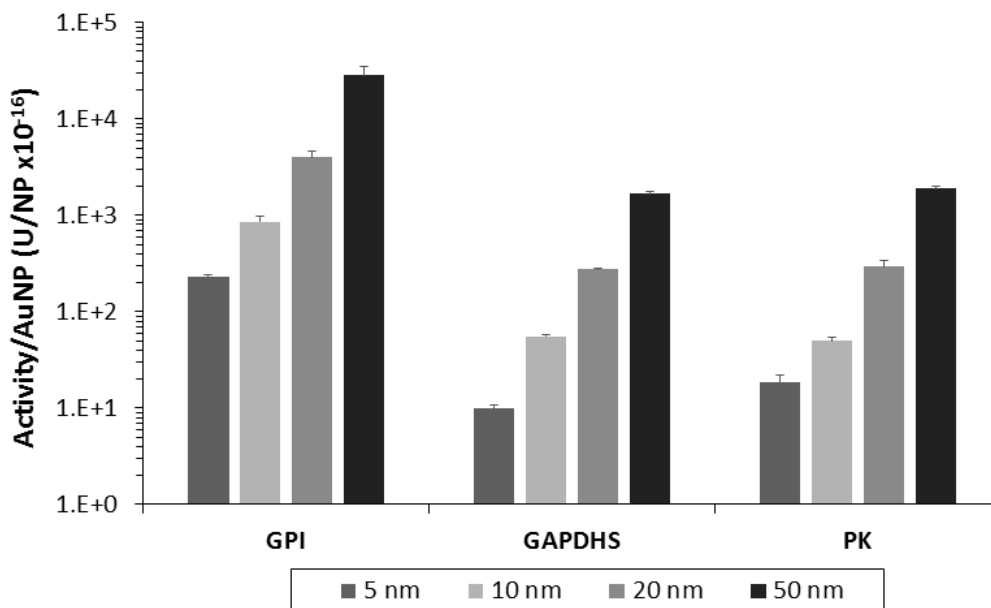


Figure 2.11: Total activity of monolayer tethered enzymes per NTA-AuNP. Enzymatic activity was measured for each size of every AuNP conjugate and divided by the total number of AuNPs to give information about the activity per AuNP, which logarithmically increased as AuNP size increased. Error bars reflect standard deviation. All comparisons among sizes for a given enzyme were performed using a Student's *t* test with unequal variance (Excel), and all are significantly different at $p < 0.05$.

the free enzymes (not tethered), ranging from GPI at 108.5 s^{-1} to GAPDHS at 15.7 s^{-1} . Although statistically significant differences in k_{cat} were noted in individual comparisons among sizes for all three enzymes when tethered as monolayers (Fig. 2.10), we are cautious about over-interpreting these differences due to the fact that the NPs were standardized according to surface area; this resulted in increased numbers of larger NPs being used, making them slightly more susceptible to loss during washing. Given this situation, the subtle differences we noted were not that dissimilar to observations from previous studies showing no clear changes in k_{cat} ^{21, 74}.

K_M inversely relates to substrate affinity. For all three enzymes, immobilization did not confer any significant, generalizable changes in K_M . Previous studies using non-specific adsorption¹⁴ and random amine binding techniques¹³ suggested that K_M varied with NP size. This discrepancy is likely because our use of oriented immobilization reduced the likelihood of blocking the substrate binding domain. Our findings suggest that prior results were dependent upon attachment chemistry, and not an inherent impact of NP size on tethered enzyme activity.

Lastly, we looked at k_{cat}/K_M , reflecting the efficiency with which an enzyme converts a substrate to product. All three enzymes showed slight yet statistically significant differences in k_{cat}/K_M with differing NP sizes, largely reflecting the variation in k_{cat} . However, no clear trends were observed. Notably, the fact that there were only subtle changes in any of the three kinetic variables when enzymes were tethered to different sizes of NPs in a monolayer, emphasizes the advantages of a tethering strategy based on oriented immobilization.

2.3.3: Effects Multilayers Have on Enzyme Kinetics.

Next, we investigated the impact of NP size under conditions of maximum enzyme loading which yields maximum activity per AuNP. To test maximal enzyme binding and multilayer formation per NP, an excess of each enzyme was incubated with NTA-AuNPs of each size (Fig. 12) and then washed

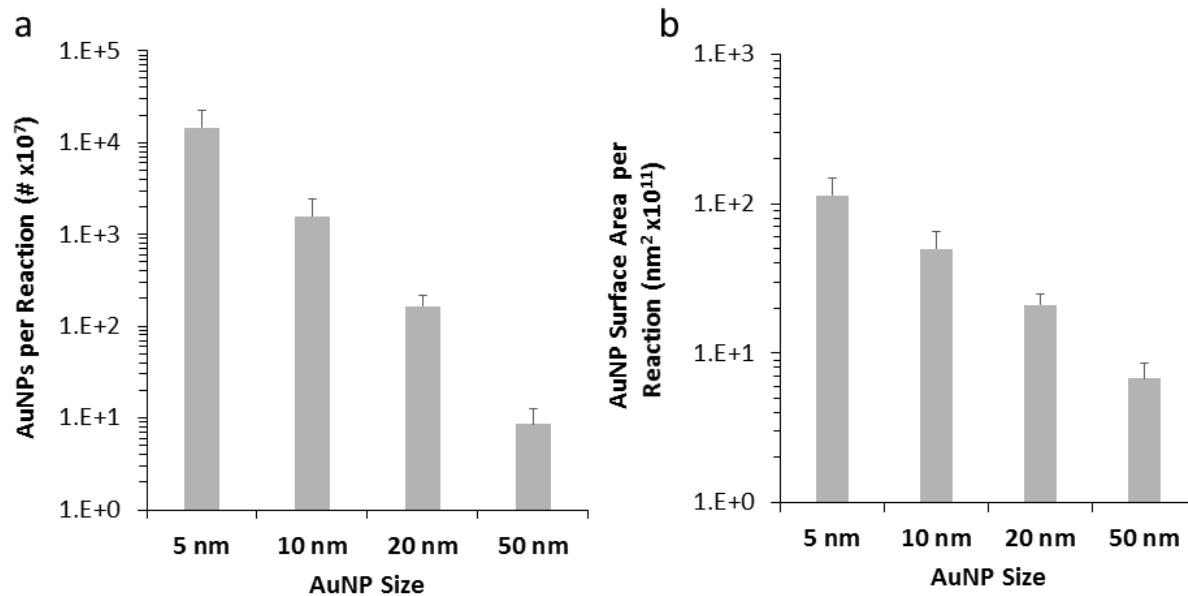


Figure 2.12: Amount of AuNP and surface area used in multilayer enzyme binding. (a) Absorbance values were used to determine AuNP concentration, which was then used to yield the number of AuNPs used for enzyme binding. (b) This number was then used to calculate the total surface area for each size of AuNP. Error bars show standard deviation. All comparisons were performed using a Student's *t* test with unequal variance (Excel), and all are significantly different at $p < 0.05$ between each AuNP size.

repeatedly. Amounts of enzyme bound (Fig. 2.5 a) were measured with BCA assays (Fig 2.4). Surface area calculations (using spherical approximations for the functional multimers) and measured amounts of enzyme bound were used to calculate multilayer formations (Fig. 2.5 b). These calculations were corroborated empirically using TEM on NTA-AuNPs with tethered GPI (Fig. 2.5 c-g). Our results showed that enzyme multilayers increased as NP size increased.

The multilayer conjugates displayed significant trends in specific activity and the kinetic variables. Activity per NP increased with increasing NP size when compared to monolayer results and as expected, the larger AuNPs with more multilayers displayed higher activity than those on the small AuNPs (Fig. 2.13). Final kinetics and Pearson correlation factors (CF) to show trends with increasing NP size are shown in Table 2.2 and Figure 2.14, respectively. When tethered, each enzyme showed a significant, decreasing trend in k_{cat} with increasing AuNP size, with an average CF of 0.9. One possible explanation is that the increased number of multilayers on the larger NPs decreased the effective amount of active enzyme on the larger particles; this is modeled and discussed below. A comparison with the monolayer data supports this hypothesis.

Much like the monolayer data, K_M showed no significant trends in multilayer data. Again, this is most likely due to our tethering strategy which might orient enzyme complexes even in layers at a distance from the surface of the NP due to the positively charged his-tag. All three enzymes showed a decrease in enzyme efficiency as AuNP size increased (CF: 0.96 for GPI; 0.88 for GAPDHS; 0.86 for PK), primarily due to the changes in k_{cat} . Importantly, it is worth noting that retention of enzyme specific activity ranged from 73-94% when comparing the enzymes with maximum efficiency (tethered to the 5 nm AuNP) with untethered counterparts (Fig. 2.15). This very high activity highlights the efficacy of our biomimetic tethering strategy by helping prevent the enzymes from coming into direct contact with the surface. However, as discussed below, decreases in specific activity for larger sizes of NP were likely affected by enzyme multilayers.

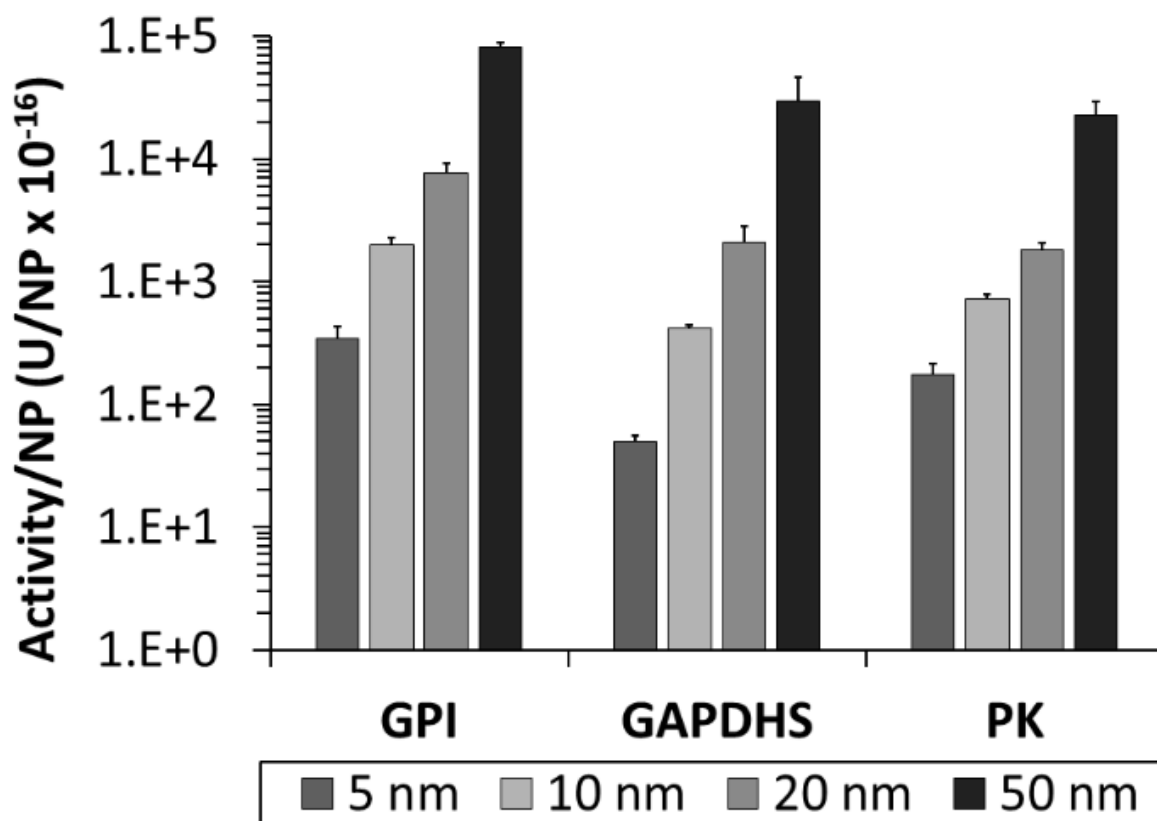


Figure 2.13: Total activity of multilayer tethered enzymes per NTA-AuNP. Enzymatic activity was measured for each size of functionalized AuNP and divided by the total number of AuNPs to give information about the activity per AuNP, which logarithmically increased as AuNP size increased. Error bars reflect standard deviation. All comparisons among sizes for a given enzyme were performed using a Student's *t* test with unequal variance (Excel), and are all significant at $p < 0.05$.

Table 2.2: Effect of AuNP size on multilayer tethered enzyme kinetics.

| | AuNP Size | Free Enzyme | 5 nm | 10 nm | 20 nm | 50 nm |
|--|-----------|--------------|--------------|--------------|-------------|-------------|
| k_{cat} (s^{-1}) | GPI | 108.5 ± 3.26 | 62.1 ± 1.67 | 80.7 ± 1.39 | 33.5 ± 0.40 | 20.2 ± 0.54 |
| | GAPDHS | 15.7 ± 0.55 | 11.4 ± 0.48 | 10.7 ± 0.48 | 6.3 ± 0.37 | 4.9 ± 0.12 |
| | PK | 36.1 ± 3.00 | 23.1 ± 1.88 | 15.1 ± 1.22 | 5.0 ± 0.55 | 3.3 ± 0.41 |
| K_M (mM) | GPI | 1.61 ± 0.15 | 1.07 ± 0.10 | 1.44 ± 0.08 | 0.95 ± 0.04 | 1.03 ± 0.10 |
| | GAPDHS | 2.68 ± 0.24 | 2.72 ± 0.29 | 2.83 ± 0.31 | 2.90 ± 0.42 | 3.24 ± 0.19 |
| | PK | 0.71 ± 0.14 | 0.51 ± 0.16 | 0.47 ± 0.15 | 0.67 ± 0.22 | 0.60 ± 0.24 |
| k_{cat}/K_M ($\text{s}^{-1} \text{mM}^{-1}$) | GPI | 67.4 ± 6.45 | 58.1 ± 5.55 | 56 ± 3.17 | 35.2 ± 1.54 | 19.6 ± 1.89 |
| | GAPDHS | 5.8 ± 0.56 | 4.2 ± 0.48 | 3.8 ± 0.45 | 2.2 ± 0.34 | 1.5 ± 0.10 |
| | PK | 50.9 ± 14.85 | 45.4 ± 14.13 | 32.1 ± 10.81 | 7.5 ± 2.60 | 5.5 ± 2.31 |

Each measurement was carried out in triplicate from at least two separate preparations of each protein.

Data were analyzed using GraphPad Prism 6 Software. Errors show standard deviation.

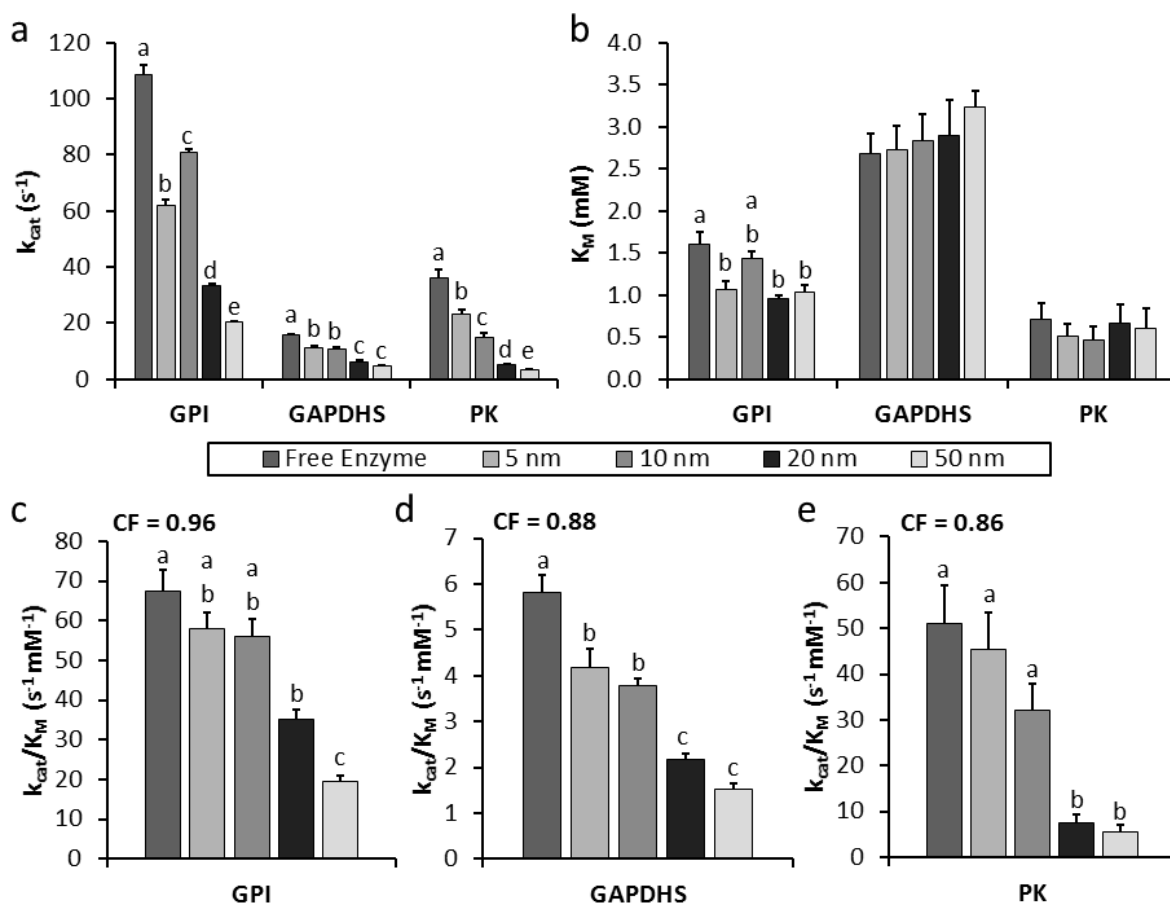


Figure 2.14: Graphical representation of the kinetics of the multilayer tethered enzymes. Activity was measured for each enzyme on various sizes of AuNP with varying amount of substrate. Values for k_{cat} and K_M were calculated using Michaelis-Menten kinetics. **(a)** The turnover number (k_{cat}) decreased as AuNP size increased, irrespective of enzyme type. **(b)** However, K_M showed no significant difference for any enzyme as the size of AuNP changed. **(c-e)** Both kinetic variables were then utilized to plot enzyme efficiency (k_{cat}/K_M) yielding a substantial decrease in efficiency as AuNP size increased with correlation factors as high as 0.96 for GPI. Error bars show standard deviation. All comparisons among sizes for a given enzyme were performed using a Student's t test with unequal variance (Excel); dissimilar letters denotes significance at $p < 0.05$, no letters indicate no significance. Pearson's correlation factors (CF) were calculated using Excel.

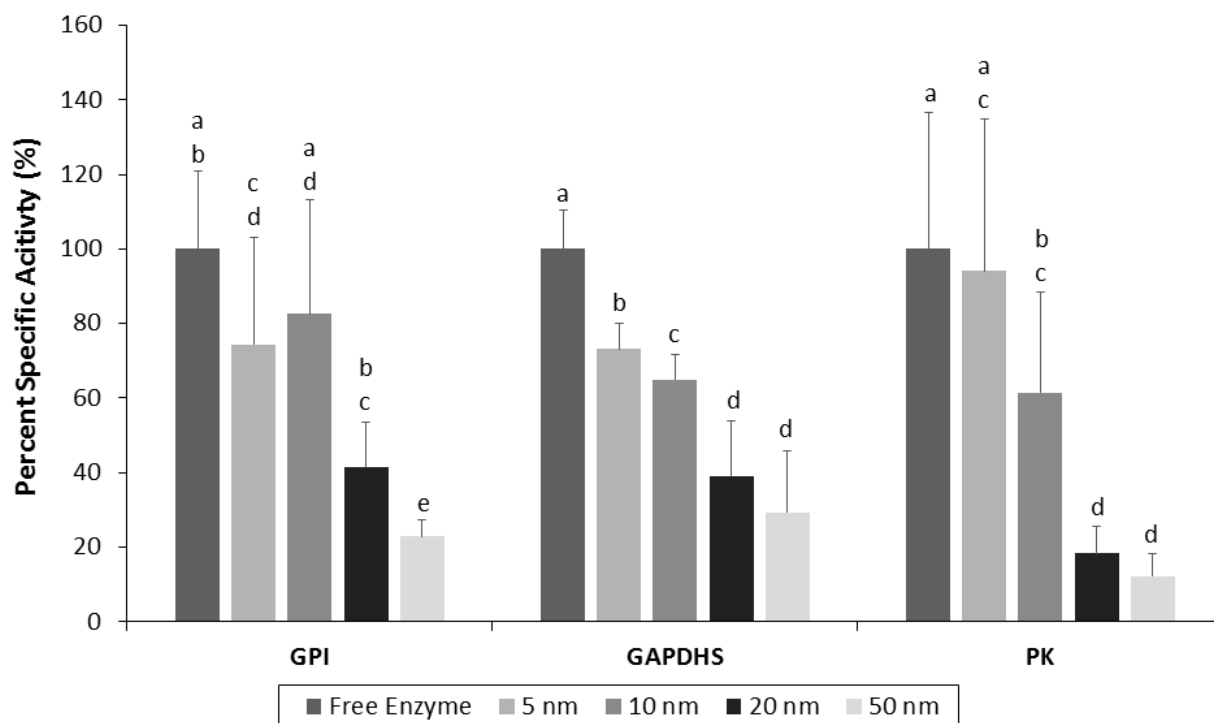


Figure 2.15: Comparison of multilayer specific activity of tethered enzymes versus the corresponding free enzyme in solution. Specific activity was measured using substrate concentration at $1/2 V_{max}$ for each enzyme. The specific activity of each tethered enzyme for each size NTA-AuNP was divided by that of the untethered enzyme yielding percentage of specific activity of the free enzyme. The data showed a clear trend that enzyme activity on smaller NTA-AuNPs was retained far better than on the larger AuNPs, with as high as 94% retention in activity (PK on 5 nm AuNPs). This likely reflects a combination of factors including the presence of enzymes positioned in inner layers on the larger NPs where they might have less access to substrate. Error bars show standard deviation. Comparisons among sizes for a given enzyme were performed using a Student's *t* test with unequal variance (Excel); dissimilar letters denotes significance at $p < 0.05$.

From what we have shown here, the leading contributor to changes in enzyme kinetics is from multilayer enzyme effects. As NP size increases the number of enzyme multilayers increase. The reasoning behind why multilayers form on larger NPs is not entirely known, however we hypothesize that there are multiple contributing factors. As the curvature of the particle decreases the distance between enzymes also decrease, this allows for closer packing on the surface and limited enzyme mobility, thus an enzyme can bind with the packed enzyme surface creating multilayers more readily than a single mobile enzyme on a highly curved surface. The packing of enzyme multilayers is likely controlled by weak protein-protein electrostatic forces. Due to our oriented immobilization strategy, there exists a highly positive his-tag present on the enzyme which will be attracted to the negatively charged residues on lower enzyme layers, therefore orientation is preserved throughout the multilayers. The second possibility for enzyme multilayers are due to enzyme crowding^{80, 81}, at high enzyme concentrations it has been shown that enzymes prefer to form protein complexes with each other in order to minimize negative space. The enzyme crowding also stabilizes the enzymes by forcing them to remain in their folded state, which is more compact in crowded conditions, rather than their denatured state. While enzyme crowding and retention of enzyme orientation enhances enzyme activity, there are negative effects from multilayers which have higher impact within those layers. Steric hindrance between enzymes together with enzyme crowding equates to enzymes preferring a tightly folded confirmation, impeding needed conformational changes in lower enzyme layers. Also, the lower enzyme layers are not accessible to substrate, and any substrate which does penetrate through the layers is at high competition with adjacent enzymes. If we look at just the outermost layer of enzymes the negative effects are partially removed from the equation.

We investigated potential effects of multilayers on our kinetic parameters by calculating the number of enzymes in the outermost layer and assuming those were the only active enzymes (Fig. 2.16). This assumption likely resulted in an underestimation of active enzymes because we deliberately did not take

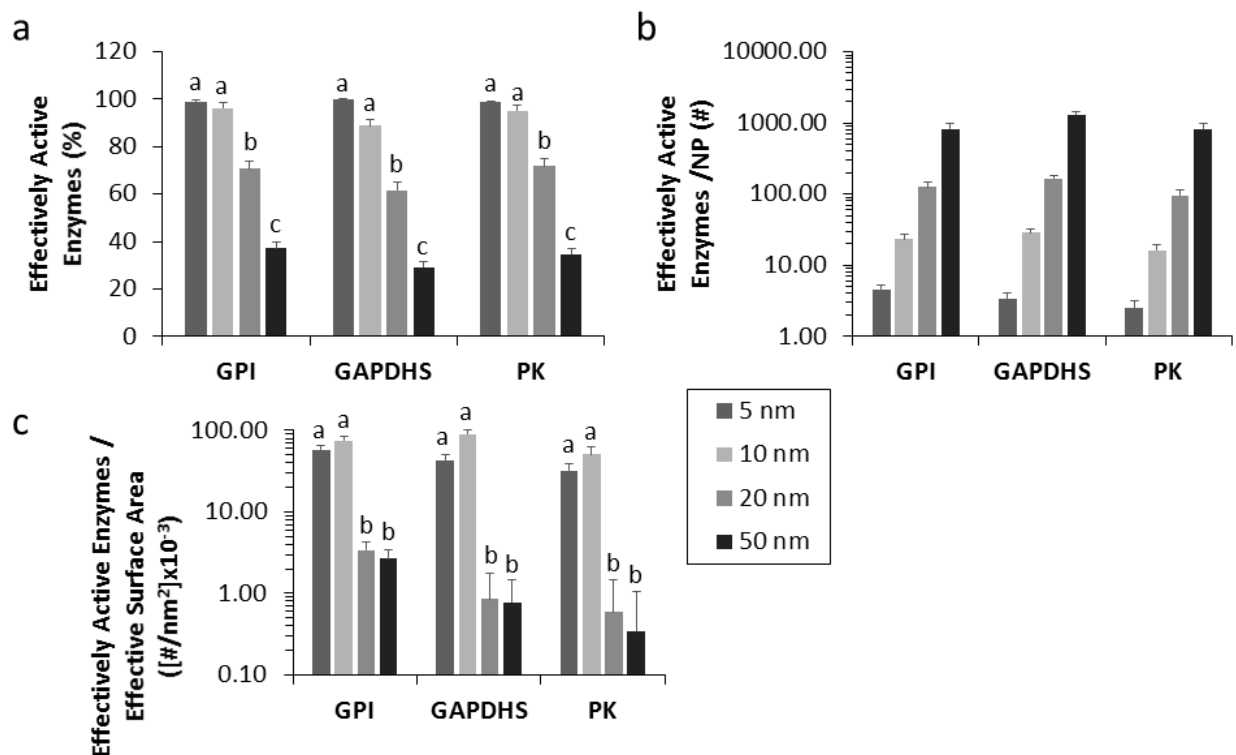


Figure 2.16: Modeled comparisons of the percentage and number of enzymes in the outermost layer around each AuNP using multilayer approach. To begin to probe whether the reduction in specific activity on larger NPs resulted from the presence of many enzymes trapped in inner layers where they might not have access to substrate, we calculated how many enzymes would be found in the outer layer for each different size NP and for each enzyme. Note that by “outer layer,” we include both the layer that is physically farthest from the NP and that percentage of enzymes in the layer immediately beneath it that are not covered physically, and hence would have free access to substrate. **(a)** First, we modeled the percentage of enzymes per NTA-AuNP that would be on the outer layer compared to the total enzymes. **(b)** Although the percentage in the outer layer was reduced for larger NPs, their much greater size still led to an increased number of enzymes in that outer layer. **(c)** Lastly, one can compare the number of outermost enzymes per effective surface area; for the larger NPs this is the surface area of the layer of enzymes beneath the outermost layer. For smaller NPs where there was only one layer of enzymes, the surface area of the NP was used. Error bars show standard deviation. Comparisons among

sizes for a given enzyme were performed using a Student's *t* test with unequal variance (Excel). All comparisons among sizes for a given enzyme in **b** are significant at $p < 0.05$. Dissimilar letters denotes significance at $p < 0.05$.

into account the activity of inner layers or how layers interact functionally. Middle layers may induce steric hindrance, be bound in non-oriented fashion, or conversely, may enhance activity by creating enzyme complexes. Differences in kinetic values with different NP sizes were not as prominent when only the outermost layer was presumed active; however, k_{cat} and k_{cat}/K_M decreased slightly for PK as NP size increased (Fig. 2.17). The concordance of the results of this modeling with our measured results in Figure 2.10, even under the strict assumption that only the outermost layer might be active, suggests that the site-specific, oriented immobilization of the enzymes attaching to the NP conferred some beneficial impact that extended through the multilayers. This is consistent with our prior findings showing advantage of this approach in terms of specific activity over random adsorption or carboxyl-amine binding^{18, 19}.

2.4 Conclusions

In summary, we used genetically-encoded tags to provide site-specific immobilization of enzyme from three different classes on four sizes of NTA-AuNPs. As NP size increased, the amount of enzyme multilayers increased, as did enzymatic activity per NP. Monolayer data demonstrated the effectiveness of our tethering strategy, exhibiting negligible influence on the kinetics of the enzymes when attached to different sizes of AuNPs. Enzymatic activity (k_{cat} and k_{cat}/K_M) from multilayer data displayed negative trends as AuNP size increased, independent of enzyme class, whereas there was no change in K_M . Our data address the fundamental question of how NP size affects the kinetics and multilayer formation of varying enzyme classes in both monolayers as well as at maximal enzyme loading. Regardless of enzyme class, the larger particles showed higher total activity per NP, whereas smaller particles showed higher activity per enzyme molecule. These generalizable trends will be of value when designing diverse applications that utilize NPs functionalized with tethered enzymes.

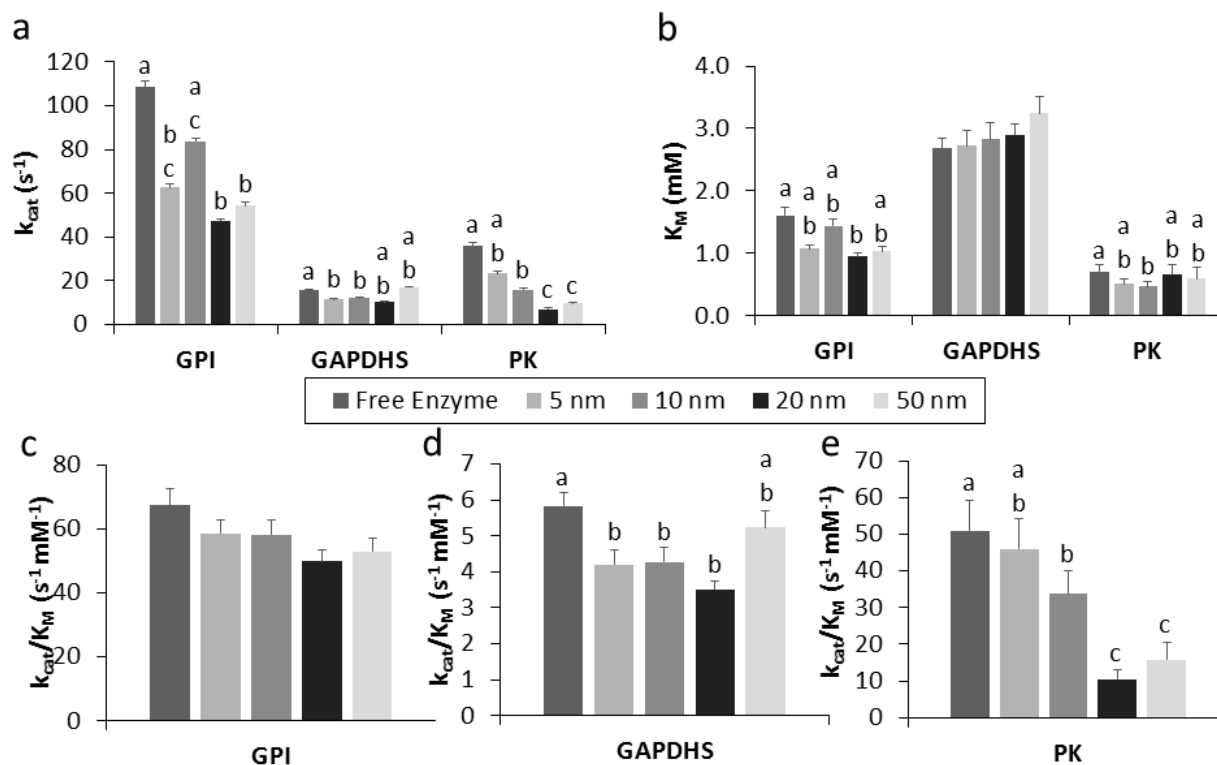


Figure 2.17: Comparison of the multilayer kinetics with respect to the outermost layer of tethered enzymes. Based on the modeled numbers of enzymes in the outermost layers, and assuming that only these enzymes were active, we see surprisingly small change versus the results shown earlier in Figure 2.10. **(a)** The turnover number (k_{cat}) declines less sharply due to the decrease of effectively active enzymes for larger sizes of AuNPs, and is flat for the least active enzyme, GAPDHS. **(b)** The K_M is not influenced by the amount of effective enzymes and so does not change. **(c-e)** Consistent with the change in k_{cat} , enzyme efficiency (k_{cat}/K_M) also showed a less marked decrease in efficiency with increasing AuNP size. Error bars show standard deviation. Comparisons among sizes for a given enzyme were performed using a Student's t test with unequal variance (Excel); dissimilar letters denotes significance at $p < 0.05$, no letters indicate no significance.

CHAPTER 3

USE OF TETHERED ENZYMES FOR RAPID BIOMARKER DETECTION – A PLATFORM TECHNOLOGY ENABLING POINT OF CARE DIAGNOSIS OF BRAIN PATHOLOGIES[‡]

3.1 Introduction

There is pressing need for quick and objective diagnostic technologies for both time sensitive and difficult to diagnose pathologies. Much attention has therefore focused on the identification of disease-specific peripheral biomarkers, and use of new technologies to improve antibody-based detection capabilities. This interest is well justified because of the enormous medical, social and economic impacts of these diseases. Stroke is one of the best examples of a brain disease that is both hard to diagnose and time sensitive, annually affecting over 15 million people. Of these, 5 million die and an additional 5 million are left permanently disabled⁸². Currently, its diagnosis relies on neurologists to distinguish stroke from mimics using advanced imaging tests (e.g. CT, MRI) in order to determine whether the stroke is ischemic or hemorrhagic. If appropriate, thrombolytic treatment can then be initiated, but is most effective only within a short 3-4 hour window from onset⁸³. In addition to rapid diagnosis of stroke, there is growing military and civilian need for PoCT devices that provide objective, biomarker-based, diagnostic and prognostic information regarding traumatic brain injuries (TBI/concussion), and neurodegenerative disease [e.g. Alzheimer's disease (AD), Parkinson's Disease (PD)]. For these BP, an objective PoCT could lead to interventions beginning early upon the onset of disease as well as provide a platform to monitor disease progression or response to therapy.

Traditional technologies for blood biomarker diagnostics include ELISA, PCR, and mass spectrometry (MS). However, these technologies are limited to laboratory use because they require sample

[‡] Modified from Cohen R, Lata JP et. al. Manuscript submitted for publication. The engineering of the enzymes and their comparative activities tethered vs non-tethered were completed by Cohen, R. Assays established, performed and analyzed for NSE detection in rat stroke models and human patient samples were completed by Lata, JP and Cohen, R with equal contributions.

preparation, and use of sophisticated instruments and highly trained technicians. Moreover, they are time and labor intensive, and are expensive⁸⁴. Much of the research on detection of blood biomarkers has focused on antibody-based methods. Although there has been considerable progress in the field, such as the introduction of lateral flow based assays, constraints due to the speed of antibody-antigen interactions, low sensitivity, semi-quantitative results and the complexity of associated detection instrumentation have thus far prevented such antibody capture methods from becoming the basis for a field-capable PoCT device to detect BP⁸⁴.

Over the last few decades, a large number of molecules have been studied for their potential usefulness as blood-borne BP biomarkers. Although no single biomarker will likely provide a definitive diagnosis of any BP, the glycolytic enzyme, NSE, is released from damaged neurons and has been suggested to be valuable for the diagnosis of various BPs^{85 86 87}. Evidence also supports its usefulness as a prognostic indicator in predicting neurological outcomes of post-cardiac arrest⁸⁸ and mild TBI⁸⁹. NSE has been suggested to be useful in distinguishing stroke from mimics, an important first step in expediting the diagnostic process⁸⁵. In addition, it has been suggested that changes in serum NSE levels may indicate changes in brain morphology in AD⁹⁰. Overall, changes in plasma NSE levels are of clinical significance to several of the major BPs, making it an excellent first candidate to test a new diagnostic platform technology.

As an alternative to antibody capture, fluid phase enzymatic reactions have been used to detect plasma NSE by means of its enzymatic activity^{91 92}; however, these failed to develop into a PoCT technology. Semi-solid phase bioluminescence detection of NSE through its binding to immunobeads enabled high sensitivity detection⁹³. However, this method required long serum-bead incubation times and did not tether the downstream enzymes (i.e. PK and Luc). Tethering enzymes has several advantages for a PoCT, such as concentrating the detection reaction, spatially localizing the readout, and potentially improving shelf life. The principle obstacle lies in maintaining enzymatic function when

immobilizing enzymes. Immobilization often interferes with substrate binding sites and/or needed conformational changes⁹⁴.

To overcome this obstacle, we adopted a strategy of biomimicry, inspired by the tethering of glycolytic enzymes to a cytoskeletal scaffold in the sperm flagellum, where they provide localized energy production^{15 95}. We previously showed that oriented immobilization via genetically-encoded binding domains conferred advantages in specific activity versus either random adsorption or chemically-specific binding^{18, 19}. Here, we extend our previous studies^{19 18} in a novel direction, to generate a PoCT platform based on enzymes tethered to nanoparticles via biomimetic oriented immobilization (Tethered Enzyme Technology, TET). Our approach couples production of ATP by PK with activity of firefly luciferase (Luc) to generate a highly rapid and sensitive bioluminescent readout for the detection of NSE. As a tethering scaffold for the PoCT device, we employed SiO₂ nanoparticles for their many positive attributes: high biocompatibility, low optical absorption, dispersibility, high surface area, and the ability to be integrated into various devices with spatial control. We hypothesized that oriented immobilization of PK and Luc on SiO₂ NPs could provide the basis for highly rapid, quantitative and sensitive detection of NSE through an enzymatic cascade reaction in a form suitable for use in a PoCT.

3.2 Materials and Methods

3.2.1: Experimental Design. The aim of this study was to explore the advantages of utilizing enzymes tethered via oriented immobilization in the detection of NSE, a neuronal injury biomarker, towards development of a PoCT technology for BP.

The study was designed to follow 3 successive stages: (i) Test the enzyme-based assay in vitro to examine the effects of oriented enzyme immobilization on the sensitivity and efficiency of the solid phase vs fluid phase reaction. (ii) Test the tethered enzyme assay in plasma from a rat BP model. Here, to simulate stroke, 2 groups of rats underwent craniectomy under anesthesia, and branches of the MCA

were cauterized in the test group. Peripheral blood samples were drawn over a time period of 6 hours to monitor changes in NSE level. Finally, the changes in NSE levels as measured with TET were compared to those obtained with ELISA. (iii) Use pre-filled 96 well plates in a comparative analysis of NSE plasma levels in samples taken from human subjects and measured by both the solid phase TET reaction and ELISA.

Enliten ATP detection kit was purchased from Promega (Madison, WI). 2-PG, PEP, ADP, ATP, luciferin, PK antibody, NSE, and yeast α -enolase were from Sigma (St. Louis, MO). pcDNA4/HisMax TOPO TA vector was from Invitrogen (Carlsbad, CA). Si-NPs (500 nm) were purchased from Spherotech Inc. (Lake Forest, IL).

3.2.2: Construction of His-Si4 fusion proteins. The complementary deoxyribonucleic acid (cDNA) of PK was obtained by reverse-transcription polymerase chain reaction (RT-PCR) from mouse muscle RNA. The Luc2 sequence was amplified from the Luciferase2 plasmid, Promega (Madison, WI).

His-PK and His-Luc were generated by TA cloning of PK and Luc into pcDNA4/HisMax TOPO TA. To generate the His-Si4 vector, two complementary oligonucleotides (Integrated DNA Technologies, Inc. USA) encoding the Si4 sequence⁹⁶ with overhanging A were hybridized and cloned into the TA site of the pcDNA4/HisMax TOPO TA plasmid, followed by restriction/ligation of PCR fragments of PK and Luc to make His-Si4-plasmids. Subsequently, the Si4-PK and Si4-Luc sequences were amplified by PCR and inserted into pcDNA3.1 to make Si4-PK and Si4-Luc. Constructs were validated by sequencing and amplified in TOP10 cells and then purified.

3.2.3: Protein expression and purification. HEK293-F-FreeStyle cells (Invitrogen, Grand Island, NY) were transfected with plasmids encoding His, His-Si4 or Si4 fusion proteins using the Freestyle MAX reagent (Invitrogen, Grand Island, NY) and incubated for 24-72 hrs in 8% CO₂. Cells were harvested and lysed by

sonication (Sonifier 250, Branson, Danbury, CT). His-tag or His-Si4 fusion proteins were purified on Ni/NTA beads as previously described ¹⁹, with the exception that the Si4 tag was used to immobilize PK on silica NPs directly from the cell lysate (Figure 3.1 D and E), providing a fast and simpler purification process.

3.2.4: Enzymatic activity assays. Enzyme activities for both single and coupled reactions were assessed via luminescence output, in sodium phosphate buffer (50mM) supplemented with MgCl₂ (5mM) and KCl (20mM). The forward reaction for PK is: $PEP+ADP \rightarrow pyruvate+ATP$. The forward reaction for Luc is: $ATP+luciferin +Mg^{2+} \rightarrow hv$. The PK and Luc coupled reaction is: $PEP+ADP \rightarrow pyruvate+ATP +luciferin \rightarrow hv$. All experiments were carried out in 96-well black or white plates at room temperature. To assay PK activity alone, purified or immobilized PK was mixed with Enliten luciferase/luciferin reagent in addition to ADP and PEP as indicated for individual experiments. To assay Luc alone, purified or immobilized Luc was mixed with luciferin, Mg²⁺, K⁺ and ATP as indicated in individual experiments and activity was monitored by means of light emission as detected by a luminometer (GloMax, Promega, Madison, WI), where the luminescence signal was integrated for 3 seconds every minute for up to 50 minutes, as indicated per each experiment. To assess the activity of the coupled reactions, PK and luciferase were mixed as indicated above, with luciferin, ADP and PEP, and light emission was measured by luminescence. Data processing and analysis were carried out using Excel (Microsoft) and Origin (Origin Lab, Northampton, MA). In experiments with internal repetitions, data are presented as average \pm standard deviation. Otherwise, representative experiments are shown that were repeated independently at least three times with similar results.

3.2.5: Detection of NSE in rat stroke model. All animal procedures were reviewed and approved by the Cornell University Institutional Care and Use Committee (protocol number 2009-0043) and were

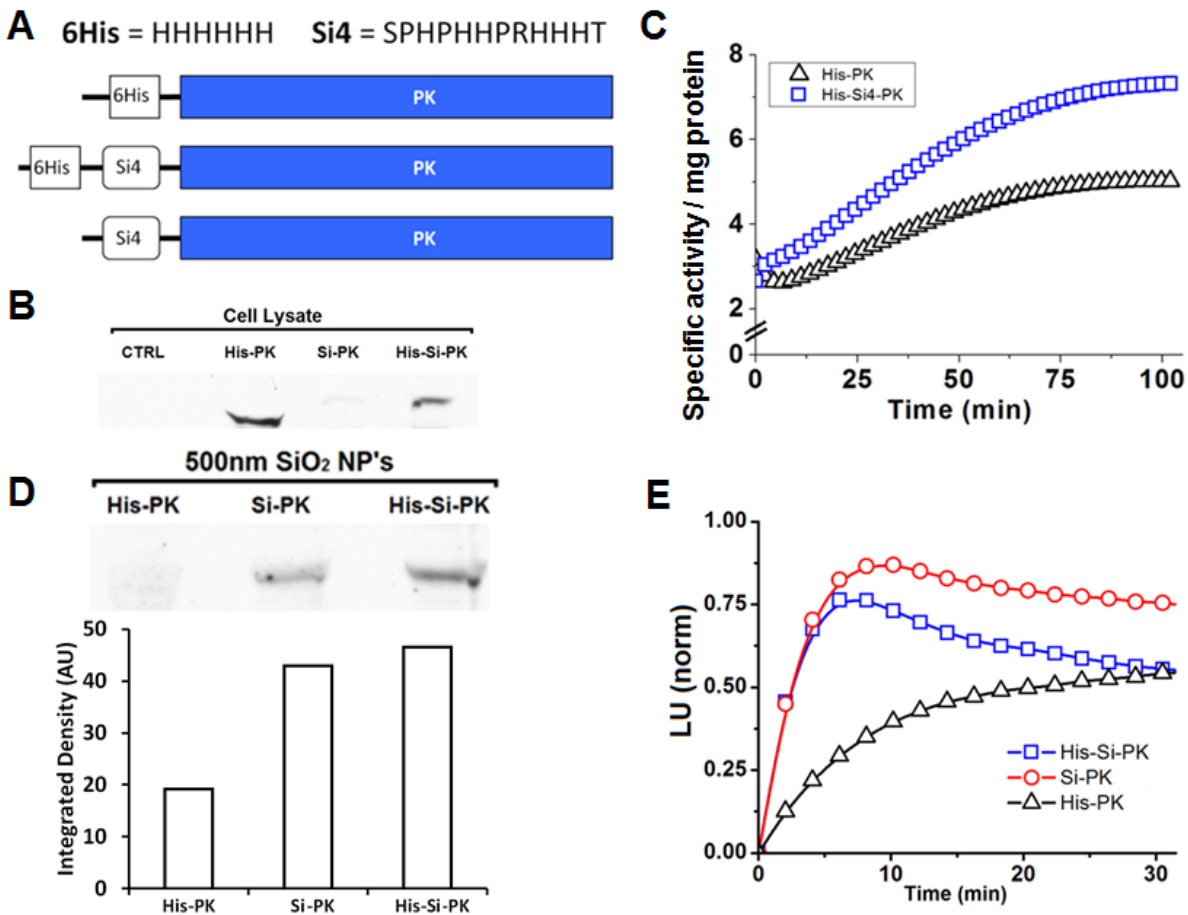


Figure 3.1: Construction and expression of PK-affinity tag fusion constructs. (A) Schematic illustration of fusion PK constructs indicating location of the His and Si4 peptide sequences. Three fusion plasmids were constructed for PK –His-PK, His-Si-PK and Si-PK. (B) HEK-293 cells were transfected with each of the 3 plasmids. 3 days later, cell lysates were separated by SDS-PAGE and then immunoblotted for PK expression, where His-PK showed highest expression level. (C) His-PK and His-Si-PK were purified (using the His-tag, see methods section) and tested for their specific activity when not tethered. Protein concentrations were determined with the Micro-BCA assay (Pierce, Rockford, IL), and purity of the samples was analyzed by SDS-PAGE and immunoblotting. (D) Immunoblot (top) and quantification (bottom) of protein bound to 500 nm SiO₂ NPs following incubation with whole cell lysates of His-PK,

His-Si4-PK or Si4-PK expressing cells. This comparison shows that the Si tag increases >2 fold the amount of protein bound to SiO₂ NPs. (E) The activity of His-PK, His-Si4-PK or Si4-PK fusion proteins was measured when immobilized on SiO₂ NPs following incubation of whole cell lysates with the 500 nm NPs. Oriented immobilization through the Si tag of His-Si-PK (blue squares) and Si-PK (red circles) results in comparable initial reaction rates, while His-PK lacking the SiO₂ affinity tag reveals a slower activity rate most likely due to its non-specific adsorption to the NPs.

conducted in strict accordance with the recommendations in the Guide for the Care and Use of Laboratory Animals (published by NIH).

3.2.5.1: Surgery and Occlusion. Male Sprague-Dawley rats (Charles River, Wilmington, MA) with average weight 400 g (std. dev. 83 g, range 260-530 g) were used in these experiments. Only males were used, to eliminate potentially confounding effects from the stage of estrus cycle. Animals were anesthetized with 5% isoflurane in oxygen and were maintained on 1.3-2.0% isoflurane. Anesthesia was adjusted to maintain both constant breathing rate of ~1 Hz, measured manually, and suppression of pedal withdrawal reflex. Rats were free breathing. In previous work⁹⁷, we have found that with these parameters it is not necessary to artificially ventilate animals for consistent cortical blood flow. Body temperature was maintained at 37.5 °C with a feedback controlled rectal thermometer. Glycopyrrolate (50 mg/100 g rat) was injected intramuscularly to suppress fluid buildup in the lungs. Rats were placed in a stereotaxic device and incision locations were shaved, cleaned and injected with bupivacaine (0.125 %, s.c.) for analgesia. The femoral artery was catheterized with PE 50 tubing for arterial blood draws. The skin and muscle on the right side of the skull were retracted, and a craniectomy was drilled from the temporal bone to just above the zygomatic arch. The dura was reflected. In experimental stroke animals, branches of the MCA were cauterized at both the entry and exit points from the field of view so that there was no flow visible in the exposed branches of the MCA. In sham animals no cauterization was used. The occlusion procedure took approximately 15 minutes, with time 0 recorded at the end of the occlusion procedure. The occlusions were visually checked every 15 minutes to ensure that the clots remained. In a few animals, some vessels became patent within the first hour and were recatherized. Experiments were conducted in matched pairs of sham animals and stroke animals. Blood (0.5ml) was drawn at 1 hour before occlusion (or sham), and after 0, 1, 3 and 6 hours post occlusion. In order to avoid dilution, flushing of the catheter was minimized. Fluids were replenished by subcutaneous injection of 0.5 ml of 5% glucose after every blood collection.

After the last blood draw, animals were overdosed with pentobarbital. Chest cavities were opened before the heart beat ceased and in some cases blood was drawn from a ventricular cardiac puncture. Animals were intracardially perfused with ~150 ml PBS and 300 mL 4% paraformaldehyde in PBS. Heads were stored in paraformaldehyde. Images were taken of each brain after extraction and before sectioning.

3.2.5.2: Fluoro-Jade C Staining. Brains were harvested and cryoprotected in 30% sucrose and then 60% sucrose for at least 24 hr each. Brains were frozen and cut into coronal, 45- μ m sections on a cryotome. For Fluoro-Jade C (FJC; Millipore) staining, sections were washed in 80% EtOH in 1% NaOH for five minutes, 70% EtOH for 2 minutes, and 0.06% KMnO₄ for 10 minutes. Sections were then incubated in the solution of 0.00015% of FJC solution (1:100 stock, according to manufacturer's instructions, dissolved in 0.1% of acetic acid) for 20 minutes. Sections were then washed with distilled water 3 times, for 1 minute each, at which time the slides were dried for 5 minutes and put into xylene solution for 5 minutes. Last, slides were dried for an hour and coverslipped with Permount (Electro Microscopy Sciences). Initially, FJC staining was performed at 1 mm-spacing throughout the brain. After the most anterior and posterior sections with FJC staining were identified, additional sections were stained to resolve the stroke volume with 200-300 μ m spacing.

3.2.5.3: Measurement of rat brain infarct volume and torn tissue area. Low magnification white light images of the entire section were photographed under a stereoscope. FJC staining was imaged with epifluorescence under 20x magnification using filters for FITC. The area labeled with FJC was manually identified by a person blinded to the treatment and marked on the low magnification, white light images of whole brain sections using ImageJ. For figures, images were normalized by calculating the mean and standard deviation of manually selected background region and then setting the minimum intensity to 4.2 x standard deviation below the mean, and maximum intensity to 7.2 x standard deviation above the

mean. Total FJC volume was obtained by multiplying each section's infarct area by the distance between sections.

In some sections, a part of tissue was torn in the stroke region. To compensate for missing tissue volume, the torn tissue area was obtained by subtracting the area of the ipsilateral from the contralateral side as calculated from the low magnification images. The volume of torn tissue was obtained by multiplying each section's missing tissue by the distance between sections. The torn tissue volume was then added to the FJC volume to calculate the total stroke volume.

3.2.5.4: Measurements of NSE activity and quantification by ELISA. Plasma was separated from whole blood samples using CAPIJECT Micro Collection Tubes (Terumo Medical Corporation, Somerset NJ). 50 μ l samples of plasma were added to individual wells in a 96-well plate, and reaction mix was added just before luminescence measurements were initiated (GloMax, Promega). Luminescence signal was integrated for 3 seconds, every minute for 50 minutes. Control wells (-2PG) were then subtracted from the raw data and LU were integrated over the first 20 minutes of the measurements. Integrated LU values of each time point were then normalized to t (-1 hr).

Rat NSE was quantified using an ELISA Kit, (R&D Systems, Inc., Minneapolis, MN) according to the manufacturer's directions. Non-Neuronal Enolase (NNE) was also detected using ELISA Kit, (antibodies-online.com, Atlanta, GA) according to manufacturer's directions. Assays were read using an Infinite M200Pro microplate reader (Tecan Trading AG, Maennedorf, Switzerland) and Magellan software (Tecan Austria GmbH, Grödigg/Salzburg, Austria).

3.2.6: Detection of NSE in blood samples from human subjects.

3.2.6.1: Plasma sample collection. This study was approved by Cornell and SUNY Upstate IRB. 5 ml of blood was collected from enrolled subjects into Na-heparin 6 ml tubes. Tubes were spun at 1000g for 5

minutes and then plasma was aspirated and placed over ice. Samples were divided and aliquots frozen for later analysis as indicated.

3.2.6.2: Detection of NSE in plasma samples from human subjects. 10 μ l of freshly collected plasma was diluted with 10 μ l of water and added to individual wells of a 96-well plate preloaded with lyophilized TET reagent mixtures for negative, test and positive control wells (in triplicates). The readout luminescence signal was integrated for 0.4 seconds, and read continuously for 25 minutes using a TECAN Safire plate reader. For calculation of NSE levels, the linear regression slope for the initial activity was calculated per each well. Then, control wells (-2PG) were subtracted from the test channel and normalized to the positive control well (with 2-PG and enolase). Plasma samples were sent for further analysis to ARUP laboratories (Salt Lake City, UT).

3.3 Results and Discussion

3.3.1: Enzyme immobilization to silica nanoparticles imparts advantages to coupled enzymatic efficiency.

We have previously shown that oriented immobilization of the glycolytic enzymes, TPI and GAPDH, enhances both their individual activities as well as the activity of their coupled sequential reactions in comparison to enzymes tethered via chemically-specific but non-oriented carboxyl-amine binding binding¹⁸. To test whether this would hold true for the coupled sequential reactions of PK and the non-glycolytic enzyme Luc, we generated mammalian PK and Luc expression plasmids, each as a fusion protein with two affinity tags, as described in the Materials and Methods section. Each of the constructs included an amino-terminal silica-binding peptide sequence (Si-tag)^{96,98} for immobilization of proteins onto SiO₂ nanoparticles (Si-NPs) and a 6xHis-tag to be used for protein purification (Figure 3.2 A, see also Figure 3.1).

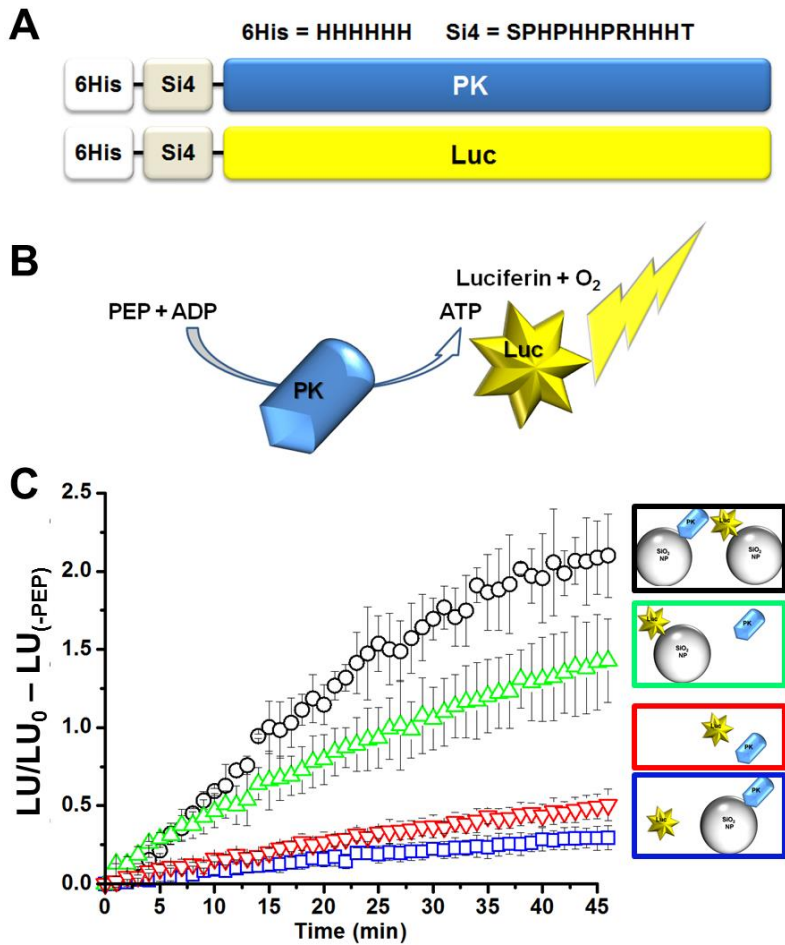


Figure 3.2: Immobilization of PK and Luc on NPs improves coupled reaction efficiency. (A) Schematic illustration of the 6XHis-Si tag fusion constructs for PK or Luc. (B) Schematic representation of the PK-Luc coupled reaction as used in the experiments described in C. (C) PK and Luc coupled activity was assayed in 4 combinations as indicated by the color coded schematic illustrations: black- (NP-PK) + (NP-Luc), blue- (NP-PK) + (soluble Luc), green- (NP-Luc) + (soluble PK) or red- (soluble PK + soluble Luc). All combinations included equivalent amounts of PK and Luc. Maximal coupled reaction efficiency, as calculated from normalizing each time point data to t0 (indicating the ratio of luminescence generated at each time point relative to the luminescence at the beginning of the reaction) and subtraction of the negative control well (no PEP, corresponding to the background luminescence signal), was observed when both PK and Luc were immobilized on NPs (each condition was tested in triplicates; data shown represents 3 individual experiments; AVG±STDEV)

To test our hypothesis that oriented immobilization would impart an improvement on the specific activity of the coupled reaction (Figure 3.2 B), we measured the coupled activities of various combinations of tethered and free PK and Luc (Figures 3.2 C and 3.3). Analysis of all four possible combinations revealed a significant increase in the readout signal when Luc was immobilized (green triangles, 3.01 ± 0.2 fold, $p < 0.001$) and an even larger increase upon immobilization of both Luc and PK (black circles, 4.25 ± 0.12 fold, $p < 0.001$). When Luc was in solution (not tethered), the coupled activity of the PK-Luc reaction was reduced, regardless of whether PK was in solution or tethered, suggesting that having Luc in close proximity with the source of ATP production (PK) was crucial for increased coupled reaction efficiency.

To investigate further the source of the improvement in Luc activity when tethered, we compared Luc in-solution versus immobilized. In agreement with previous findings⁹⁹, our measurements revealed a 10-fold average reduction in the sensitivity to ATP of immobilized Luc (data not shown). However, Luc tethered on the Si-NPs exhibited extended photon emission dynamics, with a slower decay rate when compared to the soluble protein (Figure 3.4 B). The differences in the enzymatic activity of immobilized Luc might result from a change in diffusion resistance and/or a slowing of kinetics due to conformational constraints. In terms of the PK-Luc coupled reaction, the reduction in Luc sensitivity was most likely compensated for by the prolonged emission kinetics. For example, placing Luc in closer proximity to PK (such as occurs with particle packing) would enhance the efficiency of ATP channeling by reducing the diffusion distance and effective local reaction volume, thereby increasing the effective local concentration of ATP, and enhancing luminescence output. Additional investigations of the impacts of enzyme tethering/proximity can be found in figures 3.3 and 3.5.

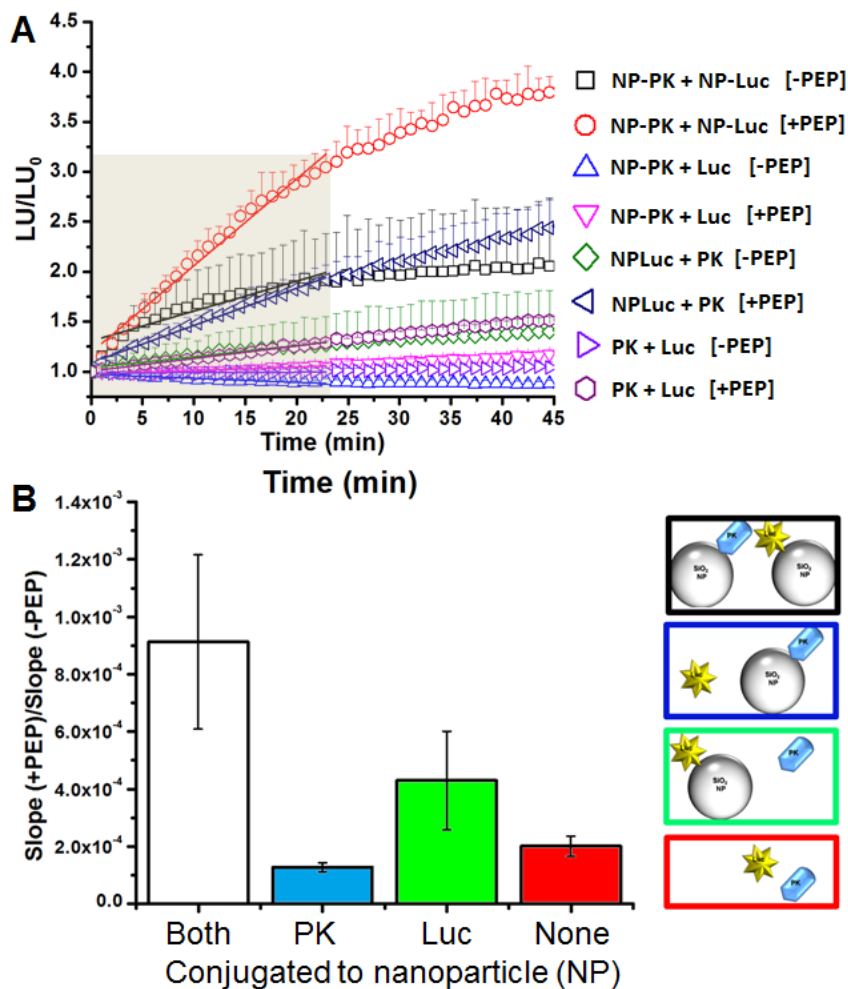


Figure 3.3: Supplementary analysis for PK-Luc coupled reaction as shown in Figure 3.2. (A) PK and Luc coupled activity was assayed in 4 combinations: (NP-PK) + (NP-Luc), (NP-PK) + (soluble Luc), (NP-Luc) + (soluble PK) or (soluble PK + soluble Luc). Luminescence output was measured for each combination with and without PEP, as indicated by the colored symbols. All combinations included equivalent amounts of PK and Luc. Here, coupled efficiency was calculated by subtracting the negative reaction (-PEP) from positive reactions (+PEP) slopes (indicated by solid lines). (B) Summary of data presented in A, shows that having both PK and Luc on NPs (black) facilitates reaction rates compared to other combinations. Each condition was tested in triplicates; data shown represents 3 individual experiments; AVG±STDEV.

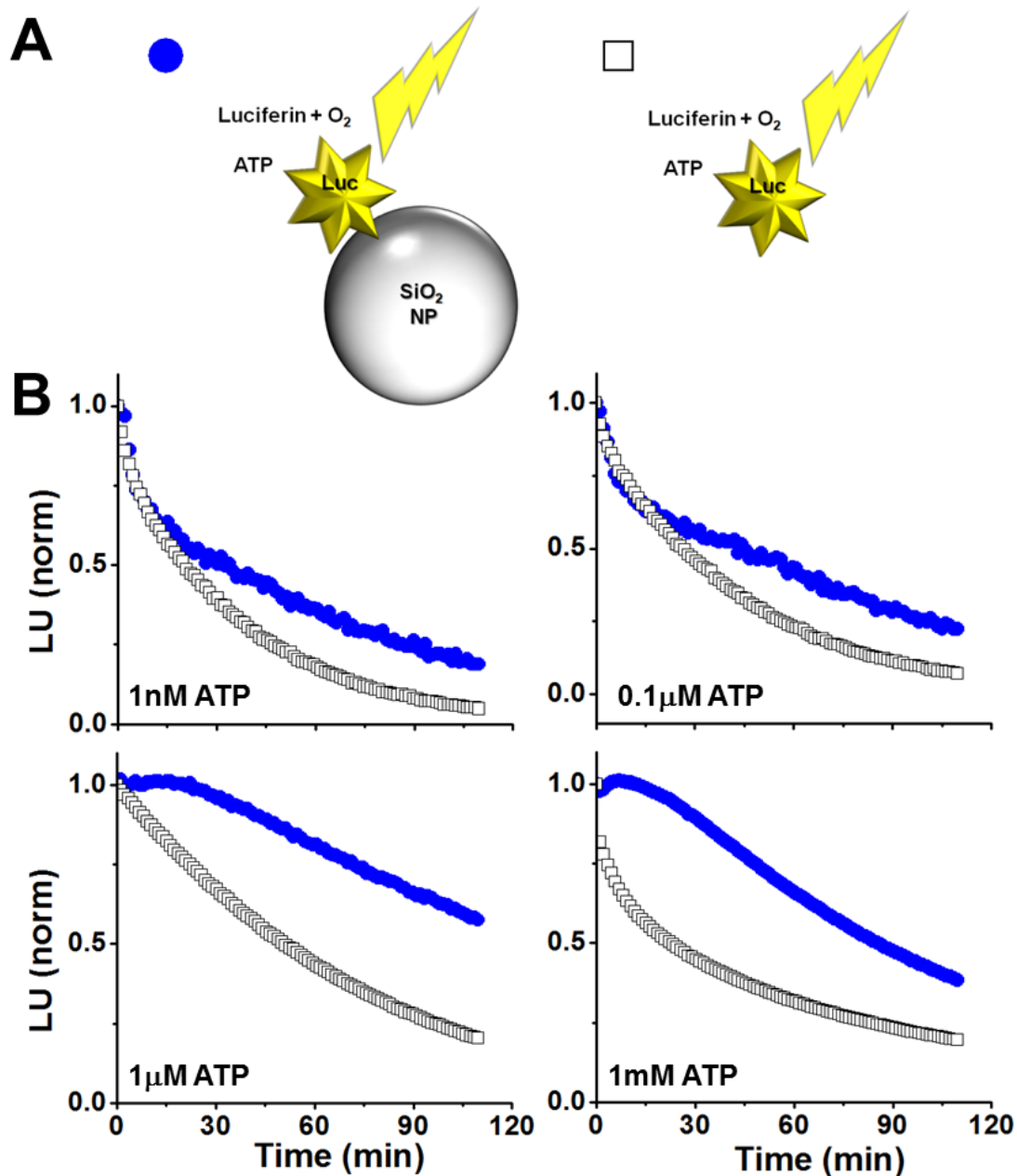


Figure 3.4: Determining the activity of His-Si4-Luc immobilized on silica NP's. (A) Schematic representation of experimental setup in the luciferase activity assay. (B) Representative traces showing the activity of Luc measured when immobilized on silica NPs (blue dots), or in solution (square) with various ATP concentrations. For these experiments, the luminescent signal was normalized against LU at time point 0, and plotted as a function of time, demonstrating a significantly slower decay time for Luc when tethered.

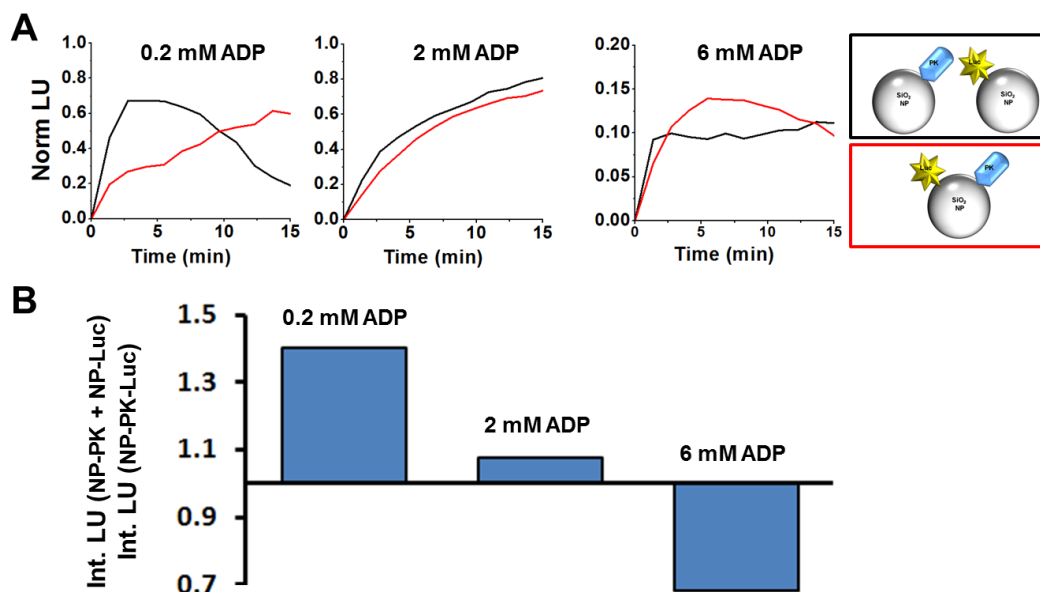


Figure 3.5: Co-immobilization of PK and Luc on single NPs reduced reaction efficiency when ADP was limiting. (A) To investigate the effect of enzyme proximity on coupled activity more directly, His-Si-PK and His-Si-Luc were immobilized on 500nm silica NPs separately (black) or together (red). Luminescence signal in the presence of 0.22 or 6 mM ADP was normalized to t (0 min) and plotted against time (all other conditions/substrates were kept the same). (B) Surprisingly, we found the activity of the coupled reactions to be significantly reduced when the enzymes were co-tethered on single particles versus tethered on separate particles. There are multiple possible explanations for this finding, ranging from steric hindrance between the two proteins when co-tethered, to interference by Luc with PK tetramers, to a competition between the enzymes for interaction with ADP^{100, 101}. Such competition would reduce substrate availability for PK, resulting in overall reduced luminescence. To distinguish between these possibilities, we repeated the experiment with increased concentrations of ADP, and found that a 10-fold excess or more of ADP reversed the reduction in activity (middle and right panels), suggesting that competition for ADP was largely responsible.

3.3.2: Detection of biomarker NSE using sequential immobilized enzymes.

We next hypothesized that the increased efficiency of the immobilized coupled reactions might provide a sensitive and rapid luminescence based assay for detection of the BP biomarker NSE. This would occur through a 3-step coupled reaction as follows – enolase/NSE catalyzes the conversion of 2-phosphoglycerate (2-PG) to phosphoenolpyruvate (PEP), PK in turn converts PEP and ADP to pyruvate and ATP, with the latter being used by Luc to generate a photon of light. We first tested this hypothesis using the non-neuronal isoform α -enolase (ENO). As shown in Figure 3.6 A, the sensitivity of the tethered enzymes (red, PK and Luc tethered separately to NPs) was significantly higher than that of freely diffusing enzymes (blue) when detecting ENO activity. In particular, higher sensitivity of the PK-Luc coupled reaction was observed at lower ENO concentrations (Figure 3.6 A inset).

Next, we sought to determine whether the NP-PK and NP-Luc coupled reaction could detect physiologically relevant concentrations of human NSE ($< 8.7 \pm 3.9$ ng/ml¹⁰²). Figure 3.6 B shows a representative dose response experiment where sub-physiological amounts of commercial human NSE were added to the reaction mixture in the presence of NP-PK and NP-Luc (tethered separately). The luminescent signal generated by Luc was integrated over 10 minutes, showing statistically significant differences for each concentration of NSE. These results indicate that using immobilized PK-Luc coupled reactions provides sub-physiological sensitivity for NSE, at concentrations well below typical pathological plasma levels, with rapid detection times.

3.3.3: Detection of NSE in rat stroke models using tethered enzyme system compared to ELISA detection.

The improved sensitivity and kinetics of NSE detection with the tethered coupled enzymatic reactions encouraged us to test our biomarker detection assays in the complex environment of blood plasma. For these experiments, we used a rat model for BP, in the form of a focal stroke that was

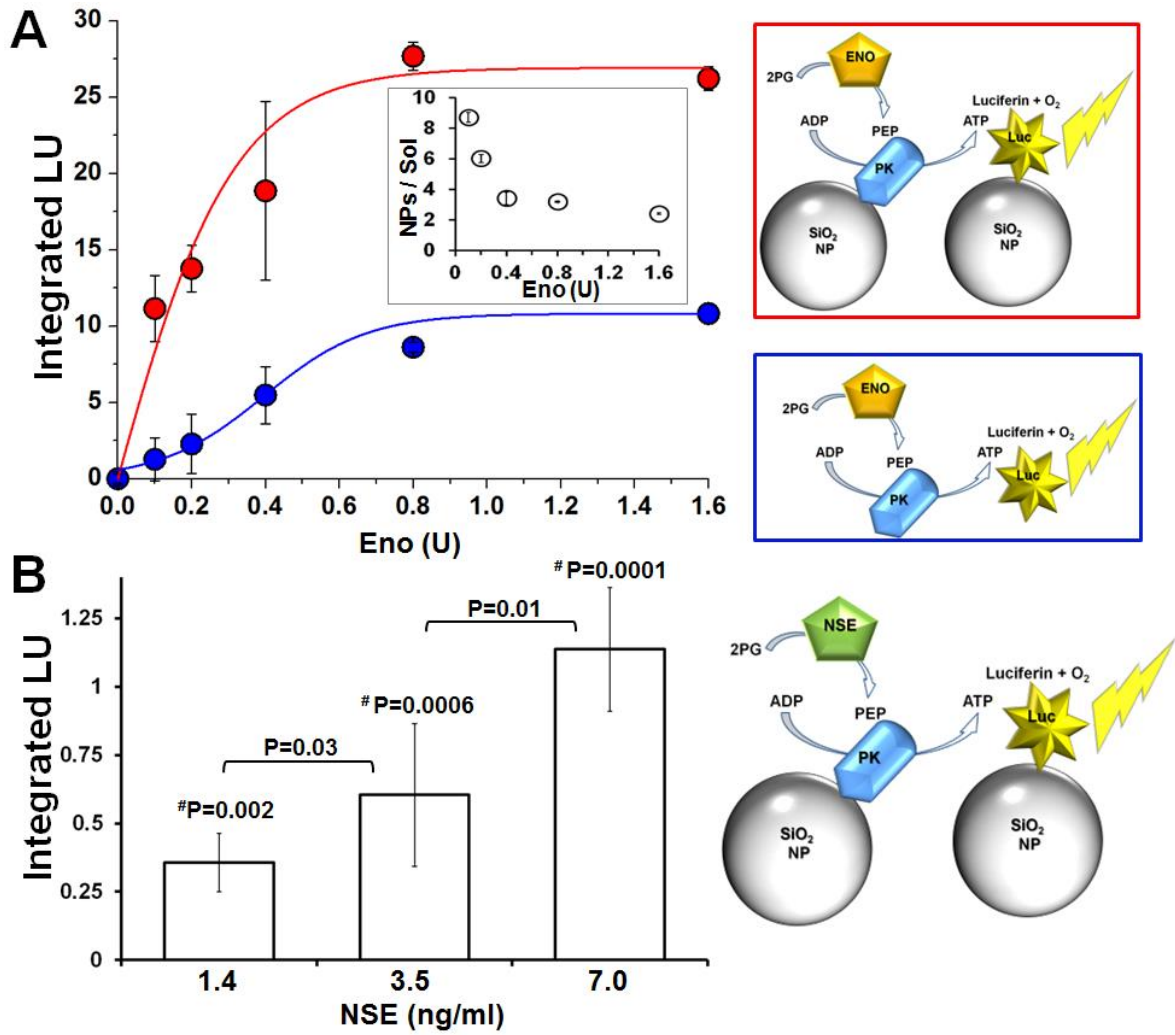


Figure 3.6: Improved sensitivity for enolase detection via its enzymatic activity when using tethered PK and Luc. (A) Comparison of the detection sensitivity for enolase activity (Eno) as measured by NP-PK + NP-Luc (red) vs. PK + Luc in solution (blue). Increasing concentrations of Eno were added to immobilized or freely diffusing enzymes in reaction buffer. Luminescence was detected and integrated over 10 minutes at RT and plotted against Eno final unit amount (lines were added to guide the eye). The inset shows the ratio of the enzymes' activities on NPs versus in solution as a function of units of ENO. Data presented as AVG±STDEV. (B) NSE detection via PK and Luc coupled activity was performed as indicated in the schematic illustration (right). His-Si-PK and His-Si-Luc were immobilized on 500 nm NPs and mixed with reaction buffer supplemented with increasing concentrations of human NSE.

Luminescence readout was normalized to t0 (first read) values and plotted as a function of time. Then, the luminescent signal was integrated for first 10 minutes, and a reading from the zero NSE well was subtracted from the collected signal. The sensitivity of the tethered enzyme assay was about 5 times higher than the reported average physiological NSE blood concentration (8.7 ± 3.9 ng/ml¹⁰²). P values were calculated using student's t-test for comparisons between NSE concentrations; values marked with # P were calculated for significance when compared against 0 ng/ml NSE.

induced by clotting the distal branches of the middle cerebral artery (MCA). Peripheral blood samples from experimental BP and sham-operated control rats were taken 1 hour before and 0, 1, 3 and 6 hours after occlusion of distal MCA branches. Luminescence output was integrated over 10 minutes from the NSE-PK-Luc coupled reaction (PK and Luc tethered separately to NPs), but with the active NSE originating from the damaged/dying neurons. Stroke-induced cell death in the rats was confirmed with Fluoro-Jade C staining (see details in Materials and Methods section). The volume of brain with damaged neurons was on average 11.25 ± 4 mm³ (n=4, 3.7 A) in the stroke animals, and 0.002 ± 0.001 mm³ in the sham-operated controls (3.7 B n=4). Integrated luminescence values at each time point were calculated by subtracting a negative control reaction (lacking the NSE substrate, 2-PG) from the test reaction (that included 2-PG). Figure 3.7 E summarizes the data collected from 10 rats (5 stroke and 5 control), showing a statistically significant increase in NSE levels as soon as 1 hour post-occlusion, whereas control rats showed no increase in plasma NSE levels (detailed time point data for each rat are provided in panels 3.7 C and 3.7 D).

Next, we compared results from our tethered enzyme technology (TET) versus quantification of the rat NSE as obtained from a commercial ELISA kit, which is currently the standard detection technology. Consistent with the results from the coupled enzymatic assay at that same time point, the ELISA revealed a 2-fold increase in NSE concentration at 6 hours post stroke (Figure 3.7 F). No elevation was found in non-neuronal isoforms of enolase (NNE) as measured using a NNE ELISA kit (data not shown), demonstrating that the source of enolase activity that we measured was indeed NSE. Importantly, while the measurements of NSE concentration using the “gold standard” ELISA assays took over 3 hours, the TET based assay provided results within 10 minutes. The ability of the tethered enzyme system to detect these changes in plasma NSE with an assay time of 10 minutes positions this technology well within the requirements for time sensitive PoCT applications.

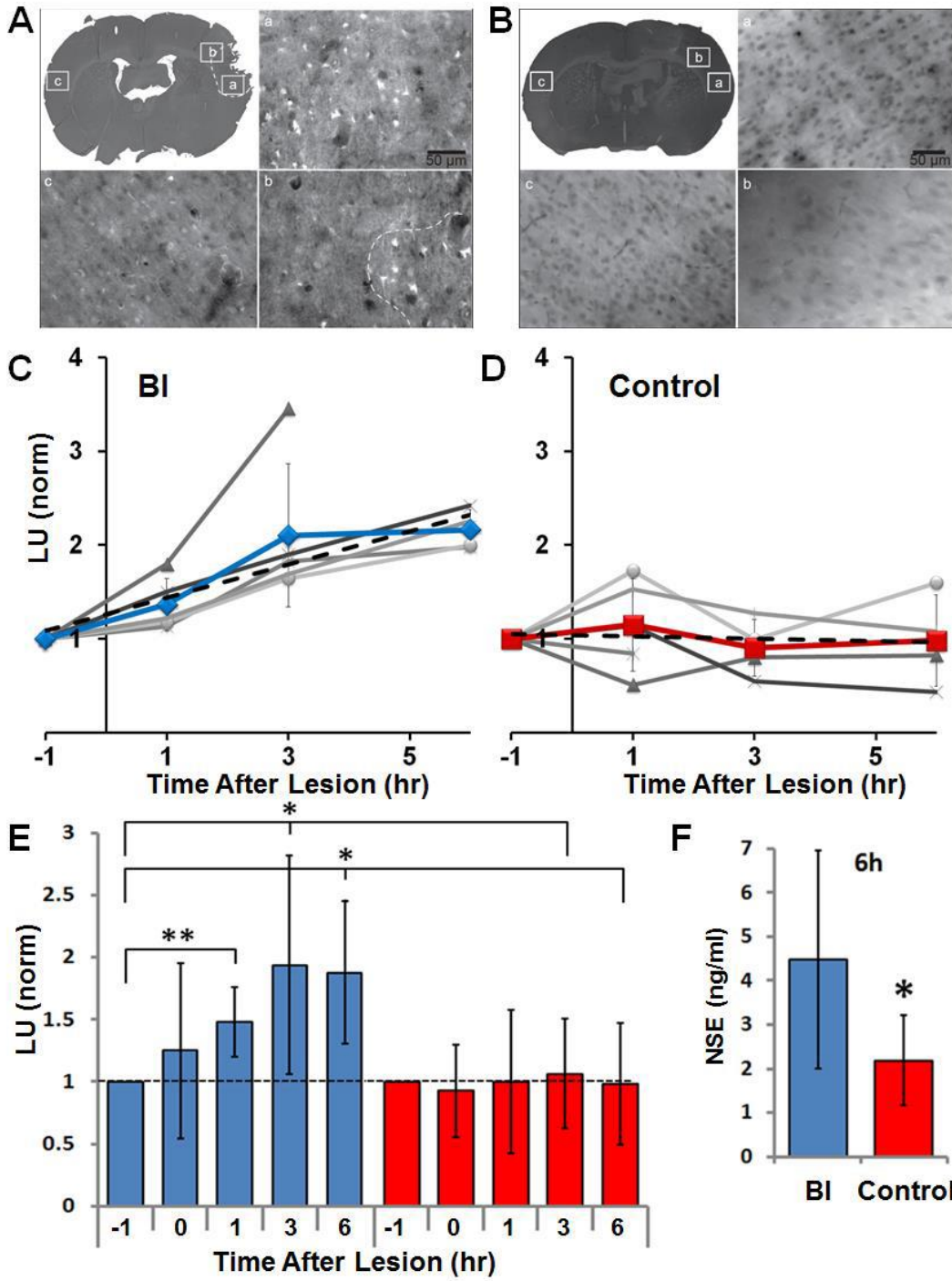


Figure 3.7: Using NP-PK and NP-Luc for rapid detection of NSE in a rat model for brain injury (BI). (A) Fluoro Jade-C staining for measurement of damaged brain tissue volume. The presence and absence of FJC-labeled degenerative neurons were imaged with epifluorescence under 20x magnification using filters for FITC. (a) Region with abundant FJC staining (bright cells) on lesioned side. (b) Region at the

edge of FJC staining. (c) Region that is contralateral to (a) that did not show any FJC staining. Dotted line in B and low magnification inset indicates manually-mapped border between FJC positive and negative areas. **(B)** FJC staining in control brain section. (a) and (b) are in area of craniectomy. **(C-D)** Individual rat data (C-BI and D-control) for NSE measurements at each time point (grayscale lines indicate data points for individual animals, line with symbol indicates the mean \pm standard deviation) as performed by tethered PK and Luc assay, and normalized to time point -1 hour. Plasma samples were collected from BI induced or control rats pre (-1 hr), and post occlusion (0, 1, 3 and 6 hr). The mean slope of the trend (dashed line) was calculated averaging individual slopes in each group (BI=0.26 with 0.95 confidence interval, control=-0.02 with 0.38 confidence interval). **(E)** Summary of rat BI model experiments showing a statistically significant increase in NSE plasma levels in BI (blue bars) vs. control (red bars) rats as soon as 1 hour post occlusion. **(F)** Measurements of NSE in plasma from rats using ELISA showed elevated levels in BI compared to control rats at the last time point (6 hr post-occlusion). P values – $0.05 < * < 0.1$, $0.01 < ** < 0.05$. Data from 10 rats were included in our analysis, with the exclusion of 3h and 6h time points for one control animal that died (at 2h mark), and a 6h time point for a BI animal which died and was found to have a large hemorrhage at the base of the brain.

3.3.4: Detection of NSE in human plasma samples from patients using tethered enzymes compares to ELISA detection.

Moving forward from an animal model, we next tested TET's ability to detect NSE in the even less defined environment of human plasma. Blood samples were collected from consenting patients seen at the Central New York Alzheimer's Disease Assistance Center (ADAC) at SUNY Upstate Medical University using Na-Heparin tubes. Plasma was then divided with a portion of the sample tested immediately using TET and the rest frozen at -80°C for later confirmation via commercial ELISA. We ran this experiment using TET in the form of a first generation PoCT technology for human NSE testing. Namely, reactions were designed to work with minimal plasma volume in white 96 well plates in which all test and control reaction components had been lyophilized. This allowed us to simply add 10 μl of freshly collected plasma into the pre-loaded wells and immediately start measuring the light output with a conventional plate reader. TET reaction reading was completed within 10 minutes from the addition of plasma to the pre-loaded wells, where each test included triplicate negative control wells (reaction lacking 2PG), positive control wells (pre-loaded with enolase) and test wells, so that a total of 90 μl of plasma was used for each subject tested (a volume able to be obtained from less than 4 drops of blood). To validate the accuracy of the TET results (representative data shown in Figure 3.8 A), plasma samples were sent for lab testing (ARUP labs, Salt Lake City, UT). Using a Pearson's correlation test, we compared TET and ELISA data finding a significant correlation of 0.81 between the two approaches (Figure 3.8 B).

3.4 Conclusions

Our results suggest that enzymes tethered via oriented immobilization can provide a PoCT platform enabling simple, rapid and objective testing for biomarkers associated with hard to diagnose and time

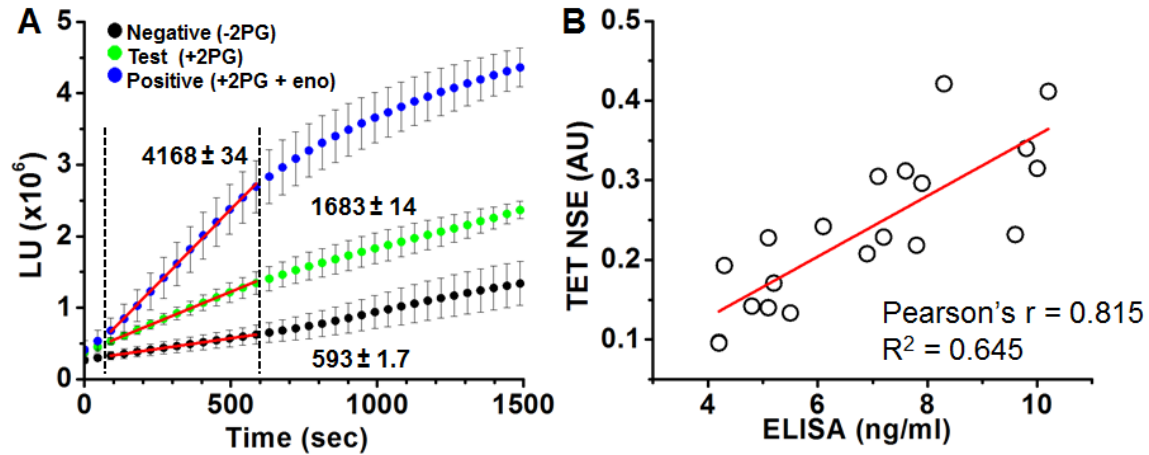


Figure 3.8: Using the tethered enzyme assay for rapid detection of NSE in human subjects. (A)

Representative data as measured from a total of nine wells per subject (triplicate measurements of negative control with no 2PG; the test sample with 2PG; and positive control wells with 2PG and enolase (Eno); mean \pm STDEV) For calculation of NSE levels, slopes of averaged curves were calculated for the first 0.5-10 minutes of the enzymatic reactions (indicated by the red linear fit in between the dashed lines), then test wells were normalized to positive and negative wells (see methods section). **(B)** High correlation was found between NSE measurements by ELISA (ng/ml) vs. TET assay (AU represents the normalization of test reaction to the negative and positive reactions, as illustrated in A and described in the methods section) as of the human plasma samples. Line indicates best fit. Pearson's $r = 0.815$, $n = 20$.

sensitive diseases. We focused on NSE for this proof of concept because it has been shown to convey clinically relevant information for several BPs.

Immobilized enzymes present several important advantages for medical applications including stability and spatial organization in a device, whether with a microfluidic card or paper chromatography. Of note, our data show that oriented enzyme immobilization also significantly improved the efficiency with which coupled enzymatic reactions occurred. This is of special importance because use of coupled enzymatic reactions allows signal amplification at both the stages of biomarker detection and transduction of signal into the luminescent readout. When combined with the inherently enhanced sensitivity and speed of catalytic activity, tethered enzymes provide some of the highly desired features expected from a PoCT diagnostic platform. Demonstrating their suitability for this purpose, we showed *in vitro* the advantages of using tethered versus soluble enzymes. We showed that TET-based systems could detect physiologically and pathologically relevant concentrations. Importantly, the immobilized enzyme-based detection system provided an ultra-rapid analysis (i.e. within 10 minutes) even when using plasma samples obtained from rat BP models or human patients.

The high correlation between ELISA and TET suggests circulating NSE enzymatic activity corresponds very well with the amount of protein. This comparison between TET and ELISA in detection of NSE raises another important finding regarding the dynamic range for detection provided by these two methods. Whereas the ELISA method provides a linear detection range, the enzyme-based assay offers close to a 2-fold larger dynamic range (as calculated from the max to min values for each assay). This finding revealed another feature contributing to the increased sensitivity of TET versus antibody capture techniques.

One potential criticism of use of tethered enzymes is that the range of biomarkers able to be detected through enzymatic reactions represents a limited subset of target analytes. However, there are numerous biomarkers with bona fide enzymatic activity (e.g. nucleoside diphosphate kinase A (NDKA

¹⁰³,) phosphoglycerate mutase (PGM ³³), or are modulators of enzyme activity (e.g. calcium ¹⁰⁴, magnesium ¹⁰⁵), or are substrates and metabolites of enzymatic reactions (e.g. glutamate and glucose ¹⁰⁶). We are currently designing and testing TET-based approaches for multiple classes of target analytes, beyond enzymes.

Together, our data support further investigations of enzymes tethered to NPs via oriented immobilization in PoCT diagnostics. The advantages of spatial control of enzyme activities, rapid and sensitive detection with signal amplification at both detection and transduction into luminescence output, combine to make TET a highly attractive alternative to antibody-based detection.

CHAPTER 4

ORIENTED IMMOBILIZATION OF ENOLASE WITH AN APPLICATION IN PHOSPHOGLYCERATE MUTASE DETECTION[‡]

4.1 Introduction

Some biomarkers of disease are enzymes that can be detected through sequential enzymatic reactions. For example, sequential enzymes in the glycolytic pathway, enolase and phosphoglycerate mutase (PGM) have been described as biomarkers for several pathologies. One of the most studied biomarkers for neurological pathologies is neuron-specific enolase (NSE), which is released into the bloodstream from dying neurons^{28, 30, 107}. Similarly, PGM is released after neural injury³³ as well as upon acute myocardial infarction^{32, 108} and is upstream of NSE in the glycolysis pathway. By immobilizing the tenth glycolytic enzyme, pyruvate kinase (PK), in a microfluidic device, the amount of NSE present in serum can be detected through a sequential reaction. Going one step further, immobilizing both PK and enolase, enables a device to detect and quantify PGM. Much attention is focused on developing point-of-care test (PoCT) technologies to detect pathology-specific biomarkers released into the bloodstream^{28, 109}. These devices could reduce the time required for diagnosis by obtaining fast results on-the-scene or in an ambulance. Specifically, NSE and PGM could be utilized for diagnosing time-sensitive pathologies, such as brain pathologies such as stroke or mild traumatic brain injury (mTBI) and acute myocardial infarction. Our lab has already functionally immobilized PK to nanoparticles (NPs) (Chapter 3). However, to detect PGM, enolase must also maintain activity after being immobilized on a surface.

Retaining enzyme function while immobilized to a solid support is currently a challenge for hybrid organic/inorganic devices. Many considerations need to be taken into account when immobilizing a

[‡] Modified from Lata JP et. al. Manuscript prepared for publication and will be submitted pending acceptance of preceding chapter.

protein to a solid support, such as: orientation of the enzyme relative to the surface, the ability for the enzyme to undergo conformation changes, and the distance of the enzyme from the surface.

Nonspecifically adsorbing a protein to a solid surface may change the protein's structure, forcing it to partially or completely denature^{9, 12, 23, 110-112}. To solve this issue, chemical techniques have been implemented to specifically tether a protein to surfaces via chemical groups present on the protein's surface^{10, 113}. One common technique is through carboxyl-amine binding, wherein a surface is chemically modified with carboxyl groups (COOH) which are then activated to allow binding with amine groups on the proteins. Unfortunately, this method has the potential for binding multiple locations on a protein and inhibiting conformation changes. It also has the possibility of burying the binding and catalytic domains on the enzyme. Recently, more controlled techniques have been developed where a specific site on a protein is tethered to a surface, thereby allowing for 'oriented immobilization'^{20, 114-116}. This is accomplished via protein engineering, by fusing an enzyme with an affinity tag to a specific domain at the DNA level. This strategy has been shown to improve enzyme activity compared to other methods^{18, 19, 117}. Immobilizing enzymes allows for spatial organization, functional separation (enzyme-enzyme, enzyme-substrate) and reusability. In conjunction with microfluidic technology, immobilization of proteins offers the means for device miniaturization, a superb level of spatiotemporal control, increased throughput, and reduced device costs.

Enolase (2-phospho-D- glyceratehydrolyase) is the ninth glycolytic enzyme which catalyzes the dehydration of 2-phosphoglycerate (2PG) to phosphoenolpyruvate (PEP). The activation of enolase requires a divalent metal ion (Mg^{2+}) making it a metal-activated metalloenzyme¹¹⁸. There are several isozymes of enolase with variable ability to be functionally immobilized. Enolase is present in eukaryotes in four prevalent homodimer isozymes: Eno1 (α), which is the most common isozyme and is located in almost every cell; Eno2 (γ), which is a neuron-specific enolase; Eno3 (β), a muscle-specific isozyme; and Eno4 (ENOS), a germ cell-specific (GCS) isozyme located in sperm¹¹⁹⁻¹²¹. Eno4 activity and expression are

still under investigation and are largely unknown. Our lab has previously identified that glycolytic GCS isozymes often have a region which tethers them to a large structural element in the principal piece of the sperm's tail known as the fibrous sheath ¹⁶. Through a biomimetic strategy and genetic engineering we have successfully replaced the gcs domain of hexokinase and GAPDHS with a linker and a hexahistidine tag (His-tag) which will tether these enzymes to a Ni-NTA coated surface to create oriented immobilization of the enzyme, as seen in sperm. Our lab has shown that oriented immobilization is critical for retaining maximal enzymatic activity for GCS enzymes ¹⁹.

In this study we compare the tethered activities of Eno4 and Eno1, the most abundant isozyme of enolase. We functionally immobilized enolase via His-tags to silica-coated magnetic nanoparticles (SiMNPs). In doing this, we made and compared four constructs, Eno1N, Eno1C, Eno4N and Eno4C which are derived from Eno1 or Eno4 with a His-tag on the N or C terminus, respectively. This will enable us to determine whether the location at which the enzyme is tagged has an impact on the enzymatic activity.

Another comparison will be made with two different binding techniques: oriented immobilization; binding through the optimized His-tag to a Ni-NTA coated surface, or chemical binding; binding through the amine groups on the enzyme to a COOH-coated surface. For these experiments our surfaces are 100 nm SiMNPs (Fig. 4.1). The magnetic properties of the SiMNPs allow for easy washing without the need for high speed centrifugation which could have detrimental effects on the enzymes. The silica coating gives the SiMNPs a higher dispersibility and a smooth surface compared to the rough magnetic Fe₂O₃ core ²⁰.

This chapter also evaluates a practical medical application for use of tethered enolase for rapid diagnosis of various pathologies for which PGM is a biomarker. To implement this, PK and Eno are both engineered with His-tags (His-PK and His-Eno). His-PK and the functional His-Eno are then co-immobilized to SiMNPs through either oriented or chemical immobilization as before and compared. With an ultimate goal of using this technology in a PoCT device, we again linked detection to a

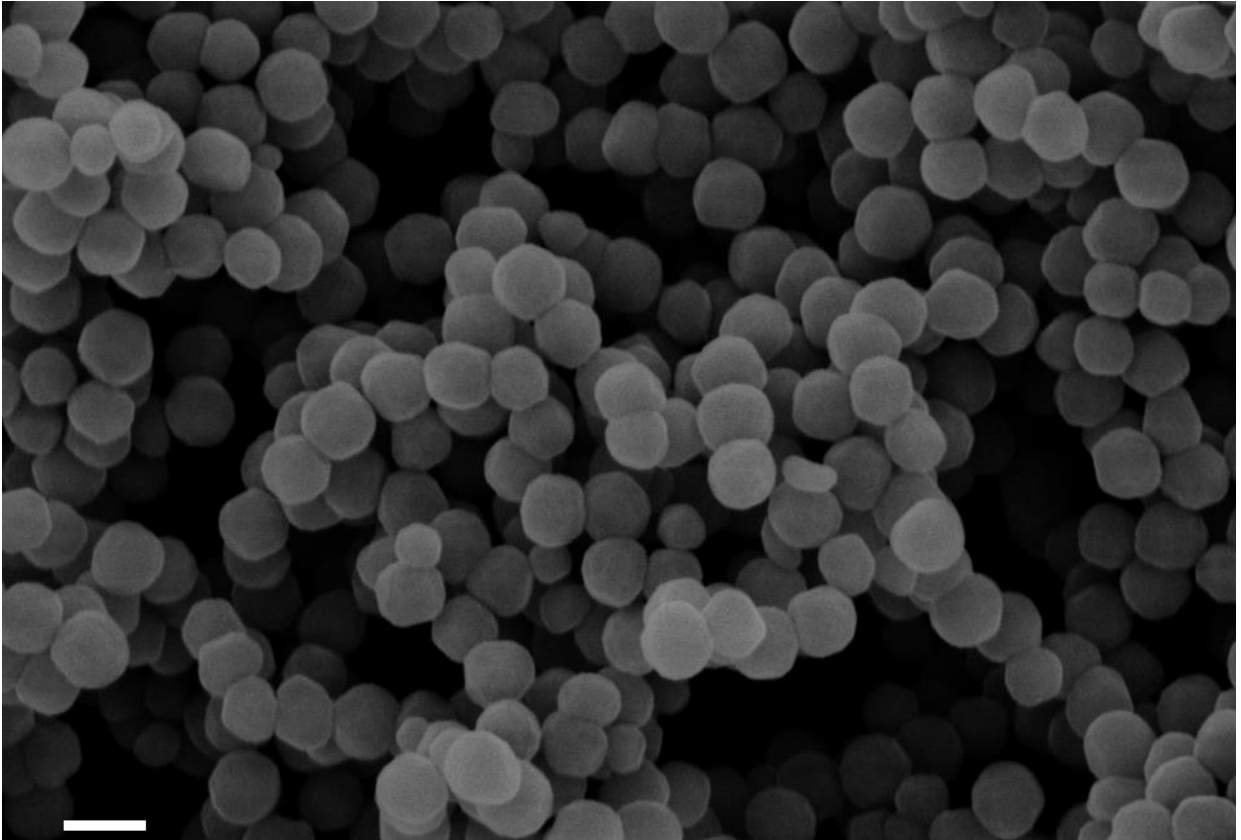


Figure 4.1: Characterization of SiMNPs. 100 nm SiMNPs were synthesized and dried for viewing under an SEM (Philips XL-30 field) at 15 kV. White scale bar represents 200 nm.

luminescent output, rather than absorbance. For this we used a His-tagged luciferase enzyme (His-Luc) and co-immobilized all three enzymes (His-PK, His-Eno, His-Luc) to detect varying amounts of His-PGM which has higher stability yet is analogous in activity to commercial PGM. This platform utilizes enzymatic reactions which will aid in developing PoCT for time sensitive pathologies such as neurological injury and acute myocardial infarction.

4.2 Materials and Methods

All materials and reagents were purchased from Sigma-Aldrich (MO, USA) or ThermoFisher Scientific (MA, USA) unless otherwise stated.

4.2.1: Protein Engineering. Four enolase constructs were engineered with His-tags on either the C or N terminus (Eno1N, Eno1C, Eno4N, Eno4C). Eno1N (aa 1-434), Eno1C (aa 1-433), Eno4N (aa 1-618) and Eno4C (aa 1-617) were identified from mouse alpha-enolase (NM 023119.2) and mouse GCS-enolase (NM 178689.4). cDNA was synthesized using SuperScript III 1st Strand Synthesis kit from CD-1 mouse testis RNA. EnoN and EnoC constructs were cloned into pcDNA4/HisMax[®]-TOPO[®] vector and pcDNA[™]3.1/V5-His-TOPO[®] vector, respectively. Constructs were validated by sequencing and amplified with a PureLink[®] Hi Pure Plasmid Filter Maxiprep Kit. 30 ml of FreeStyle[™] HEK 293-F cells (1x10⁶ cells/ml) were transfected with 36 µg of purified plasmid using FreeStyle[™] MAX 293 Expression System. Cells were harvested and lysed using sonication (Sonafier 250, Branson). Individual His-tagged enzymes were purified with Ni-NTA Agarose (Qiagen Corp.) and underwent four washes with 40 mM imidazole in native purification buffer [100 mM sodium phosphate, 250 mM NaCl, pH 7.9], followed by an elution with 400 mM imidazole in native buffer. Imidazole was then immediately removed with PD MiniTrap G-25 (GE Healthcare Life Science) and MOPS buffer [50mM, pH 7.9] was added. Enzyme purity was examined using both western immunoblotting and Coomassie Brilliant Blue R-250 gel staining. Western

blots were performed using anti-His antibodies for N-term and C-term His, respectively. Initial enzyme concentration was determined from Pierce Micro BCA Assay (Thermo Fisher Scientific Inc.). Final enzyme concentration was calculated after adjusting for impurities noticed on the Coomassie stained gel using densitometric analysis. His-tagged N-terminus mouse muscle pyruvate kinase (His-PK) (NM 011099.3), His-tagged N-terminus firefly luciferase (His-Luc) (luciferase 2 gene purchased from Promega) and His-tagged N-terminus mouse muscle phosphoglycerate mutase 2 (His-PGM) (NM 018870.3) were similarly constructed and purified using the procedures above.

4.2.2: Silica Magnetic Nanoparticle (SiMNP) Synthesis. Purified His-tagged enzymes were immobilized on 100 nm SiMNPs, which were conjugated with either COOH or NTA groups. Magnetic (Fe_3O_4) nanoparticles were synthesized in a solvo thermal system^{122, 123}. Briefly, 0.82 g of FeCl_3 (Fisher) was dissolved in 40 ml of ethylene glycol to form a clear solution. 3.6 g of NaAc (Fisher) and 2 ml of ethylenediamine (Sigma) were continuously added into the above solution with vigorous stirring for 30 min. The mixture was then transferred into a 50 ml teflon-lined stainless-steel autoclave and reacted at 200 °C for 12 hours. After the autoclave was cooled to room temperature, the black precipitates were collected, rinsed with ethanol and dried at 60 °C for 3 hours. The synthesized nanoparticles were characterized using scanning electron microscopy (SEM, Philips XL-30 field, 15 kV). 26 mg Fe_3O_4 nanoparticles were mixed with 20 ml 2-propanol and 40 ml ethanol. Then 0.5 ml deionized water and 1.5 ml ammonia solution (25% by wt) were consecutively added to the reaction mixture. Under continuous mechanical stirring, tetraethyl orthosilicate (Sigma) and carboxyethylsilanetriol (disodium salt, 25% in water) (Gelest, Inc.) at a ratio of 1:4 (v/v, total 400 μl) were added into the reaction solutions. The reaction was allowed to proceed at room temperature for 8 hours. After the coating reaction, the core-shell nanostructures were separated from the reaction medium by a magnet block, and dispersed into ethanol. The separation procedure was performed at least three times. The modified

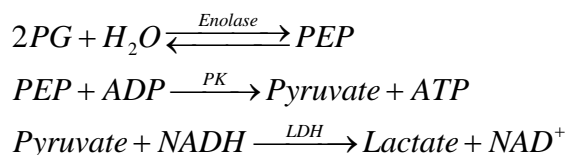
MNPs (SiMNPs) were dried at 60°C for 3 hours and characterized using scanning electron microscopy (SEM, Philips XL-30 field, 15 kV) (Fig. 4.1) and Fourier transform-infrared spectroscopy (FTIR, Bruker Optics - Vertex80v).

4.2.3: Oriented Enzyme Immobilization. The SiMNPs were split into two groups, half being used for chemical binding and half for oriented immobilization. For chemical binding the COOH groups were activated using 1-ethyl-3-(3-dimethylaminopropyl) carbodiimide (EDC) and N-hydroxysuccinimide (NHS) in a 3:1 ratio. Excess EDC and NHS were washed out with MilliQ water. Enzyme was then conjugated directly to the carboxyl groups (as described below) via carboxyl-amine binding forming a chemically-specific but non-oriented immobilization. For the oriented immobilization the COOH groups were activated as above, but enzyme was not yet added. Nitrilotriacetic acid (NTA) was added instead and conjugated through carboxyl-amine binding. Excess NTA was removed with MOPS buffer [50 mM] washes. NiCl₂ solution was then added to produce Ni-NTA. Additional washes with MOPS buffer removed excess Ni and Cl. Enzyme was then added and conjugated to the Ni via the His-tag, tethering the enzymes via oriented immobilization.

In each immobilization strategy the enzymes were immobilized in different ratios to SiMNPs depending whether it was a single enzyme binding or co-tethering with multiple enzymes. A single enzyme immobilization used 1.5 µg of His-Eno added to 100 µg of SiMNPs and incubated on ice for 15 minutes. For two enzyme co-immobilization, 1.5 µg of His-Eno1C and 0.5 µg of His-PK were added to 100 µg of SiMNPs and incubated on ice for 15 minutes. This 3:1 ratio for His-Eno1C and His-PK was based on specific activity, since His-PK had three times more activity than His-Eno1C. For three enzyme co-immobilization, the reaction was optimized to the final ratio of 4 µg His-Eno1C, 1 µg His-PK and 2 µg His-Luc. After the 15 minute incubation on ice the supernatant was collected and three washes were

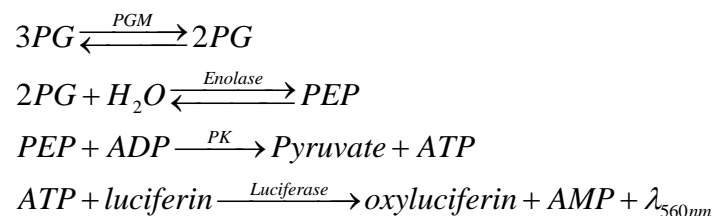
performed using MOPS, which were similarly collected. The amount of protein bound to the SiMNPs was calculated by subtraction with a BCA assay.

4.2.4: Enzyme Activity Assays. In-solution activity assays were carried out based on the final concentrations present in the enzyme assay protocols from Sigma. These assays were performed in 96-well plates and read with absorbance using a plate reader (Infinite® 200 Pro, Tecan Group Ltd.). For the enolase activity assays, each 100 µl volume reaction utilized the following reaction mixture: pyruvate kinase (PK) [2.5 units/ml], L-lactate dehydrogenase (LDH) [3.5 units/ml], adenosine diphosphate (ADP) [1.6 mM], reduced nicotinamide adenine dinucleotide (NADH) [0.7 mM], 2-phosphoglycerate (2PG) [2 mM], MgSO₄ [25 mM], KCl [100 mM], HEPES [50 mM, pH 7.5], Pluronic F108 [70 µM], and MOPS [50 mM]. All assays contained a positive control well with 500 ng of the His-Eno in solution with SiMNPs [100 µg], and negative control with the reaction mixture and SiMNPs [100 µg] minus enolase. The enolase conjugated SiMNPs were added to start the reactions. One unit will convert approximately 1.0 µmole of 2PG per minute.



The next set of experiments used the sequential reaction of His-Eno1C and His-PK co-tethered to SiMNPs. Everything from the above assay stayed the same, except commercial PK was removed and the SiMNPs conjugated with both His-Eno1C and His-PK were added instead. Positive controls used 250 ng of His-PK and 750 ng of His-Eno in solution with SiMNPs [100 µg]. The PGM assays used SiMNPs conjugated with His-Eno1C, His-PK and His-Luc. PGM is upstream of enolase in the glycolysis pathway and therefore uses the same reaction mixture as enolase, except 3-phosphoglycerate (3PG) [2 mM] was added instead of 2PG. The detection strategy used luminescence instead of absorbance through the

introduction of firefly luciferase, a bioluminescent enzyme which requires ATP from the PK reaction and exogenous luciferin [1.3 mM]. This was used to show that our strategy can work under different detection modalities for use in a PoCT device, where an exogenous excitation source is not ideal. His-PGM was added, in solution, in varying concentrations [0.6, 1.2, 2.4, 4.8, 9.6, 19, 38 ng/ml] to start the reactions. Luminescence is given in relative light units (RLU) and is dependent on the amount of ATP produced.



Each assay was performed at least three times with multiple protein preparations to demonstrate reproducibility. We calculated specific activity, in the case of single enzyme conjugates (units per amount of protein bound), and relative activity, for multiple enzyme conjugates (units per total amount of protein bound). All assays were carried out at RT.

4.2.5: Statistical Analysis. Statistical analysis was performed using the student *t* test for two samples assuming unequal variance to assess significance. Bar plots are presented as average \pm standard deviation using Microsoft Excel Software. Box plots are presented as the mean (-) and median (mid line) including the 1st (x), 5th (dashed bar), 25th (upper box), 75th (lower box), 95th (dashed bar) and 99th (x) percentiles, using Origin Lab Software.

4.3 Results

4.3.1: Protein Engineering and Optimization of Enolase.

Eno4 constructs showed good protein expression in the FreeStyle cell system; however, the purified enzyme displayed little to no activity, irrelevant of which terminus the His-tag was placed (data not shown). Both Eno1C and Eno1N were successfully expressed and retained functionality in solution (i.e. in buffer). Immunoblots of the purified enzymes revealed His-tagged proteins at 49 kD for both constructs (Fig. 4.2 A) compared to native enolase at 47 kD. Specific activity was analyzed between the two and was statistically higher ($p < 0.01$) for Eno1C when compared to Eno1N in-solution (Fig. 4.2 B). Eno1C had an average of 46% ($p < 0.01$) higher expression than Eno1N with purities ranging from 61% \pm 8 pure (Eno1N) to 78% \pm 7 pure (Eno1C). Kinetic assays were performed in-solution and analyzed using non-linear regression with fitting to R^2 . Eno1N yielded a k_{cat} of 13 ± 3.5 units/mg and a K_M of 0.6 ± 0.23 mM, while Eno1C had a k_{cat} of 31 ± 7 units/mg and a K_M of 1.3 ± 0.45 mM.

4.3.2: Enolase Immobilization to SiMNPs

Eno1N and Eno1C had similar binding characteristics whether with COOH-tethering or through Ni-NTA, with 77-85% immobilized to the surface. Enolase retained functionality when tethered to SiMNPs with both COOH and NTA coatings (Fig. 4.3). Eno1N had lower activity ($p < 0.01$) than Eno1C when bound to SiMNPs with both COOH and NTA coatings. However, the Ni-NTA coated surface had a statistically higher activity ($p < 0.01$) with both Eno1N and Eno1C compared to the COOH coating.

4.3.3: Pyruvate Kinase and Enolase Co-immobilization and Sequential Reactions.

Binding of PK has been optimized and shown to be most active with a His-tag on its N-terminus (data not shown). When both His-PK and Eno1C were co-immobilized on SiMNPs there was 60-70%

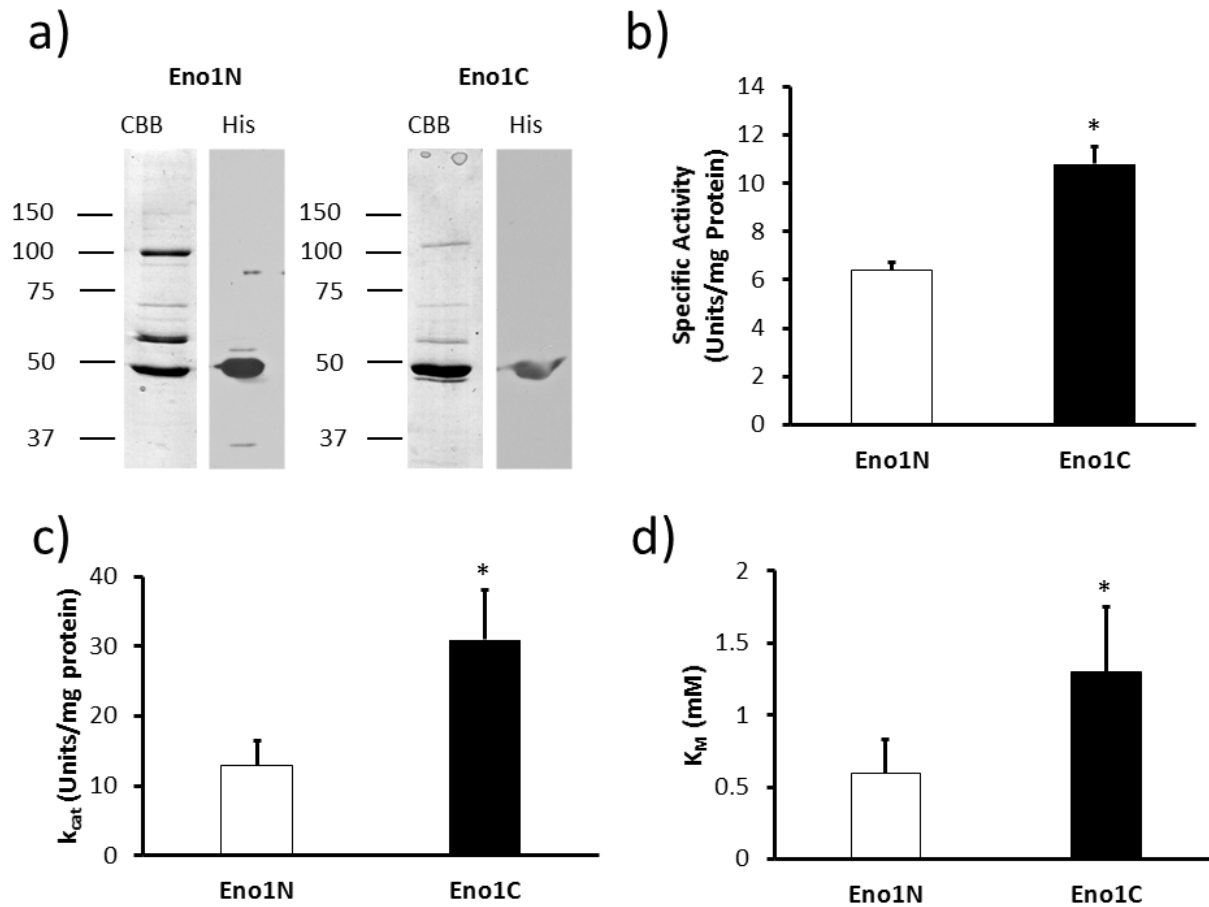


Figure 4.2: Expression and kinetics of His-tagged enolase constructs (Eno1N and Eno1C). (a) Expression after purification of Eno1N and Eno1C (~49 kD) using SDS-PAGE with a Coomassie brilliant blue (CBB) stained gel and an immunoblot showing detection of the anti-His (His). We compare the (b) in-solution specific activity (units/mg protein), (c) k_{cat} (units/mg protein) and d) K_M (mM) of Eno1N versus Eno1C. (n = 9, *p < 0.01).

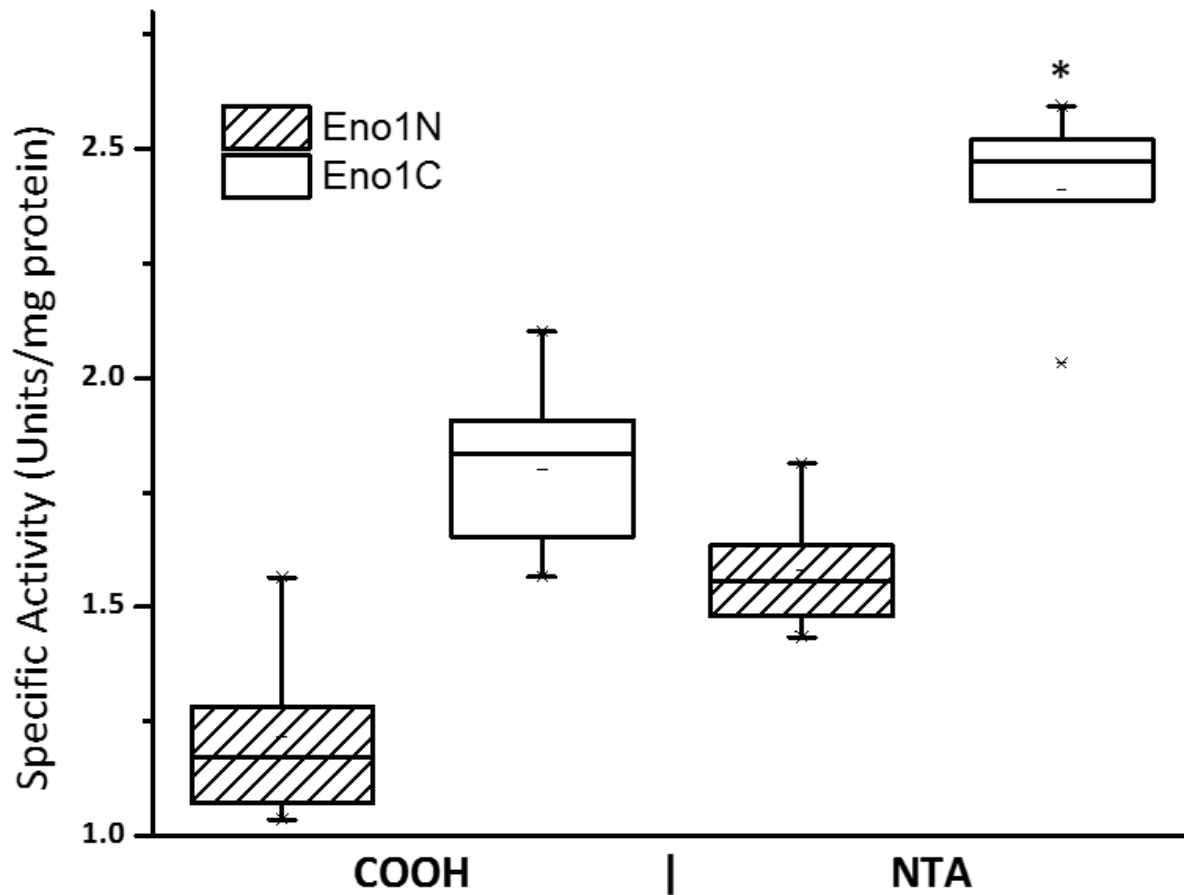


Figure 4.3: Specific activity of Eno1N and Eno1C bound to SiMNPs via chemical (COOH) or oriented (NTA) immobilization techniques. It is interesting to note that NTA binding was always higher than COOH binding (n = 9, *p < 0.01).

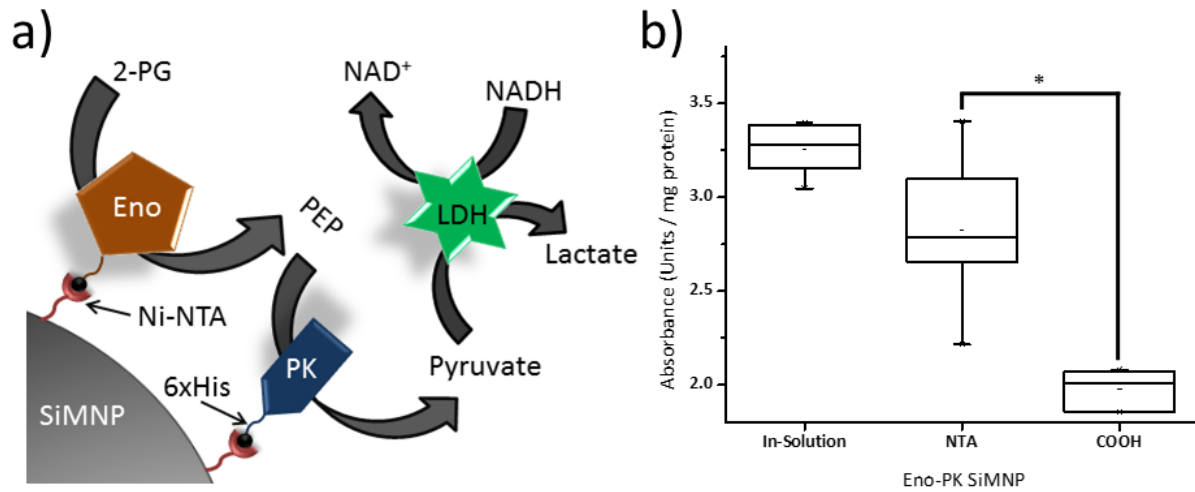


Figure 4.4: Oriented immobilization of Eno1C and His-PK. (a) Schematic of the sequential reaction of the co-immobilized enzymes on a SiMNP coated with Ni-NTA. (b) The relative activity (units/mg protein) of Eno1C and His-PK in-solution, co-immobilized using oriented immobilization (NTA), and co-immobilized using chemical binding (COOH) ($n = 6$, $*p < 0.01$).

adsorption. A schematic for the sequential reaction is given in Figure 4.4 A, and the equation is presented in the Materials and Methods section. Figure 4.4 B shows the comparison between the enzymatic reactions in solution not attached to SiMNPs (i.e. freely diffusing enzymes), and with conjugated SiMNPs via COOH or through Ni-NTA. As before, the Ni-NTA surface showed higher activity ($p < 0.01$) when compared to the COOH surface. In the case of oriented immobilization, comparing the bound enzyme activity (2.8 ± 0.4 units/mg protein) with those that were in-solution (3.3 ± 0.1 units/mg protein) gave $86\% \pm 13$ retention of activity.

4.3.4: Detection of Phosphoglycerate Mutase Utilizing Tethered Pyruvate Kinase and Enolase

Sequential Reactions.

PGM was engineered to include a His-tag on the N-terminus. Commercially available PGM is unstable and activity decays rapidly when diluted to low concentrations (ng/ml), whereas fresh His-PGM is more stable and maintains a high degree of activity. The SiMNPs are saturated with His-Eno or His-PK, likely forming multilayers (see Chapter 2), and therefore Ni-NTA binding sites are unavailable for His-PGM to bind. Furthermore, if binding did occur, His-PGM would show decreased activity, yielding a lower error in our assay. To verify that our system could detect different amounts of PGM we introduced varying concentrations of His-PGM, in solution, and collected the luminescent data. As shown in Figure 4.5, we could detect His-PGM down to 0.6 ng/ml. Although the pathological range for PGM is unknown, this value is consistent with the lower range of most enzyme biomarkers, such as NSE²⁹.

4.4 Discussion

We first compared the activities of Eno4, the isozyme found in sperm, and Eno1, a common somatic isozyme. In contrast to our studies involving tethering of other glycolytic enzymes of sperm^{18, 19},

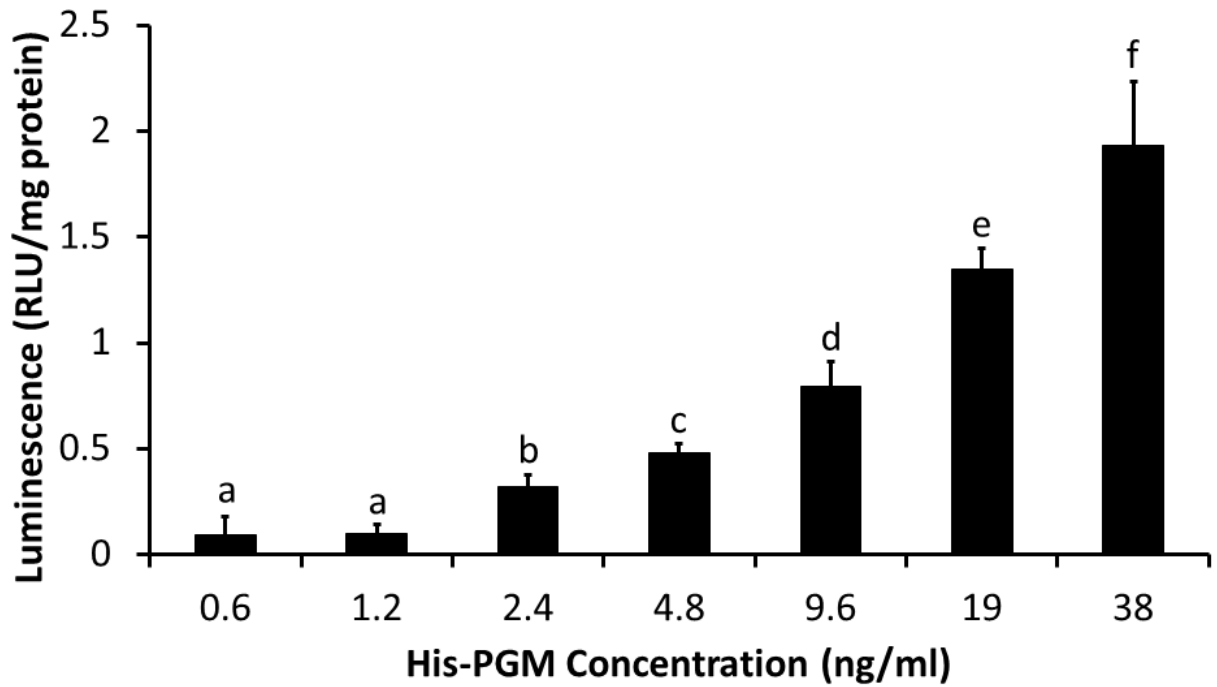


Figure 4.5: Varying concentrations of His-PGM detected via luminescence using oriented co-immobilization of Eno1C and His-PK. Final activity was measured by subtracting the activity with substrate from the activity without substrate to remove background noise (n = 3, dissimilar letters denote significance at $p < 0.01$).

expression and subsequent tethering of Eno4 did not result in an active enzyme. There was no expression for the N-terminal construct and the C-terminal construct had very low expression with negligible activity, possibly due to the His-tag interfering with needed conformational changes or blocking of the catalytic domain. As shown in Figure 4.2 we successfully expressed Eno1, both with a C and N term His-tag, and maintained a high level of in-solution activity. We have demonstrated the importance of how and where to target immobilization of an enzyme to a surface for optimal enzymatic activity. Creating enolase constructs with either a His-tag on the N- or C-terminus resulted in a statistically significant difference in specific activity in-solution. Interestingly, this was also the first of 10 glycolytic enzymes which had a preference for tethering to the C versus the N terminus. In most of our tethering strategies we compare somatic isoforms of the enzymes to the GCS isoforms, in which the N-terminus was the hypothesized tethering domain. Tethered enolase does not appear to follow this pattern, with the somatic isoform, Eno1, tethered via the C terminus, producing the best activity.

Even though Eno1N was less active in-solution, we wanted to assess if immobilization of the enzyme would rescue some of the activity, since all of the other enzymes our laboratory has constructed showed higher activity when tethered via the N-terminus^{18, 19}. As shown in Figure 4.3, the Eno1N enzyme activity was not rescued, but it still remained active. The more striking finding was the increased activity of enolase when it underwent oriented immobilization (NTA) compared to the chemical technique (COOH). The results from these assays demonstrate that oriented immobilization through the C-terminus on enolase yielded the highest activity out of all the strategies we evaluated. Although the Eno1C presented here yielded higher enzymatic activity, further optimization may be possible via alterations in linker lengths between the His-tag and the enzyme²⁰, as well as a more idealized placement of the His-tag on the enzyme.

To detect PGM, we next co-immobilized Eno1C and His-PK. His-PK was constructed and analyzed previous to these experiments (data not shown). His-PK specific activity (units/mg protein) showed

about triple the activity of Eno1C, potentially making Eno1C the rate limiting step in the reaction. A 3:1 ratio of Eno1C:His-PK was chosen to equalize the activities. As shown in Figure 4.4, the binding technique again made a significant difference in activity. While this was to be expected, what was surprising was the amount of enzyme activity retained (~86%) with oriented immobilization compared to in-solution. This higher than anticipated activity could result from increased proximity of Eno1C to His-PK, as well as increased local concentration of the enzymes, since the SiMNPs were observed to slowly settle to the bottom in between orbital shaking cycles.

The coupled reaction of tethered His-PK, Eno1C and His-Luc was then utilized in an analyte detection/quantification application to detect His-PGM. An increase in PGM blood levels has been reported after neural injury and acute myocardial infarction, therefore we sought to test our assay as a potential diagnostic platform technology for PGM. Enzymatic reactions have been used to detect PGM activity in clinical trials^{32, 33, 108}. However, the use of tethered enzymes offers a way to incorporate the coupled reactions into a device that does not need an excitation source and can be miniaturized yet still maintain high sensitivity. The ability to tether the enzymes enables spatial control and higher localized concentrations of the enzyme. We show in Figure 4.5 that the sensitivity was not lost when tethering Eno1C, His-PK and His-Luc to SiMNPs, enabling us to detect changes in His-PGM concentrations down to 0.6 ng/ml.

4.5 Conclusions

This study represents an exciting first step in the development of a novel PoCT device for rapid detection of blood biomarkers via tethered enzymes. With our current tethered enzymes we can detect two stroke biomarkers, PGM and NSE, in a 96-well plate. Using micro-channel chip designs, simultaneous biomarker recognition could take place in a hand-held apparatus. Reaction wells in micro-channels could be pre-loaded with tethered enzymes lyophilized to improve shelf life. This would allow the chip to be

self-sufficient (only a blood sample would be needed to reconstitute and start the reactions). The detection output could be varied depending on the specific application, including absorbance by adding lactate dehydrogenase (LDH) and reduced nicotinamide adenine dinucleotide (NADH), luminescence by adding firefly luciferase and luciferin, or color through the use of horseradish peroxidase and 3,3',5,5'-tetramethylbenzidine (TMB). This platform technology fills a much needed role in diagnosing time sensitive pathologies at the bed-side or on-the-scene by enabling device miniaturization to PoCT and utilizing rapid signal output through enzymatic reactions.

CHAPTER 5

MICROFLUIDIC PLATFORM FOR POINT-OF-CARE DETECTION OF STROKE BIOMARKER, NEURON-SPECIFIC ENOLASE[‡]

5.1 Introduction

Stroke is one of the leading causes of mortality and long-term disability in the US, yet current practice lacks the ability for prompt diagnosis within the 3 hour window in which treatment can be most effectively administered. Every year, 795,000 people in the United States suffer from stroke, and 279,000 of those result in death¹²⁴. Diagnosis relies on the expertise of neurologists who can interpret clinical signs and results of advanced imaging tests (e.g. CT/MRI)²⁷. During this process, patients must follow a labyrinth of mental and physical tasks to rule out stroke mimics, such as transient ischemic attacks, migraines, epilepsy, electrolyte abnormalities, and mass lesions²⁵. It must also be determined whether the stroke is ischemic, which accounts for 87% of strokes¹²⁴, or hemorrhagic; as the thrombolytic treatment for ischemic stroke, tissue plasminogen activator (TPA), is contraindicated in cases of hemorrhagic stroke. Optimally, TPA must be given within a 3 hour window to be effective, thus prompt diagnosis is imperative²⁶. In addition to the time it takes for the patient/family to recognize and diagnose the problem, further delays are experienced in getting the patient to a facility that can make a diagnosis; 77% of counties within the US do not have a hospital with neurological services²⁴. All of these issues leads to an inherent problem with the current diagnostic paradigm which results in less than 5% of patients receiving necessary treatment¹²⁴.

The ability to detect a biomarker from a drop of blood can give insight into pathological conditions or, depending on the specificity of the biomarker, a definitive diagnosis. Because of the clinical need, a great many potential biomarkers for stroke have been identified^{28, 31}. One such biomarker, neuron

[‡] Modified from Lata JP et. al. Manuscript in preparation for publication.

specific enolase (NSE), which is released after neuronal cell death^{30, 125}, has proven to be one of the leading markers for stroke and has gained credence in distinguishing strokes from mimics. Making point-of-care testing (PoCT) devices that can identify stroke biomarkers is still a relatively new technology, and although there has been a great deal of research interest, it has yet to make an impact in a clinical setting¹²⁶.

PoCT devices for biomarker detection faces several challenges. Biomarkers of different classes often require different detection approaches. Assays for biomarkers can be time consuming; antibody-based detection methods such as enzyme-linked immunosorbent assays (ELISA) can take several hours³⁶. Lastly, instrumentation for detection is not easily portable and detection is costly. However, if these obstacles are overcome PoCT technology presents numerous advantages, particularly in the case of time sensitive pathologies. As stated previously, the current diagnostic methodology is very time consuming and expensive. PoCT devices would revolutionize the diagnostic paradigm by adding a step before the patient arrives to the hospital. While in transit, or at the scene, a paramedic can draw blood and run it through a device which will provide quantitative insights as to whether a stroke occurred, and possibly the type/size of stroke. In the case of an ischemic stroke the patient can immediately receive TPA; in the case of a small stroke, and possibly hemorrhagic strokes, the patient can immediately go for MRI, skipping both a CT scan and the need for a neurologist's assessment. PoCT technology could take advantage of use of a microfluidic system, such as: high portability, increased sensitivity, minute reagent amounts, small blood sample sizes, reduced manufacturing cost, high multiplex capability, and operation simplicity.

There are many types of devices being designed to detect biomarkers^{109, 127-134}, but one alternative technology in particular is being developed for diagnosis of multiple biomarkers and addresses similar challenges. The Triage system from Alere/Biosite offers a single use chip-based diagnostic assay for multiple pathologies including the diagnostic Triage® Stroke Panel¹³⁵. This system can detect four stroke

biomarkers using immunoassay techniques. However, the detection of biomarker panels is based on a fluorescent signal requiring a sophisticated operation process, large readout equipment, and high energy demands. This technology has been through clinical trials, but has yet to be implemented in clinical practice.

We propose a novel PoCT platform that uses coupled enzymatic reactions in microfluidic channels for rapid detection of the stroke biomarker, NSE, in human serum. By using oriented immobilization, we have stably tethered functional enzymes to nanoparticles and used these conjugates to perform coupled reactions to detect NSE as well as other stroke biomarkers not discussed here (see Chapters 3 and 4). Enzyme tethering is based on the Travis Lab's use of biomimicry of the sperm flagellum to immobilize enzymes in an oriented fashion on various inorganic surfaces^{16, 18, 19}, in this case silica nanoparticles (NPs). This strategy for tethering the enzymes confers benefits in activity and stability versus chemical or non-specific methods.

Here, we seek to integrate these enzyme-NP conjugates into a multichannel microfluidic platform. Tethered enzymes in a microfluidic-based PoCT device would have multiple advantages over current antibody-based approaches. These advantages include: 1) speed - enzymatic reactions occur thousands of times faster than antibody-antigen interactions; 2) luminescence-based readout - enables standalone, highly portable devices that do not require bulky excitation elements (such as for fluorescence or absorbance); 3) sensitivity - enzymatic reactions facilitate signal amplification at the steps of both detection and readout; 4) low cost of fabrication - NPs and microfluidic channels (microchannels) are made from inexpensive materials and can easily be mass produced; 5) small sample size - the rapid enzymatic detection with the microchannel design only requires nanoliter amounts of serum per reaction; 6) accurate quantification - different amounts of the same NP-tethered enzymes can be placed in adjacent channels, providing variable range sensitivity for each biomarker tested; 7) multiplex capability - coupled biochemical reactions can detect multiple biomarkers through a spatially-defined

luminescence readout; and 8) robust and portable - the chip/reader system as a whole could be small and portable due to the low energy demands. Our specific reaction will detect enolase, which is the ninth glycolytic enzyme and can be detected with a luminescence-based readout through coupled reactions with NP-tethered pyruvate kinase (PK) and firefly luciferase (Luc). Earlier we presented our findings of clinical trials for this assay to detect NSE levels in a 96-well plate (see Chapter 3).

To minimize required sample sizes and enhance portability, our tethered enzyme detection strategy is integrated into a multichannel microfluidic platform. This allows us to minimize the reaction volume and maintain a high degree of sensitivity. Transitioning from 96 well plates to a microfluidic card platform is a significant step in enabling the tethered enzyme technology to be used by paramedics as a PoCT device in a variety of field settings. NP-enzyme conjugates are concentrated within a reaction chamber in the microchannel through lyophilization, concentrating and restricting signal output to that one region. A multichannel design allows for a single input of serum to give multiple readouts, each with a positive control, negative control and test channel to rigorously detect NSE levels in human serum at physiological and pathological levels (Fig. 5.1).

5.2 Materials and Methods

All materials and reagents were purchased from Sigma-Aldrich (MO, USA) or ThermoFisher Scientific (MA, USA) unless otherwise stated.

5.2.1: Enzyme Nanoparticle Conjugation. Recombinant PK and Luc were generated and their identity, relative purity, and activities verified using previous methods (see Chapter 3). Enzymes were engineered to include a hexahistidine tag (His-tag) for enzyme purification and a silica binding tag (Si4-tag) for silica

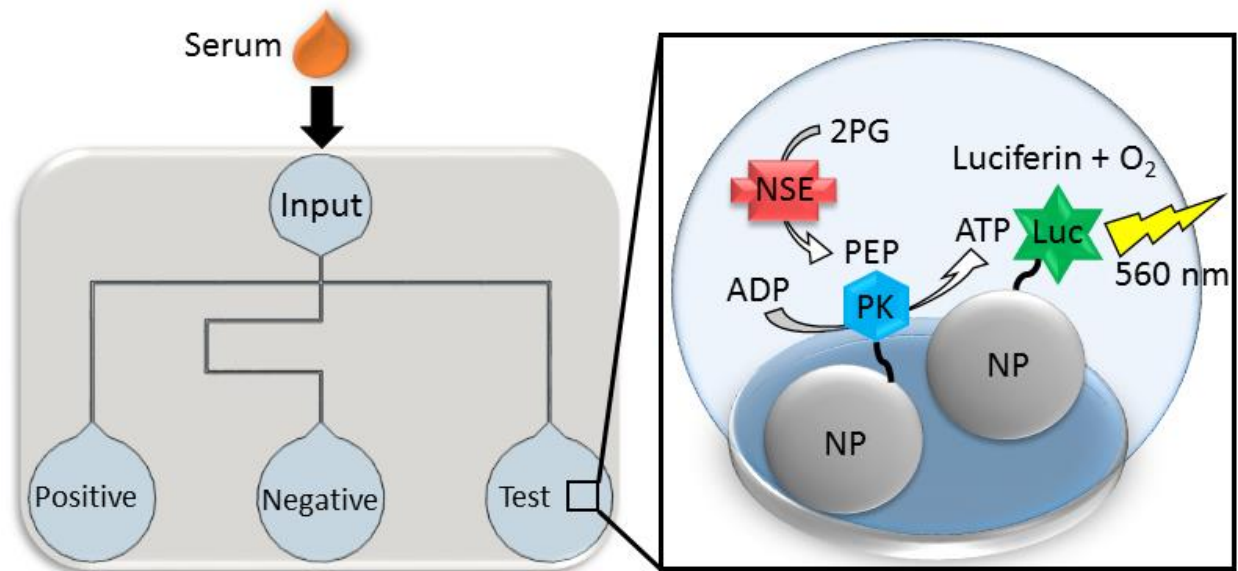
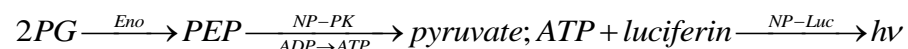


Figure 5.1: Schematic representation of the microfluidic chip and the tethered enzyme reaction for NSE detection. Serum sample is introduced into the inlet of the microfluidic chip and travels to three chambers via negative pressure. The three chambers include a positive control, negative control and test chamber where lyophilized reagents are reconstituted by the serum sample. Each lyophilized mix contain NP tethered enzymes, PK and Luc, and all cofactors, substrates and reagents needed for the sequential reaction to translate the concentration of NSE into light intensity ($\lambda= 560 \text{ nm}$). A detector above the chambers detects the amount of light which is used to quantify the amount of NSE in the sample.

NP tethering. Enzymes were tethered separately to 500 nm silica NPs (Spherotech Inc., IL), washed three times with low salt sodium phosphate buffer (NPB) by centrifugation, and then mixed together.

5.2.2: Enzyme Activity Assay. For this study we used α -enolase (Eno) instead of NSE, as commercially available NSE does not have stable activity (data not shown). The detection of Eno utilized the coupled reaction of PK and Luc tethered to silica NPs. The forward reaction for detection is:



All reactions were optimized to contain the following master mix concentrations: luciferin [20 mM], ADP [20 mM], MgCl₂ [10 mM], KCl [2 mM], HEPES [50 mM], Pluronic F108 [48 mg/ml]. Positive control and test reactions included 2PG [9 mM]. Positive control reactions also contained frozen Eno [200 ng/ml]. Luminescent output from the reactions was read with a luminescent plate reader (Infinite M200 Pro, Tecan). This was modified with a custom 3D-printed plate (Fig. 5.2 A) prepared using a 3D Printer (da Vinci 1.0, XYZ Printing), designed to elevate the microfluidic chips to be in close proximity to the detector unit. Luminescence was integrated for 1 second every 30 seconds for up to 30 minutes. Each chip included a positive, test and negative channel and was independently tested at each concentration four times, yielding similar data trends.

5.2.3: Microfluidic Chip Designs. Microfluidic chips were designed and fabricated at the Cornell Nanofabrication Facilities (Ithaca, NY). SU-8 lithography was utilized to make 250 μm high structures using 2150 SU-8¹³⁶¹³⁶. Polydimethylsiloxane (PDMS) was molded over the SU-8 structures using a 20:1 PDMS and curing agent mass ratio, yielding sticky and pliable PDMS microfluidic chips. Each chip included a 2 mm wide inlet with 100 μm wide channels leading to three separate \varnothing 4 mm reaction chambers. Each reaction chamber represented either the test chamber, in which all reagents needed for the reaction are supplied except Eno (which would be supplied by the sample to be tested); the negative

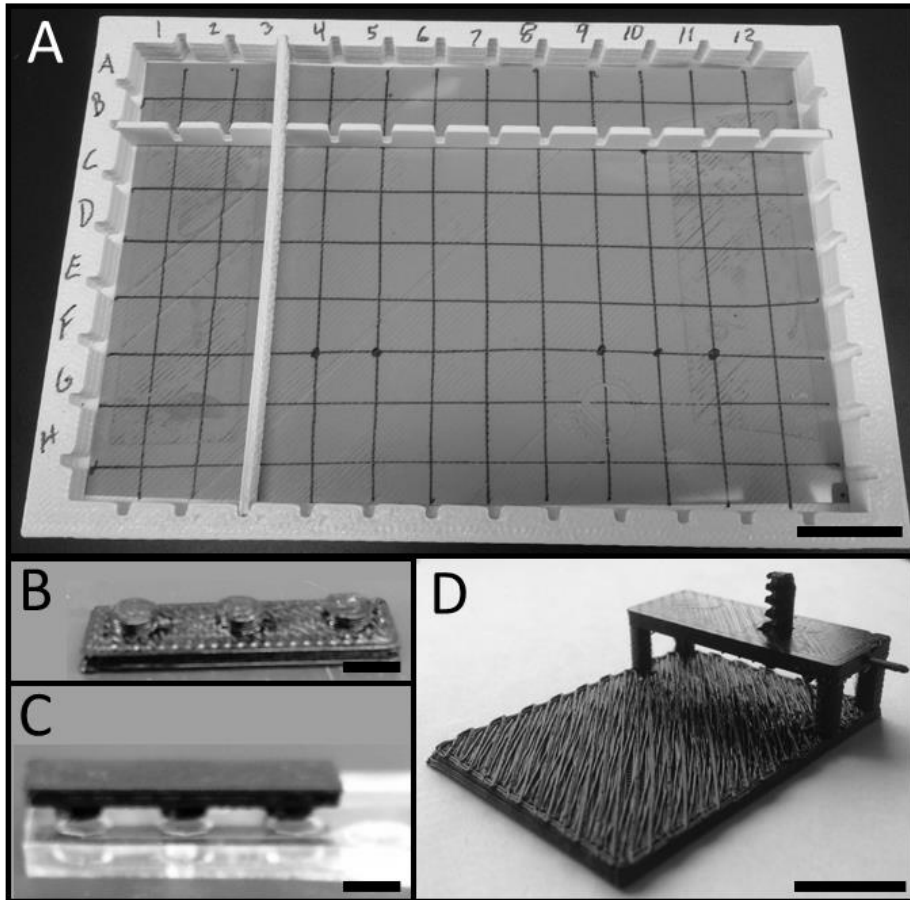


Figure 5.2: 3D printed apparatus for housing the microfluidic chips. We tested several designs with a goal of improving the signal output and reliability obtained using the microfluidic chips. The first is a 3D printed plate for use in a standard plate reader (panel **A**). The plate was designed to elevate the chips closer to the detectors and accurately position the chips so the chambers are aligned with the detector. The scale bar represents 20 mm. Two separate pieces were constructed to apply pressure to the microfluidic chips for the negative pressure pumping action. The first apparatus used a small three chamber pump (panel **B**) which was placed over the chambers (panel **C**) and simply pressed with a finger. Scale bars represent 4 mm. An alternative apparatus used a variable pump that included a bar with ridges (panel **D**) which was pressed over the pump chamber and held at a specific pressure using a needle. Scale bar represents 20 mm.

control, in which all reagents except 2PG are supplied, giving the background luminescence of the system; and the positive control, in which all reagents including 2PG and a high concentration of Eno are supplied to provide a standard for normalization between different samples and devices. Two different chip devices were used, which gave similar results, device A (Fig. 5.3 A) and device B (Fig. 5.3 B). Device B differed from device A through the use of an external negative pressure pump which was \varnothing 5 mm and 2 mm deep.

5.2.4: Loading and Cleaning the Chip. After the PDMS chip was cured and peeled off the SU-8 master wafer, it was placed on a -80 °C aluminum block. 8.4 μ l of the master mix was placed in each reaction chamber and froze within seconds. In the positive and test chambers 0.4 μ l of 2PG was added and allowed to freeze. Lastly, in the positive control chamber 2 μ l of enolase was placed on the frozen reaction mix and froze. This sequential freezing of reaction components prevented the reaction from initiating before the sample is added. The chips were then placed in a lyophilizer (FreeZone 2.5, Labconco) for 45 min until no liquid remained. After lyophilization, the chips were closed with a glass coverslip or microscope slide, which readily sealed with the sticky PDMS. Fluid flowed through both devices via negative pressure which was induced by positive pressure to either the reaction chamber in device A or the external pump in device B. Device A had a 3D printed plunger (Fig. 5.2 B&C) which was used to apply pressure on top of the pliable PDMS over the reaction chambers. Once pressure was applied the sample was loaded into the inlet and the plunger taken away, creating a vacuum that pulled the sample into the reaction chambers, completely filling them. Device B had the same premise, only the pressure was applied to the external pump with a different 3D printed plunger (Fig. 5.2 D) which gave just enough pressure to fill the chambers and not overflow into the pump. In both devices, enough sample was loaded to fill the reaction chambers and allow air to close off any back flow which would cause mixing between the chambers. After the chips were used for detection they were placed in a

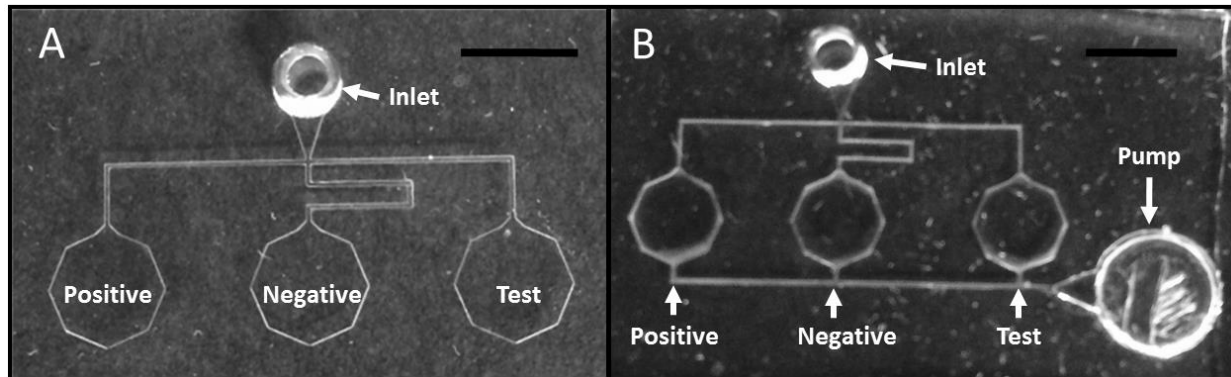


Figure 5.3: Microfluidic chip designs. SU-8 lithography and PDMS molding was used to make three chamber microfluidic chips including a single inlet that lead to a positive, negative and test chamber. Two different approaches were taken to introduce the flow via negative pressure, **(A)** pressure was applied to all three chambers and released once the sample was added, or **(B)** pressure was applied to an external larger fourth chamber (pump) and released after the sample was added. Both designs were adequate at rapidly filling the chambers simultaneously, however device B was less reliable due to the pump needing the exact same pressure each time, whereas device A was not so dependent upon the amount of pressure applied. Scale bars represent 4 mm.

mixture of ethanol, cleaning soap (Liqui-Nox, Alconox) and water then stirred for 4-8 hrs. The chips were then rinsed with DI water followed by MilliQ water and allowed to dry for continued use.

5.2.5: Statistics. All data were analyzed using Microsoft Excel and statistics were carried out using Pearson's correlation (CF) and Student's *t* test with unequal variance.

5.3 Results and Discussion

5.3.1: Miniaturization and lyophilization of enzymatic reaction.

In previous work (see Chapter 3), we developed our NSE reaction to work at volumes as low as 50 μ l. Here, we optimized the reaction conditions to work at \sim 2.5 μ l volumes. This required optimization for each reagent in the reaction mixture. Our foremost concern with the reaction focus on the cryoprotectant, sorbitol. At high concentrations, sorbitol does not lyophilize—instead becoming a dense gel—within the time frame needed to maintain enzymatic activity. In order to introduce this reaction into a microfluidic chip device we needed to look for a different cryoprotectant which would fully lyophilize to a powder allowing fluid flow. After comparing several cryoprotectants (Fig. 5.4), pluronic F108 was chosen. Pluronic not only proved to be a powerful cryoprotectant, but likely because of its dispersant properties, also enhanced the enzymatic activity yielding higher sensitivity in our reaction. Reactions were lyophilized and tested in a white 96-well plate prior to being introduced into the microfluidic platform. These reactions detected the differences between enolase concentrations within 10 minutes ranging from 0 to 100 ng/ml (Fig. 5.5). These data showed a CF of 0.99 and an 11-fold increase in activity when comparing 0 ng/ml with mid-level, 20 ng/ml Eno. We did note storage issues when moisture penetrated into the lyophilized mix, severely reducing activity. Therefore, rapidly sealing the microchannel chips after lyophilization was crucial.

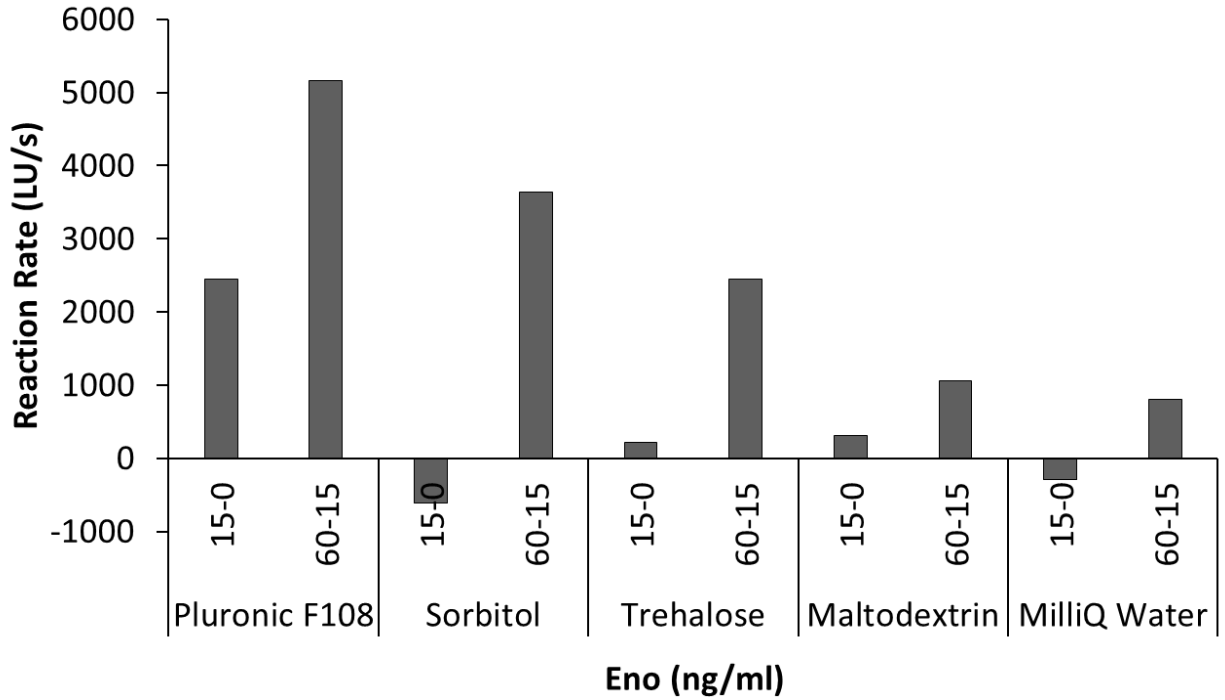


Figure 5.4: Reaction activity retention after lyophilization with different cryoprotectants. Five different cryoprotectants (Pluronic F108 [25 mg/ml], Sorbitol [0.3 M], Trehalose [25 mg/ml], and Maltodextrin [25 mg/ml]) were tested in a white 96-well plate with three Eno concentrations (0, 15, 60 ng/ml). After lyophilization, Eno was added to reconstitute the reactions and rates were taken over 15 minutes. The difference between each Eno concentration is presented as 15-0 (ng/ml) and 60-15 (ng/ml) which was used as the metric for retention of activity. Pluronic yielded the largest change in rate from 0 to 15 ng/ml and from 15 to 60 ng/ml with MilliQ water giving the least amount of change.

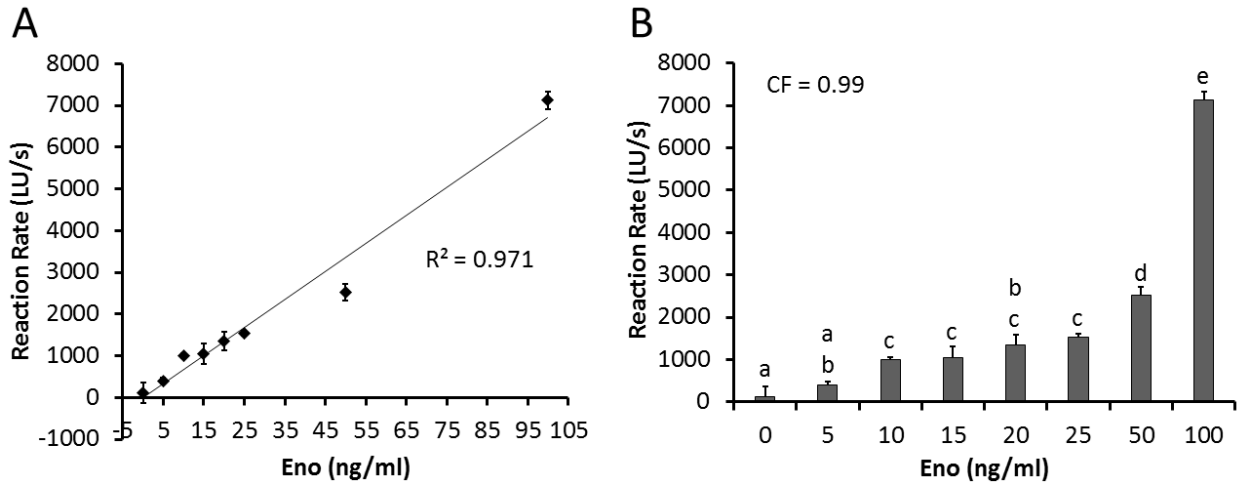


Figure 5.5: Detection of Eno at different concentrations. Reagents were lyophilized in a white 96 well plate and reconstituted with Eno at eight concentrations from 0 to 100 ng/ml. This experiment was done in triplicate which all fit on a single plate, therefore no positive or negative controls were needed to normalize the data sets. Rates of reaction were calculated after 10 minutes and plotted as (A) a scatter plot which shows standard deviation between the triplicates and a line of best fit, as well as (B) a bar graph displaying standard deviations, statistical significance and a CF of 0.99. These data show a high correlation between the reaction rate and the amount of Eno present in the sample. Comparisons among Eno concentrations were performed using a Student's *t* test with unequal variance (Excel); dissimilar letters denote significance at $p < 0.05$.

5.3.2: Optimizations of the microfluidic chip design and implementation.

The microfluidic chip was designed to be compatible with current plate readers. The reaction chambers were positioned at the same locations of three consecutive wells on a 96-well plate. In order to read the chips a custom 3D-printed plate was engineered which allowed the chips to be stuck through double-sided tape to specified locations analogous to the wells in a 96-well plate (Fig. 5.2). The custom plate was also elevated to hold the chips closer to the detector unit. This plate could fit four chip devices at once. The chips were tested with both the PDMS or the glass side toward the detector, with no difference in luminescence. For our use, it was simpler to keep the PDMS side up, toward the detector. The microfluidic chip went through rigorous performance testing and optimization. The depth and width of the channels were optimized to be large $250\ \mu\text{m} \times 100\ \mu\text{m}$ to allow for a greater volume of sample to rapidly reconstitute the reaction mixtures. For this reason we did not use passive flow through capillary action, as it was too slow to reconstitute the entire reaction, and the flow was too easy to be perturbed depending on various imperfections in the PDMS. Other designs included mixing elements such as pillars and shunts designed to optimize fluid flow in the reaction chambers (Fig. 5.6), however these designs did not notably improve the reactions and had poor reproducibility. We also tested the cross-talk between the reaction chambers, finding less than 2% cross-talk. Lastly, we tested a silicon reflective surface, a black plastic surface, and a white plastic surface behind the reactions to try and optimize the amount of light directed to the detector. The white surface yielded the optimal amount of light reflected back to the detector. Lyophilization of the reaction mixtures on the microfluidic chips was also tested with varying times and temperatures in order to keep optimal enzyme activity.

5.3.3: Detection of enolase in water and commercial human serum with microfluidic chip.

Device A (Fig. 5.3 A) was utilized for the detection of Eno. In device A, pressure is applied to the reaction chamber where there is lyophilized reaction mixture, whereas with device B the pressure is applied to

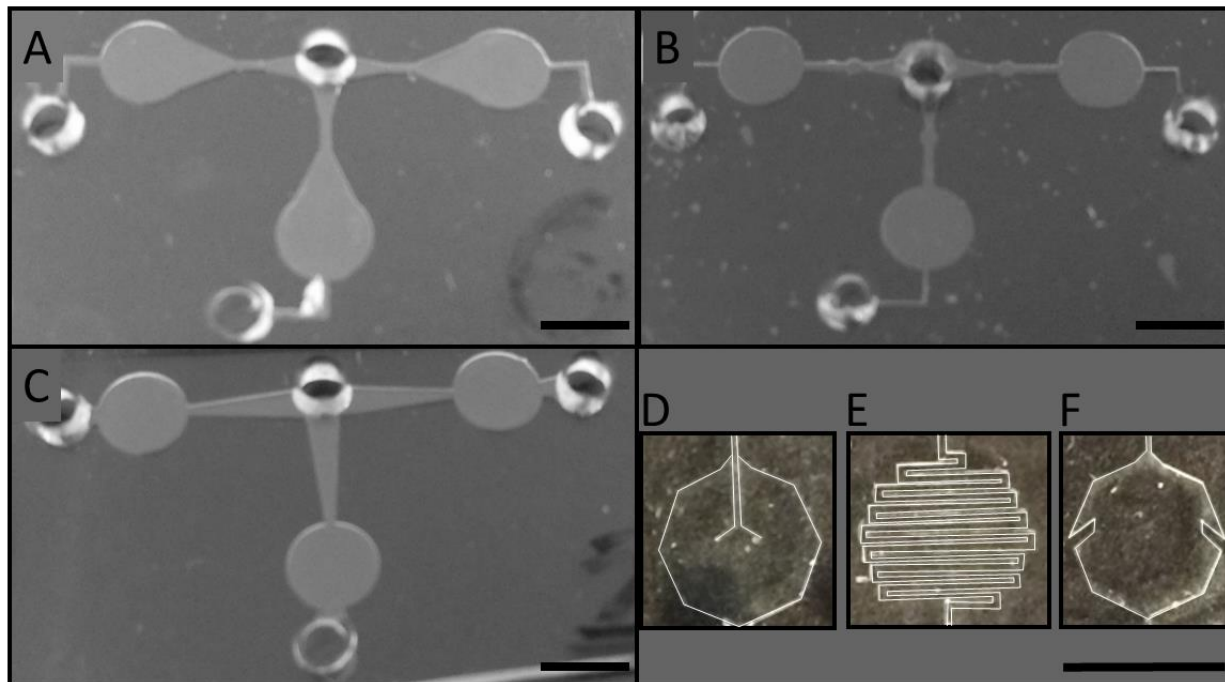


Figure 5.6: Photographs of different microchannel and chamber designs tested, but not used in our final chip design. The microchannels were positioned in a “T” shape to provide equal lengths of inlet to each chamber. We tested a two tapered channel design (panel **A**), a straight channel with small chambers for preloading of 2PG and/or Eno (panel **B**), and a long tapered channel design (panel **C**). The reaction chambers were also modified with a channel that applied the sample to the center of the chamber (panel **D**), a serpentine channel designed to help reconstitute the sample (panel **E**), and columns on the side to prevent liquid from following the walls and promote mixing (panel **F**). We determined that the modifications shown here did not provide better results and were excluded from our final design, which featured simple straight channels and open reaction chambers as shown in Figure 5.3. Scale bars represent 4 mm.

an external pump preventing any possible damage to the reaction. In practice, device B was slightly less consistent at obtaining the exact same volume of sample in the reaction chambers compared to device A. Further optimization of device B should yield a better second generation device. Eight devices, each including the three reaction chambers, were lyophilized at the same time. Four devices underwent detection while the other four were placed into a -80 °C freezer to be used after the first set. Eno samples were diluted with water just before they were placed in the inlet of the chip. Each chip included a positive control chamber, a negative control chamber and a test chamber. A positive control chamber is needed to normalize any variations in luciferase activity between experiments. The negative control chamber included everything in the reaction, excluding the initiating substrate (2PG), and is subtracted from the test and positive control chambers.

Eight concentrations of Eno [0, 5, 10, 15, 20, 25, 50, 100 ng/ml] were evaluated both at physiological (< 10 ng/ml) and pathological levels (> 10 ng/ml) in water (Fig. 5.7). This was done with 4 replicates of each concentration using differing enzyme-NP batches, and master mixes. Data shown in figure 5.7 are representative of the four replicates (Fig. 5.8). Increased luminescence was noted at higher Eno concentrations after 10 minutes of detection. Data revealed that the assay could differentiate at least 5 ng/ml differences in concentration with a CF of 0.98. Looking at a comparison from 0 ng/ml to mid-level, 20 ng/ml Eno we saw a 1.7 fold increase in activity. Next we repeated these concentration tests using commercial human serum instead of water. The results were less dramatic; however, the differences in concentration were still detectable with a correlation factor of 0.93 (Fig. 5.9 and 5.10). There was a 2.9 fold increase in activity when comparing 5 ng/ml and 25 ng/ml Eno. For both microchannel results using water and serum the signal is very low at Eno concentrations below 25 ng/ml and are within error, showing no statistically significant differences. However, the trends show much promise for this first generation device and with optimization of a custom detection apparatus to collect all photons being diffused elsewhere the sensitivity should improve to the level we get with a 96-well plate (Fig. 5.5).

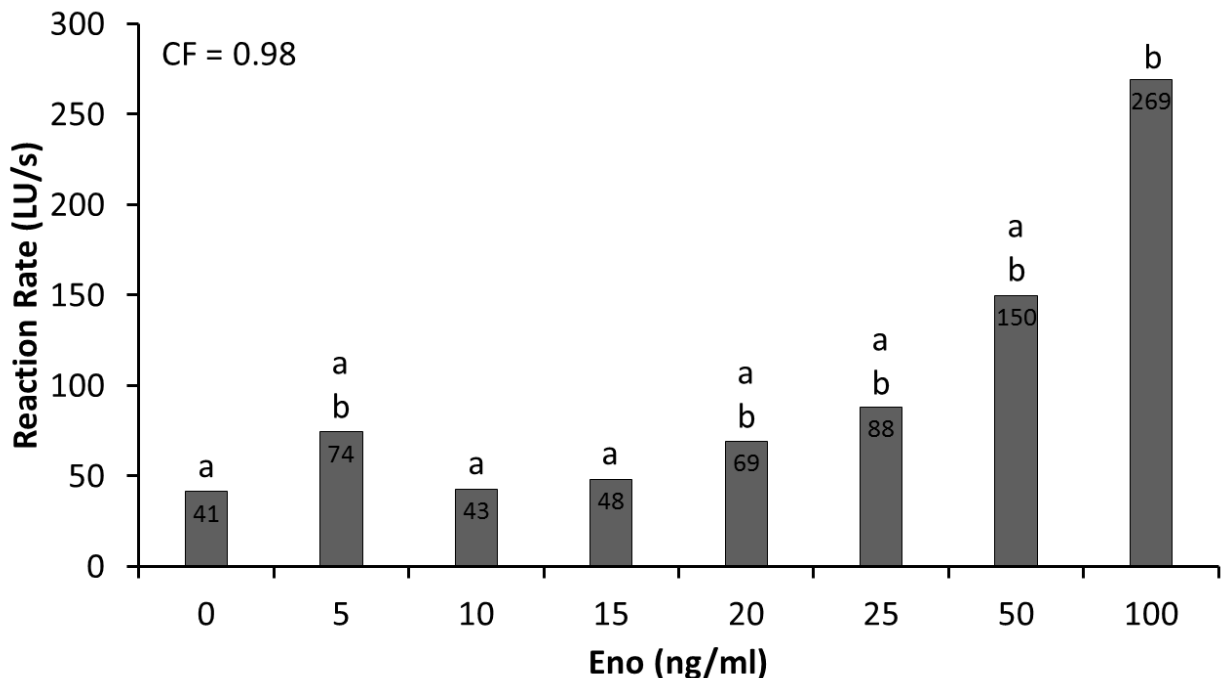


Figure 5.7: Microfluidic chip utilized to detect Eno diluted in water from 0-100 ng/ml. Eight concentrations of Eno were introduced into individual chips and luminescence collected over 10 minutes. Slope calculations were used to get the rate of reactions including both positive and negative control data to normalize data sets. There was an apparent increasing trend in reaction rate with Eno concentration, yielding a CF of 0.98. These data represent a single representative replicate for Eno detection in water, the statistical values come from all four replicates which can be found in Figure 5.8. Comparisons among Eno concentrations were performed using a Student's *t* test with unequal variance (Excel); dissimilar letters denotes significance at $p < 0.05$.

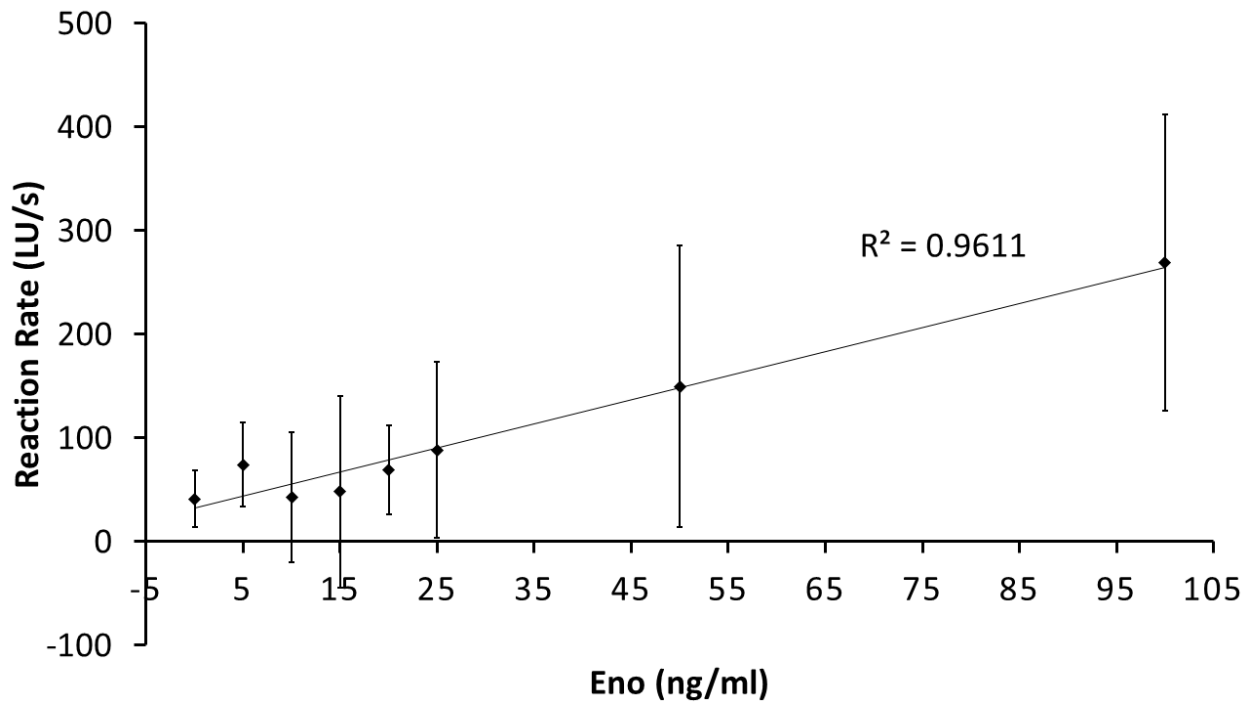


Figure 5.8: Microfluidic chip utilized to detect Eno diluted in water from 0-100 ng/ml. These data include all four replicates from figure 5.7. Error was calculated as standard deviation and a line of best fit is displayed. There exists an increasing trend; however, at low concentrations of Eno the error shrouds any significance.

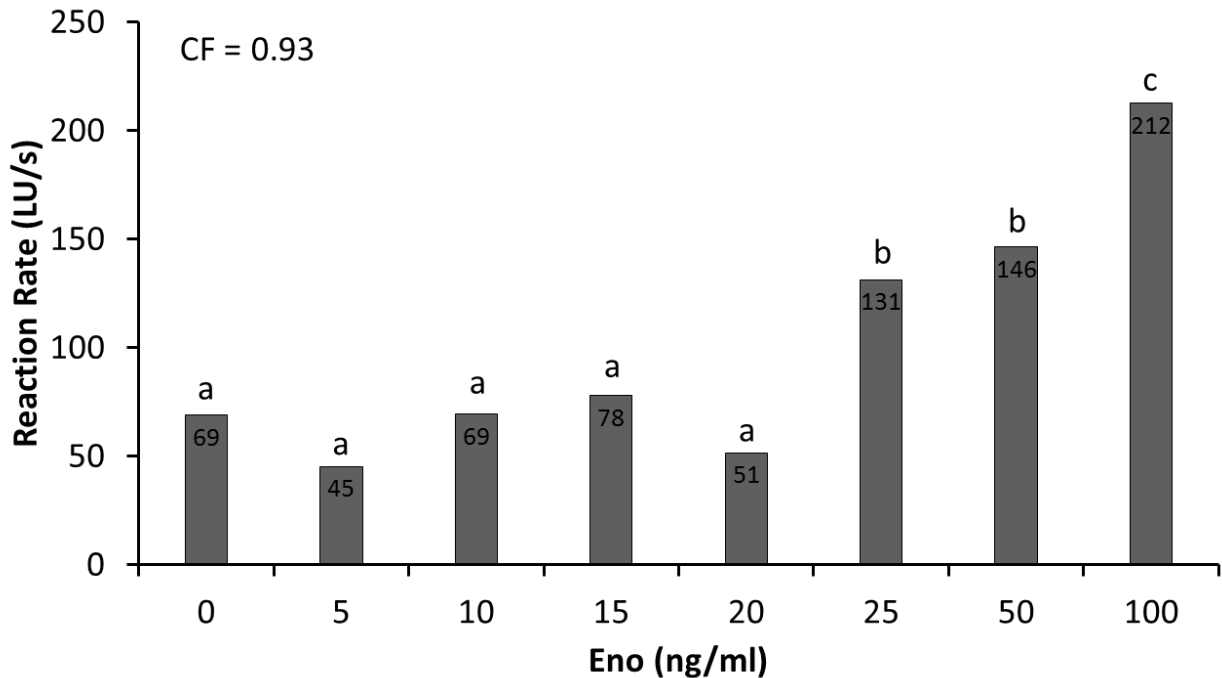


Figure 5.9: Microfluidic chip utilized to detect Eno in commercial human serum from 0-100 ng/ml.

Eight concentrations of Eno were introduced into individual chips and luminescence collected over 30 minutes. It took 10 minutes for the serum to completely reconstitute the lyophilized reagents, thus reaction rates were taken after the initial 10 minutes, which including both positive and negative controls. As in Figure 5.7, there appeared to be an increasing trend in reaction rate with Eno concentration, having a CF of 0.93. These data represent a single representative replicate for Eno detection in serum, the statistical values come from all four replicates which can be found in Figure 5.10. Comparisons among Eno concentrations were performed using a Student's *t* test with unequal variance (Excel); dissimilar letters denotes significance at $p < 0.05$.

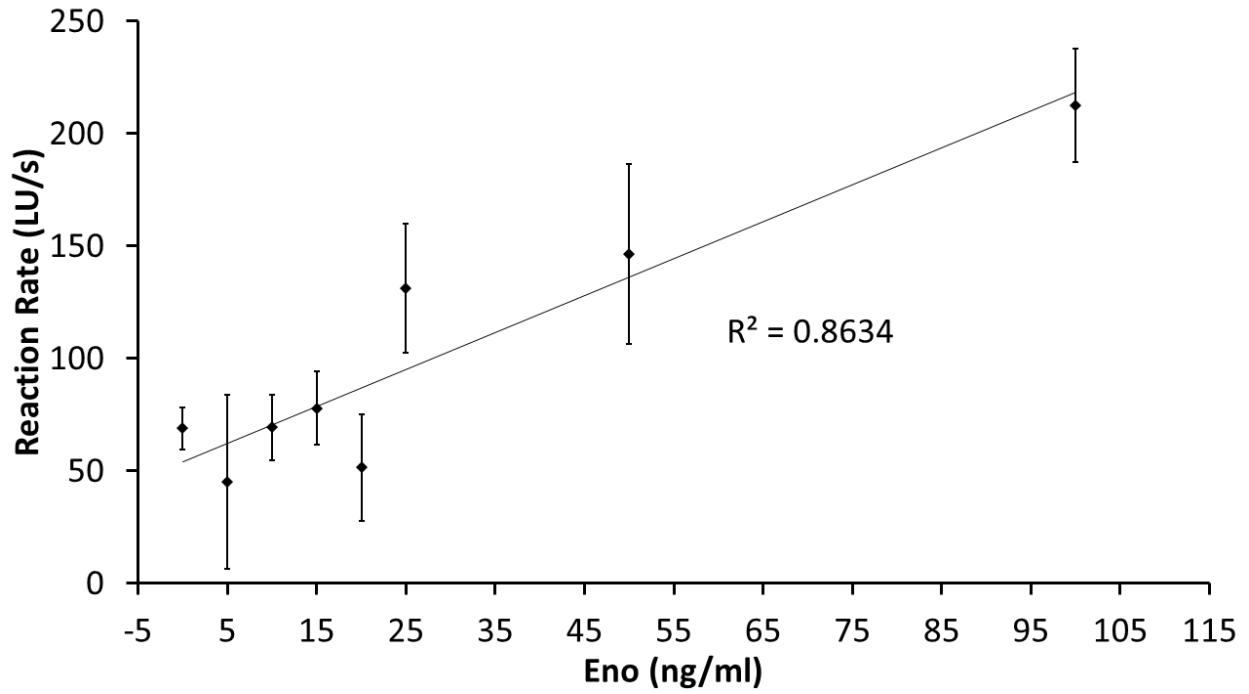


Figure 5.10: Microfluidic chip utilized to detect Eno in commercial human serum from 0-100 ng/ml.

These data include all four replicates from figure 5.9. Error was calculated as standard deviation and a line of best fit is displayed. There exists an increasing trend, however the error shrouds any statistical significance.

5.4 Conclusions

In conclusion, we have described a PoCT platform which utilized microfluidic chips for the detection of NSE biomarker for stroke diagnosis. Optimization of the 2.5 μ l tethered enzyme reaction gave statistically significant detection capabilities from 0-100 ng/ml Eno in a 96-well plate. The fabrication of microfluidic chips allowed for a single inlet which lead to 3 chambers comprising a positive, negative and test chamber. We obtained results for the tethered reaction operating inside the chips with both water and serum samples at Eno concentrations from 0 to 100 ng/ml. Increasing trends with correlation factors of 0.98 and 0.93 respectively, were observed although there were no statistical significance between each individual concentration. While there is still room for optimization, as the error for reproducibility is rather high, it is a first step in creating the first tethered enzyme based PoCT device for diagnostic applications.

CHAPTER 6

CONCLUSIONS AND FUTURE DIRECTIONS

Engineering enzymes through rational design to tether them to a surface and retain their function is a complicated process requiring the creation of multiple constructs for each enzyme to verify and validate that the tethered region does not impede enzymatic activity. Once the enzyme is optimized for tethering to a surface, oriented immobilization has compelling advantages such as better activity and increased enzyme stability compared to adsorption or chemically-specific but non-oriented immobilization. Placement of an affinity tag at a specific location on an enzyme allows for an oriented tethering with the surface, therefore leaving catalytic binding domains accessible and permitting needed conformational changes as well as quaternary structure formation.

Our tethered enzyme technology enabled us to immobilize enzymes to inorganic scaffolds and use their catalytic functions for in vitro applications, but as we soon learned tethering of the enzyme was not the only factor which had an effect on enzymatic activity. The surface to which the enzyme is bound also impacts function; for example, the change from a planar surface to a NP led to a substantial increase in activity. From this observation we hypothesized that the size and curvature of the surface impacts the kinetics of tethered enzymes. This was proven true for maximal enzyme loading on gold NPs ranging in size from 5 to 50 nm in diameter, which displayed a decreased enzyme efficiency as the NP size increased. However, it is worth noting that enzyme multilayers formed as NP size increased. Looking at a monolayer of enzyme, we did not see a significant change in kinetics. This suggested that the success of our tethering strategy was not dependent on the curvature or size of NP. This is only one step toward understanding the full effects that the surface and environment have on tethered enzymes, thus more fundamental relationships need to be addressed such as the impact of surface composition,

geometry, roughness, porosity and charge as well as environmental factors including pH, temperature, viscosity and salt concentrations.

A diagnostic platform using a plate reader emerged from the use of our tethered enzyme technology with the potential to change the medical diagnostic paradigm. The platform was born from the advantage of tethering multiple types of enzymes to NPs for cascade reactions which displayed enhanced coupled enzymatic efficiency. We used these advantages to detect pathology-specific biomarkers. The coupled efficiency together with rapid enzymatic catalysis uniquely positioned the platform technology to detect markers for time-sensitive pathologies, such as stroke. We showed that we could detect NSE within 10 minutes using in vitro buffer solutions, rat stroke models, and finally patient blood samples. For our purposes, we have sufficient data to show that NSE can be detected through our enzymatic platform with comparable results to ELISA data; however, we have not ruled out whether other factors might confound our diagnostic results. These factors could be in the form of medications the patients are taking, the age of the patients, blood concentrations caused by dehydration, and many other possible blood contaminants which could have an effect on how the enzymes in our system function. To further develop this platform for clinical use in hospital laboratories, much attention needs to be focused on blood borne differences found in disparate patients during meticulous clinical trials. Even with this, our platform will need to be expanded to detect a panel of biomarkers to provide more robust diagnostic capability.

In this regard, we have investigated an additional biomarker, PGM. The ideal situation would be for our platform to detect a panel of pathology-specific biomarkers, with each biomarker narrowing in on what is the exact cause of the patient's ailment. A future device would include panels of biomarkers focused on specific diseases, such as a stroke panel or acute myocardial infarction panel. By showing PGM detection, which complicates the enzymatic reaction by including one more tethered enzyme in

the system, we can move to even more complicated reactions for the detection of more stroke-specific biomarkers such as S100 β and GFAP.

The current stroke diagnostic methodology is very time consuming and requires expert knowledge. Our PoCT platform will change this methodology by adding a step before traditional diagnostics during which the patient, caregiver or paramedic can measure blood biomarkers without the need for neurological expertise. The results could enable health care providers to skip time consuming steps and potentially begin immediate treatment. The PoCT platform is not just a proof of concept to be forgotten and possibly turned into something else down the line, but instead it is the first step in creating a functional PoCT diagnostic tool with advantages that open new avenues for diagnostic and prognostic care. Being able to utilize a single drop of blood to rapidly detect a number of biomarkers in a handheld device without any sophisticated instrumentation could have staggering implications for the medical community. Here we presented the very first generation, utilizing a microfluidic chip with our tethered enzyme technology for the detection of NSE with positive and negative controls through a single inlet in a plate reader. We have already opened collaborations to miniaturize the detection device to use photodiodes for simultaneous detection of multiple channels. As this is a first generation device there are a plethora of future directions.

Future work should focus on optimizing the reactions and lyophilization conditions to allow for a more sensitive device which will be stable over a longer period of time. The current reaction utilizes pluronic as a cryoprotectant, with the additional benefit that it enhanced reaction rates. However, unlike the months of stable storage we obtained with sorbitol when freezing in 96 well plates, the reagents lyophilized with pluronic kept maximal activity only for days. Combining trehalase and sorbitol at varying concentrations with the pluronic might help obtain better results. This work has started in the right direction with the ability to accurately detect one biomarker, but the true power of the PoCT

platform will be to detect multiple biomarkers simultaneously through a single drop of blood. Thus more biomarkers need to be linked to enzymatic cascades and detected for potential diagnostic value. Lastly, in our current experiments, we needed to separate the serum before introducing it into the device. In the future, the separation of blood and serum should occur on the chip. This is possible with current nanofabrication techniques for blood-plasma separation, but that was outside the scope of this dissertation.

In summary, we have developed a biomimetic strategy for tethering enzymes which imbues them with better activity than the same enzymes when attached via other immobilization strategies. We investigated and defined the fundamental changes that NP size and curvature have on tethered enzyme kinetics in order to optimize our tethering technique. We utilized our technology as the basis for a medical diagnostic platform, which we used to detect NSE within 10 minutes using rat stroke models and human patient samples. We achieved comparable results to commercial ELISA tests, which typically take 3-4 hours. We extended our diagnostic to detect PGM as well. We took a major step of developing the tethered enzyme approach into a PoCT platform by designing microchannel chips for the detection NSE with minimal sample size. Our PoCT platform for biomarker detection has the potential of changing the clinical diagnostic paradigm with fast results, obtained with an easy and portable card-reader system.

REFERENCES

1. Minteer, S.D. Springer Protocols: Enzyme Stabilization and immobilization, Methods and Protocols, Edn. 679. (Human Press, St. Louis; 2011).
2. Knotts, T.A., Rathore, N. & de Pablo, J.J. An Entropic Perspective of Protein Stability on Surfaces. *Biophysical Journal* **94**, 4473-4483 (2008).
3. Schoemaker, H.E. Dispelling the myths-- Biocatalysis in industrial synthesis. *Science* **299**, 1694-1697 (2003).
4. Zebda, A. et al. Mediatorless high-power glucose biofuel cells based on compressed carbon nanotube-enzyme electrodes. *Nature Communications* **2**, 370 (2011).
5. Demin, S. & Hall, E.A.H. Breaking the barrier to fast electron transfer. *Bioelectrochemistry* **76**, 19-27 (2009).
6. Arruda, D.L. et al. Microelectrical sensors as emerging platforms for protein biomarker detection in point-of-care diagnostics. *Expert Review of Molecular Diagnostics* **9**, 749-755 (2009).
7. Yoo, H.S., Kim, T.G. & Park, T.G. Surface-functionalized electrospun nanofibers for tissue engineering and drug delivery. *Advanced Drug Delivery Reviews* **61**, 1033-1042 (2009).
8. Fischer, T. & Hess, H. Materials chemistry challenges in the design of hybrid bionanodevices: supporting protein function within artificial environments. *Journal of Materials Chemistry* **17**, 943 (2007).
9. Talbert, J.N. & Goddard, J.M. Enzymes on Material Surfaces. *Colloids and Surfaces B: Biointerfaces* **93**, 8-19 (2012).
10. Hermanson, G.T. Bioconjugate Techniques, Edn. 3rd Edition. (Academic Press, 2013).
11. Vertegel, A.A., Siegel, R.W. & Dordick, J.S. Silica nanoparticle size influences the structure and enzymatic activity of adsorbed lysozyme. *Langmuir* **20**, 6800-6807 (2004).
12. Sivaraman, B., Fears, K.P. & Latour, R.A. Investigation of the Effects of Surface Chemistry and Solution Concentration on the Conformation of Adsorbed Proteins Using an Improved Circular Dichroism Method. *Langmuir* **25**, 3050-3056 (2009).
13. Nakamura, N., Mori, C. & Eddy, E.M. Molecular Complex of Three Testis-Specific Isozymes Associated with the Mouse Sperm Fibrous Sheath: Hexokinase 1, Phosphofructokinase M, and Glutathione S-Transferase mu class 5. *Biology of Reproduction* **82**, 504-515 (2009).
14. Miki, K. et al. Glyceraldehyde 3-phosphate dehydrogenase-S, a sperm-specific glycolytic enzyme, is required for sperm motility and male fertility. *Proceedings of the National Academy of Sciences* **101**, 16501-16506 (2004).
15. Travis, A.J. et al. Targeting of a germ cell-specific type 1 hexokinase lacking a porin-binding domain to the mitochondria as well as to the head and fibrous sheath of murine spermatozoa. *Mol Biol Cell* **9**, 263-276 (1998).
16. Krisfalusi, M. Multiple Glycolytic Enzymes Are Tightly Bound to the Fibrous Sheath of Mouse Spermatozoa. *Biology of Reproduction* **75**, 270-278 (2006).
17. Eddy, E.M., Toshimori, K. & O'Brien, D.A. Fibrous sheath of mammalian spermatozoa. *Microscopy Research and Technique* **61**, 103-115 (2003).
18. Mukai, C. et al. Biomimicry enhances sequential reactions of tethered glycolytic enzymes, TPI and GAPDHS. *PLoS One* **8**, e61434 (2013).
19. Mukai, C., Bergkvist, M., Nelson, J.L. & Travis, A.J. Sequential reactions of surface- tethered glycolytic enzymes. *Chem Biol* **16**, 1013-1020 (2009).
20. Yu, C.-C. et al. Site-specific immobilization of enzymes on magnetic nanoparticles and their use in organic synthesis. *Bioconjugate Chemistry* **23**, 714-724 (2012).

21. Wu, C.-S., Lee, C.-C., Wu, C.-T., Yang, Y.-S. & Ko, F.-H. Size-modulated catalytic activity of enzyme–nanoparticle conjugates: a combined kinetic and theoretical study. *Chemical Communications* **47**, 7446 (2011).
22. Papat, A. et al. Mesoporous silica nanoparticles for bioadsorption, enzyme immobilisation, and delivery carriers. *Nanoscale* **3**, 2801 (2011).
23. Keighron, J.D. & Keating, C.D. Enzyme:Nanoparticle Bioconjugates with Two Sequential Enzymes: Stoichiometry and Activity of Malate Dehydrogenase and Citrate Synthase on Au Nanoparticles. *Langmuir* **26**, 18992-19000 (2010).
24. Roger, V.L. et al. Heart Disease and Stroke Statistics--2011 Update: A Report From the American Heart Association. *Circulation* **123**, e18-e209 (2010).
25. Hand, P.J., Kwan, J., Lindley, R.I., Dennis, M.S. & Wardlaw, J.M. Distinguishing Between Stroke and Mimic at the Bedside: The Brain Attack Study. *Stroke* **37**, 769-775 (2006).
26. Disor., N.I.N. & al., e. Tissue Plasminogen Activator For Acute Ischemic Stroke. *The New England Journal of Medicine* **333**, 7 (1995).
27. Saenger, A.K. & Christenson, R.H. Stroke Biomarkers: Progress and Challenges for Diagnosis, Prognosis, Differentiation, and Treatment. *Clinical Chemistry* **56**, 21-33 (2009).
28. Whiteley, W., Chong, W.L., Sengupta, A. & Sandercock, P. Blood Markers for the Prognosis of Ischemic Stroke: A Systematic Review. *Stroke* **40**, e380-e389 (2009).
29. Brea, D. et al. Temporal profile and clinical significance of serum neuron-specific enolase and S100 in ischemic and hemorrhagic stroke. *Clinical Chemistry and Laboratory Medicine* **47** (2009).
30. Dauberschmidt, R. et al. Severe Head Trauma and the Changes of Concentration of Neuron-Specific Enolase in Plasma and in Cerebrospinal Fluid. **131**, 6 (1983).
31. Whiteley, W., Tseng, M.C. & Sandercock, P. Blood Biomarkers in the Diagnosis of Ischemic Stroke: A Systematic Review. *Stroke* **39**, 2902-2909 (2008).
32. Nishinari, M. et al. Phosphoglucosmutase Activity as a Novel Biomarker in Patients With Acute Myocardial Infarction. *Circulation Journal* **76**, 2197-2203 (2012).
33. Hayashi, T. & Matuo, Y. A new stroke marker as detected by serum phosphoglycerate mutase B-type isozyme. *Biochem Biophys Res Commun* **287**, 843-845 (2001).
34. Robin, X. et al. Bioinformatics for protein biomarker panel classification: what is needed to bring biomarker panels into in vitro diagnostics? *Expert Review of Proteomics* **6**, 675-689 (2009).
35. Song, Y. et al. Point-of-care technologies for molecular diagnostics using a drop of blood. *Trends Biotechnol* **32**, 132-139 (2014).
36. Paulie, S., Perlmann, H. & Perlmann, P. Enzyme-linked Immunosorbent Assay. *Encyclopedia of Life Sciences*, 4 (2005).
37. Hilvert, D. Critical Analysis of Antibody Catalysis. *Annual Review of Biochemistry* **69**, 42 (2000).
38. Viallard, J.L., Murthy, M.R. & Dastugue, B. An Ultramicro Bioluminescence Assay of Enolase-Application to Human Cerebrospinal Fluid. *Neurochem Res* **10**, 11 (1985).
39. Wevers, R.A., Jacobs, A.A.C. & Hommes, O.R. A Bioluminescent Assay for Enolase (EC 4.2.1.11) Activity in Human Serum and Cerebrospinal Fluid. *Clinica Chimica Acta* **135**, 9 (1983).
40. Gervais, L., de Rooij, N. & Delamarche, E. Microfluidic Chips for Point-of-Care Immunodiagnosics. *Advanced Materials* **23**, H151-H176 (2011).
41. Melin, J. & Quake, S.R. Microfluidic large-scale integration: the evolution of design rules for biological automation. *Annu Rev Biophys Biomol Struct* **36**, 213-231 (2007).
42. Grover, W.H., Ivester, R.H., Jensen, E.C. & Mathies, R.A. Development and multiplexed control of latching pneumatic valves using microfluidic logical structures. *Lab on a Chip* **6**, 623-631 (2006).
43. Hulme, S.E., Shevkopyas, S.S. & Whitesides, G.M. Incorporation of prefabricated screw, pneumatic, and solenoid valves into microfluidic devices. *Lab on a Chip* **9**, 79-86 (2009).

44. Oh, W.K., Arum, H., Shekhar, B. & Chong, H.A. A low-temperature bonding technique using spin-on fluorocarbon polymers to assemble microsystems. *JOURNAL OF MICROMECHANICS AND MICROENGINEERING* **12**, 6 (2002).
45. Maillefer, D. et al. A High-Performance Silicon Micropump For Disposable Drug Delivery Systems. *IEEE*, 5 (2001).
46. Fan, Z.H. & Harrison, D.J. Micromachining of Capillary Electrophoresis Injectors and separators on glass chips and evaluation of flow at capillary intersections. *Analytical Chemistry* **66**, 8 (1994).
47. Duffy, D.C., Gillis, H.L., Lin, J., Sheppard, N., Jr. F. & Kellogg, G.J. Microfabricated Centrifugal Microfluidic Systems, characterization and multiple enzymatic assays. *Analytical Chemistry* **71**, 10 (1999).
48. Lutz, S. et al. Microfluidic lab-on-a-foil for nucleic acid analysis based on isothermal recombinase polymerase amplification (RPA). *Lab on a Chip* **10**, 887-893 (2010).
49. Sista, R. et al. Development of a digital microfluidic platform for point of care testing. *Lab on a Chip* **8**, 2091-2104 (2008).
50. Zimmermann, M., Hunziker, P. & Delamarche, E. Valves for autonomous capillary systems. *Microfluidics and Nanofluidics* **5**, 395-402 (2008).
51. Buechler, K.F. diagnostic devices for the controlled movement of reagents without membranes. (1995). 5458852
52. Beebe, D.J. et al. Functional hydrogel structures for autonomous flow control inside microfluidic channels. *Nature* **404**, 3 (2000).
53. Zimmermann, M., Schmid, H., Hunziker, P. & Delamarche, E. Capillary pumps for autonomous capillary systems. *Lab on a Chip* **7**, 119 (2007).
54. Clearblue 2013).
55. Zimmermann, M., Schmid, H., Hunziker, P. & Delamarche, E. Capillary pumps for autonomous capillary systems. *Lab on a Chip* **7**, 119-125 (2007).
56. Hosokawa, K., Omata, M., Sato, K. & Maeda, M. Power-free sequential injection for microchip immunoassay toward point-of-care testing. *Lab on a Chip* **6**, 236-241 (2006).
57. Fan, R. et al. Integrated barcode chips for rapid, multiplexed analysis of proteins in microliter quantities of blood. *Nat Biotechnol* **26**, 1373-1378 (2008).
58. Weiss, G.A. & Penner, R.M. The Promise of Phage Display, customized affinity and specificity. *Analytical Chemistry*, 8 (2008).
59. Yeo, W.S., Min, D.H., Hsieh, R.W., Greene, G.L. & Mrksich, M. Label-free detection of protein-protein interactions on biochips. *Angew Chem Int Ed Engl* **44**, 5480-5483 (2005).
60. Cornell, B.A. et al. A biosensor that uses ion-channel switches. *Nature* **387**, 4 (1997).
61. Xu, H. et al. Aptamer-Functionalized Gold Nanoparticles as probes in a dry-reagent strip biosensor for protein analysis. *Analytical Chemistry* **81**, 7 (2009).
62. Gervais, L. & Delamarche, E. Toward one-step point-of-care immunodiagnosics using capillary-driven microfluidics and PDMS substrates. *Lab on a Chip* **9**, 3330-3337 (2009).
63. Lange, S.A. et al. Measuring biomolecular binding events with a compact disc player device. *Angew Chem Int Ed Engl* **45**, 270-273 (2005).
64. Bruls, D.M. et al. Rapid integrated biosensor for multiplexed immunoassays based on actuated magnetic nanoparticles. *Lab on a Chip* **9**, 3504-3510 (2009).
65. Gaster, R.S. et al. Matrix-insensitive protein assays push the limits of biosensors in medicine. *Nature Medicine* **15**, 1327-1332 (2009).
66. Ouellet, E. et al. Parallel microfluidic surface plasmon resonance imaging arrays. *Lab on a Chip* **10**, 581-588 (2010).
67. Mandal, S., Goddard, J.M. & Erickson, D. A multiplexed optofluidic biomolecular sensor for low mass detection. *Lab on a Chip* **9**, 2924-2932 (2009).

68. Kim, A. et al. Direct label-free electrical immunodetection in human serum using a flow-through-apparatus approach with integrated field-effect transistors. *Biosens Bioelectron* **25**, 1767-1773 (2010).
69. McKendry, R. et al. Multiple label-free biodetection and quantitative DNA-binding assays on a nanomechanical cantilever array. *Proc Natl Acad Sci U S A* **99**, 9783-9788 (2002).
70. Halliwell, C.M., Morgan, G., Ou, C.-P. & Cass, A.E.G. Introduction of a (poly)histidine tag in l-lactate dehydrogenase produces a mixture of active and inactive molecules. *Anal Biochem* **295**, 257-261 (2001).
71. Kim, J., Grate, J.W. & Wang, P. Nanostructures for enzyme stabilization. *Chemical Engineering Science* **61**, 1017-1026 (2006).
72. Bower, C.K., Sananikone, S., Bothwell, M.K. & McGuire, J. Activity losses among T4 lysozyme charge variants after adsorption to colloidal silica. *Biotechnology and Bioengineering* **64**, 373-376 (1998).
73. Czeslik, C. & Winter, R. Effect of temperature on the conformation of lysozyme adsorbed to silica particles. *Physical Chemistry Chemical Physics* **3**, 235-239 (2001).
74. Jia, H., Zhu, G. & Wang, P. Catalytic behaviors of enzymes attached to nanoparticles: the effect of particle mobility. *Biotechnology and Bioengineering* **84**, 406-414 (2003).
75. Park, H.J., McConnell, J.T., Boddohi, S., Kipper, M.J. & Johnson, P.A. Synthesis and characterization of enzyme-magnetic nanoparticle complexes: effect of size on activity and recovery. *Colloids and Surfaces B: Biointerfaces* **83**, 198-203 (2011).
76. Hainfeld, J.F., Liu, W., Halsey, C.M.R., Freimuth, P. & Powell, R.D. Ni-NTA Au clusters target his-tagged proteins. *Journal of Structural Biology* **127**, 185-198 (1999).
77. Rezwani, K., Studart, A.R., Voros, J. & Gauckler, L.J. Change of zeta potential of biocompatible colloidal oxide particles upon adsorption of bovine serum albumin and lysozyme. *Journal of Physical Chemistry B* **109**, 14469-14474 (2005).
78. Greenwood, R. & Kendall, K. Selection of suitable dispersants for aqueous suspensions of zirconia and titania powders using acoustophoresis. *Journal of the European Ceramic Society* **19**, 479-488 (1999).
79. Hanaor, D., Michelazzi, M., Leonelli, C. & Sorrell, C.C. The effects of carboxylic acids on the aqueous dispersion and electrophoretic deposition of ZrO₂. *Journal of the European Ceramic Society* **32**, 235-244 (2012).
80. Phillip, Y. & Schreiber, G. Formation of protein complexes in crowded environments—from in vitro to in vivo. *FEBS Lett* **587**, 1046-1052 (2013).
81. Kuznetsova, I.M., Turoverov, K.K. & Uversky, V.N. What macromolecular crowding can do to a protein. *Int J Mol Sci* **15**, 23090-23140 (2014).
82. WHO (2002).
83. Maiser, S.J. et al. Intravenous recombinant tissue plasminogen activator administered after 3 h following onset of ischaemic stroke: a metaanalysis. *Int J Stroke* **6**, 25-32 (2011).
84. Song, Y. et al. Point-of-care technologies for molecular diagnostics using a drop of blood. *Trends Biotechnol* **32**, 132-139 (2014).
85. Dash, P.K., Zhao, J., Hergenroeder, G. & Moore, A.N. Biomarkers for the diagnosis, prognosis, and evaluation of treatment efficacy for traumatic brain injury. *Neurotherapeutics* **7**, 100-114 (2010).
86. Ahmad, O., Wardlaw, J. & Whiteley, W.N. Correlation of levels of neuronal and glial markers with radiological measures of infarct volume in ischaemic stroke: a systematic review. *Cerebrovasc Dis* **33**, 47-54 (2012).
87. Wunderlich, M.T., Lins, H., Skalej, M., Wallesch, C.W. & Goertler, M. Neuron-specific enolase and tau protein as neurobiochemical markers of neuronal damage are related to early clinical

- course and long-term outcome in acute ischemic stroke. *Clin Neurol Neurosurg* **108**, 558-563 (2006).
88. Culler, L., Whitcomb, J. & Webster, S. Serum neuron-specific enolase predicting neurological outcomes post-cardiac arrest: a review of the literature. *Dimens Crit Care Nurs* **33**, 309-315 (2014).
 89. Cheng, F., Yuan, Q., Yang, J., Wang, W. & Liu, H. The prognostic value of serum neuron-specific enolase in traumatic brain injury: systematic review and meta-analysis. *PLoS One* **9**, e106680 (2014).
 90. Chaves, M.L. et al. Serum levels of S100B and NSE proteins in Alzheimer's disease patients. *J Neuroinflammation* **7**, 6 (2010).
 91. Wevers, R.A., Jacobs, A.A. & Hommes, O.R. A bioluminescent assay for enolase (EC 4.2.1.11) activity in human serum and cerebrospinal fluid. *Clin Chim Acta* **135**, 159-168 (1983).
 92. Viallard, J.L., Murthy, M.R. & Dastugue, B. An ultramicro bioluminescence assay of enolase: application to human cerebrospinal fluid. *Neurochem Res* **10**, 1555-1566 (1985).
 93. Wevers, R.A., Theunisse, A.W. & Rijksen, G. An immunobioluminescence assay for gamma-gamma enolase activity in human serum and cerebrospinal fluid. *Clin Chim Acta* **178**, 141-150 (1988).
 94. Halliwell, C.M., Morgan, G., Ou, C.P. & Cass, A.E. Introduction of a (poly)histidine tag in L-lactate dehydrogenase produces a mixture of active and inactive molecules. *Anal Biochem* **295**, 257-261 (2001).
 95. Travis, A.J. et al. Functional relationships between capacitation-dependent cell signaling and compartmentalized metabolic pathways in murine spermatozoa. *J Biol Chem* **276**, 7630-7636 (2001).
 96. Naik, R.R., Brott, L.L., Clarson, S.J. & Stone, M.O. Silica-precipitating peptides isolated from a combinatorial phage display peptide library. *J Nanosci Nanotechnol* **2**, 95-100 (2002).
 97. Schaffer, C.B. et al. Two-photon imaging of cortical surface microvessels reveals a robust redistribution in blood flow after vascular occlusion. *PLoS Biol* **4**, e22 (2006).
 98. Oren, E.E. et al. Probing the molecular mechanisms of quartz-binding peptides. *Langmuir* **26**, 11003-11009 (2010).
 99. Nakamura, M., Mie, M., Funabashi, H. & Kobatake, E. Construction of streptavidin-luciferase fusion protein for ATP sensing with fixed form. *Biotechnol Lett* **26**, 1061-1066 (2004).
 100. Ford, S.R., Chenault, K.D., Hall, M.S., Pangburn, S.J. & Leach, F.R. Effect of periodate-oxidized ATP and other nucleotides on firefly luciferase. *Arch Biochem Biophys* **314**, 261-267 (1994).
 101. Ford, S.R. et al. Use of firefly luciferase for ATP measurement: other nucleotides enhance turnover. *J Biolumin Chemilumin* **11**, 149-167 (1996).
 102. Casmiro, M. et al. Cerebrospinal fluid and serum neuron-specific enolase concentrations in a normal population. *Eur J Neurol* **12**, 369-374 (2005).
 103. Marginean, I.C. et al. Plasmatic markers in hemorrhagic stroke. *J Med Life* **4**, 148-150 (2011).
 104. Chung, J.W., Ryu, W.S., Kim, B.J. & Yoon, B.W. Elevated calcium after acute ischemic stroke: association with a poor short-term outcome and long-term mortality. *J Stroke* **17**, 54-59 (2015).
 105. Stippler, M. et al. Serum and cerebrospinal fluid magnesium in severe traumatic brain injury outcome. *J Neurotrauma* **24**, 1347-1354 (2007).
 106. Hasan, N., McColgan, P., Bentley, P., Edwards, R.J. & Sharma, P. Towards the identification of blood biomarkers for acute stroke in humans: a comprehensive systematic review. *Br J Clin Pharmacol* **74**, 230-240 (2012).
 107. Hay, E. et al. Cerebrospinal Fluid Enolase in Stroke. *Journal of Neurology, Neurosurgery, and Psychiatry* **47**, 6 (1984).

108. Durany, N. et al. Activity of Phosphoglycerate Mutase and its Isozymes in Serum After Acute Myocardial Infarction. *Journal of Clinical Pathology: Molecular Pathology* **49**, 4 (1996).
109. Chin, C.D., Linder, V. & Sia, S.K. Commercialization of Microfluidic Point-of-Care Diagnostic Devices. *Lab on a Chip* **12**, 2118 (2012).
110. Vertegel, A., Siegel, R. & Dordick, J. Silica Nanoparticle Size Influences the Structure and Enzymatic Activity of Adsorbed Lysozyme. *Langmuir* **20**, 8 (2004).
111. Fears, K.P., Sivaraman, B., Powell, G.L., Wu, Y. & Latour, R.A. Probing the Conformation and Orientation of Adsorbed Enzymes Using Side-Chain Modification. *Langmuir* **25**, 9319-9327 (2009).
112. Friedel, M., Baumketner, A. & Shea, J.-E. Stability of a protein tethered to a surface. *The Journal of Chemical Physics* **126**, 095101 (2007).
113. Rusmini, F., Zhong, Z. & Feijen, J. Protein Immobilization Strategies for Protein Biochips. *Biomacromolecules* **8**, 1775-1789 (2007).
114. Xu, C. et al. Dopamine as A Robust Anchor to Immobilize Functional Molecules on the Iron Oxide Shell of Magnetic Nanoparticles. *Journal of the American Chemical Society* **126**, 9938-9939 (2004).
115. Toda, A., Yamada, K. & Nishimura, S.-I. An Engineered Biocatalyst for the Synthesis of Glycoconjugates: Utilization of β 1,3-N-Acetyl-D-glucosaminyltransferase from *Streptococcus agalactiae* Type Ia Expressed in *Escherichia coli* as a Fusion with Maltose-Binding Protein. *Advanced Synthesis & Catalysis* **344**, 61-69 (2002).
116. Holland-Nell, K. & Beck-Sickinger, A.G. Specifically Immobilised Aldo/Keto Reductase AKR1A1 Shows a Dramatic Increase in Activity Relative to the Randomly Immobilised Enzyme. *ChemBioChem* **8**, 1071-1076 (2007).
117. Turková, J. Oriented Immobilization of Biologically Active Proteins as a Tool for Revealing Protein Interactions and Function. *Journal of Chromatography B: Biomedical Sciences and Applications* **722**, 11-31 (1999).
118. Zhang, E., Brewer, J.M., Minor, W., Carreira, L.A. & Lebioda, L. Mechanism of Enolase: The Crystal Structure of Asymmetric Dimer Enolase-2-Phospho-D-glycerate/Enolase-Phosphoenolpyruvate at 2.0 Å Resolution. *Biochemistry* **36**, 9 (1997).
119. Nakamura, N. et al. Disruption of a Spermatogenic Cell-Specific Mouse Enolase 4 (Eno4) Gene Causes Sperm Structural Defects and Male Infertility. *Biology of Reproduction* (2013).
120. Force, A., Viillard, J.-L., Saez, F., Grizard, G. & Boucher, D. Electrophoretic Characterization of the Human Sperm-Specific Enolase at Different Stages of Maturation. *Journal of Andrology* **25**, 6 (2004).
121. Edwards, Y. & Grootegoed, J.A. A Sperm-Specific Enolase. *Journal of Reproduction and Fertility Ltd* **68**, 8 (1983).
122. Guo, S., Li, D., Zhang, L., Li, J. & Wang, E. Monodisperse Mesoporous Superparamagnetic Single-Crystal Magnetite Nanoparticles for Drug Delivery. *Biomaterials* **30**, 1881-1889 (2009).
123. Gao, L. et al. Intrinsic peroxidase-like activity of ferromagnetic nanoparticles. *Nature Nanotechnology* **2**, 577-583 (2007).
124. Go, A.S. et al. Heart Disease and Stroke Statistics--2014 Update: A Report From the American Heart Association. *Circulation* **129**, e28-e292 (2013).
125. Schaarschmidt, H., Prange, H.W. & Reiber, H. Neuron-specific enolase concentrations in blood as a prognostic parameter in cerebrovascular diseases. *Stroke* **25**, 558-565 (1994).
126. Yetisen, A.K., Akram, M.S. & Lowe, C.R. Paper-based microfluidic point-of-care diagnostic devices. *Lab on a Chip* **13**, 2210 (2013).
127. Ka-wang Wang, K., Hayes, R., Mueller, U. & Zhang, Z. Biomarker detection process and assay of neurological condition. U.S. Patent US 2011/0143375 A12011.

128. Selinfreund, R., Vig, R. & Gill, R. Devices and systems for biomarker detection. U.S. Patent US 2011/0195872 A12011
129. Dambinova, S. Rapid multiple panel of biomarkers in laboratory blood tests for TIA/stroke. U.S. Patent US 2006/0024749 A12006
130. Dambinova, S. Assay methods for immediate diagnosis of cause of stroke. U.S. Patent US 2006/0172341 A12006
131. Chin, C.D. et al. Microfluidics-based diagnostics of infectious diseases in the developing world. *Nature Medicine* **17**, 1015-1019 (2011).
132. Ford, B. & Ford, G. biomarkers for stroke. U.S. Patent 201200408582012
133. Montaner Vilallonga, J. differential diagnostic biomarkers of stroke mimicking conditions and methods of use thereof. U.S. Patent 201102946902011
134. Sharp, F., Stamova, B. & Jickling, G. biomarkers for diagnosis of stroke and its causes. U.S. Patent 201200650872012
135. Sibon, I., Rouanet, F., Meissner, W. & Orgogozo, J.M. Use of the Triage Stroke Panel in a neurologic emergency service. *The American Journal of Emergency Medicine* **27**, 558-562 (2009).
136. MicroChem SU-8 2000 Permanent Epoxy Negative Photoresist Processing Guidelines for: SU-8 2100 and SU-8 2150. *Data Sheet* (2015).